Search for steady and flaring astrophysical neutrino point sources with the IceCube detector

D I S S E R T A T I O N

zur Erlangung des akademischen Grades

doctor rerum naturalium
(Dr. rer. nat.)
im Fach Physik

eingereicht an der
Mathematisch-Naturwissenschaftlichen Fakultät I
Humboldt-Universität zu Berlin

von
M.Sc. José Luis Bazo Alba

Präsident der Humboldt-Universität zu Berlin:
Prof. Dr. Dr. h.c. Christoph Markschies

Dekan der Mathematisch-Naturwissenschaftlichen Fakultät I:
Prof. Dr. Andreas Herrmann

Gutachter:
1. Dr. Elisa Bernardini
2. Prof. Dr. Thomas K. Gaisser
3. Prof. Dr. Hermann Kolanoski

eingereicht am: 10.06.2010
Tag der mündlichen Prüfung: 30.08.2010

Abstract

High energy neutrino astronomy relies on the predictions of neutrino fluxes coming from astrophysical objects, for example active galactic nuclei. In these models, neutrinos and gamma-rays are produced in hadronic processes, which require the acceleration of protons to very high energies.

Since neutrinos hardly interact and travel towards Earth undeflected by magnetic fields, they can point back to their sources. IceCube, located at the South Pole, is a large volume detector for high energy neutrinos. In this work, data from two partial configurations of IceCube (22 and 40 strings) are analyzed looking for neutrino point-like sources. The data cover 651 days, from 2007 to 2009, and consist mostly of atmospheric muon neutrinos in the Northern sky and high energy atmospheric muons in the Southern sky.

A time integrated search for neutrino point sources in the Northern sky was developed and applied to an event sample obtained for the best sensitivity, with IceCube 22-string. The search was performed on a pre-selected list of candidate sources and the whole hemisphere was scanned. No evidence of a neutrino signal was found.

In order to enhance the flare detection probability, an untriggered time dependent search that looks for neutrino events clustering in time from specific sources in the entire sky was developed. This search was motivated by neutrino-photon correlations and the observations of flaring objects in gamma-rays, but focuses only on the neutrino data, covering a wide range of possible flare durations.

The search method was expanded from a binned approach to a newly developed unbinned likelihood method, improving the results by 5-25%. Moreover, for the first time the Southern sky was analyzed with a time dependent method. A source selection criteria was developed defining two lists of variable astrophysical sources, for IceCube 22 and 40-string. The results were compatible with background fluctuations for all sources tested. Therefore, upper limits on the neutrino fluence from these sources are presented.

Keywords: IceCube, point sources, neutrinos, flares, likelihood.

Für astrophysikalische Quellen, z. B. aktive galaktische Kerne, werden hochenergetische Neutrinoflüsse vorhergesagt. Neutrinos und Gammastrahlen werden in hadronischen Prozessen erzeugt, für die Protonen auf hohe Energien beschleunigt werden müssen.

Da Neutrinos nur schwach wechselwirken und nicht von Magnetfeldern abgelenkt werden können, bleiben Flussstärken und die ursprüngliche Richtung erhalten. IceCube, ein Kubikkilometer-Detektor der sich am Südpol befindet, kann solche Neutrinos nachweisen.

In dieser Arbeit wurden Daten zweier Teilkonfigurationen IceCubes (22 und 40 Trossen) im Rahmen der Suche nach Neutrino-Punktquellen ausgewertet. Die Daten, die zwischen 2007 und 2009 gesammelt wurden, bestehen hauptsächlich aus atmosphärischen Myon-Neutrinos, die im Nordhimmel erzeugt wurden und hochenergetischen atmosphärischen Myonen aus dem Südhimmel.

Eine zeitunabhängige Analyse, die nach astrophysikalischen Neutrino-Punktquellen im Nordhimmel sucht, wurde mit einem sensitivitäts-optimierten Datensatz von IceCube-22 durchgeführt. Die ganze Hemisphäre und eine Liste ausgewählter Quellen wurden analysiert, wobei kein Hinweis auf extraterrestrische Neutrino-Signale gefunden wurde.

Um das Entdeckungspotenzial für eine variable Quelle zu erhöhen, wurde eine nicht-getriggerte zeitabhängige Analyse entwickelt. Diese Suche ist durch Neutrino-Photon-Korrelationen und Gammastrahlung-Ausbrüche kosmischer Objekte motiviert, jedoch wurden nur Neutrino-Daten verwendet. Ein grosser Bereich möglicher Strahlungsausbruchsdauer wurde abgedeckt.

Die gebinnte Methode wurde zu einer ungebinnten Likelihood-Methode erweitert, so dass die Ergebnisse um 5-25% verbessert werden konnten. Auswahlkriterien für eine Liste zeitlich veränderlicher astrophysikalischer Quellen vom ganzen Himmel wurden für IceCube-22 und IceCube-40 entwickelt. Zum ersten Mal wurde eine zeitabhängige Suchmethode im Südhimmel benutzt. Es konnten keine Ereignisüberschüsse über dem Untergrund festgestellt werden. Demzufolge wurden obere Grenzen für Neutrinoflüsse aus diesen Quellen berechnet.

Schlagwörter: IceCube, Punktquellen, Neutrinos, Strahlungsausbrüche, Likelihood.

Resumen

La astronomía de neutrinos de altas energías se sustenta en las predicciones de flujos de neutrinos provenientes de objetos astrofísicos tales como núcleos activos de galaxias. En estos modelos, los neutrinos y los rayos gamma se producen en procesos hadrónicos que requieren la aceleración de protones hasta muy altas energías.

Dado que los neutrinos no son desviados por campos magnéticos, mantienen su dirección original apuntando a sus fuentes. Además debido a que interaccionan débilmente, su flujo inicial se preserva. IceCube, localizado en el Polo Sur, es un detector de gran volumen que puede observar neutrinos de alta energía. Este trabajo analiza los datos de dos configuraciones parciales de Ice Cube (22 y 40 cadenas), con el objetivo de buscar fuentes puntuales de neutrinos. Los datos abarcan 651 días de actividad del detector entre 2007 y 2009, y consisten mayormente en neutrinos muónicos atmosféricos en el hemisferio Norte y muones atmosféricos de alta energía en el hemisferio Sur.

Se llevó a cabo un análisis en búsqueda de fuentes puntuales de neutrinos en el hemisferio Norte, usando una muestra de eventos de IceCube con 22 cadenas. La búsqueda se aplicó a una lista preseleccionada de objetos astrofísicos, examinando todo el hemisferio, no hallándose ninguna evidencia significativa de señal alguna de neutrinos extraterrestres.

Para incrementar la probabilidad de descubrir una fuente variable de neutrinos, se desarrolló un análisis temporal. Esta búsqueda fue motivada por la correlación entre neutrinos y fotones y las observaciones de llamaradas de rayos gamma. Sin embargo, en el análisis sólo se usaron los datos de neutrinos, abarcando un amplio rango de posibles duraciones de las llamaradas.

El método de búsqueda se amplió implementando un nuevo método de máxima verosimilitud, mejorándose los resultados anteriores en un 5 a 25 %. Por primera vez se analizó el hemisferio Sur con un método dependiente del tiempo. Se desarrollaron criterios para seleccionar una lista de fuentes astrofísicas variables en todo el cielo para IceCube con 22 y 40 cadenas. No se detectó ningún exceso de eventos que permitiera identificar una fuente puntual, pues los resultados fueron compatibles con las fluctuaciones de fondo para todas las fuentes probadas. En consecuencia, se calcularon los límites superiores del flujo de neutrinos para cada fuente.

Palabras clave: IceCube, fuentes puntuales, neutrinos, llamaradas, máxima verosimilitud.

Contents

1. Introduction **1**

2. High Energy Neutrino Astronomy **3**
2.1. Cosmic-ray connection . . . 3
2.2. Possible sources of high energy neutrinos . . . 5
2.2.1. Galactic source candidates . . . 5
2.2.2. Extragalactic source candidates . . . 6
2.3. Acceleration Mechanism . . . 8
2.4. Neutrino Production . . . 9
2.5. Neutrino oscillations . . . 10
2.6. Expected neutrino fluxes . . . 11
2.7. Multi-messenger astronomy . . . 12

3. High Energy Neutrino Detection **13**
3.1. Neutrino telescope principle . . . 13
3.2. Neutrino-induced events . . . 14
3.2.1. Survival probability . . . 14
3.2.2. Interaction probability . . . 15
3.3. Cherenkov Effect . . . 17
3.4. Background . . . 17
3.4.1. Atmospheric muons . . . 17
3.4.2. Atmospheric neutrinos . . . 18

4. The ICECUBE Observatory **19**
4.1. Sub-detectors . . . 22
4.1.1. ICECUBE . . . 22
4.1.2. IceTop . . . 23
4.1.3. DeepCore . . . 24
4.2. Digital Optical Module and Data Acquisition . . . 24
4.3. Detector Calibration . . . 26
4.3.1. Time calibration . . . 26
4.3.2. Gain calibration . . . 26
4.4. Optical properties of ice . . . 26
4.4.1. Scattering . . . 27
4.4.2. Absorption . . . 28
4.5. Neutrino event signatures . . . 28
4.6. Triggers, filters and data processing . . . 29

5. Simulation & Reconstruction **31**
5.1. Simulation . . . 31
5.1.1. Event generators . . . 31

5.1.2. Particle propagation . . . 32
5.1.3. Photon propagation . . . 32
5.1.4. Detector response . . . 32
5.2. Reconstruction . . . 33
5.2.1. Extraction of photoelectrons from digitized waveforms . . . 33
5.2.2. First-guess track reconstruction . . . 34
5.2.3. Maximum Likelihood track reconstruction . . . 34
5.2.4. Angular uncertainty estimation . . . 36
5.2.5. Energy estimation . . . 36
5.2.6. Double muon reconstruction . . . 37
5.2.7. Online reconstruction & selection . . . 37

6. Analysis methods **39**
6.1. Point source search concept . . . 40
6.2. Time integrated search . . . 41
6.2.1. Binned method . . . 41
6.2.2. Unbinned maximum likelihood method . . . 43
6.3. Time dependent Search . . . 46
6.3.1. Binned method . . . 48
6.3.2. Unbinned maximum likelihood method . . . 49
6.4. Comparing binned versus unbinned methods . . . 56
6.5. Sensitivity and Discovery Potential . . . 58
6.5.1. Sensitivity and Upper Limits . . . 58
6.5.2. Discovery Potential . . . 59
6.6. Note on Blindness . . . 59
6.7. Note on Trial factors . . . 60

7. Data & Event selection **63**
7.1. Detector stability . . . 63
7.1.1. Run selection . . . 63
7.1.2. Lifetime . . . 64
7.2. Data processing . . . 65
7.3. Cut variables for event selection . . . 66
7.3.1. Parameters independent of the reconstructed direction . . . 66
7.3.2. Parameters dependent on the reconstructed direction . . . 67
7.3.3. Parameters dependent on the time residual interval . . . 69
7.3.4. Cut variables not used . . . 70
7.4. Cut optimization and final cuts for the time integrated search . . . 70
7.5. Event selection for the time dependent searches . . . 74
7.5.1. ICECUBE 22-string unbinned untriggered flare search event sample 74
7.5.2. ICECUBE 40-string unbinned untriggered flare search event sample 75
7.6. Final event sample description . . . 76
7.6.1. Time integrated search event sample . . . 76
7.6.2. Time dependent search event samples . . . 84

8. Source candidate selection **89**
8.1. Time integrated search source list . . . 89

8.2. Time dependent search source lists 91
8.2.1. ICECUBE 22-string candidate list 92
8.2.2. ICECUBE 40-string candidate list 93

9. Results **97**
9.1. Search for point sources in the Northern sky with ICECUBE 22-string . . 97
9.1.1. Candidate source list 97
9.1.2. Sky-map 100
9.2. Search for variable point sources in the whole sky 102
9.2.1. ICECUBE 22-string results 102
9.2.2. ICECUBE 40-string results 104
9.3. Uncertainties 107
9.3.1. Statistical errors 107
9.3.2. Systematic errors 107
9.3.3. Errors summary 113
9.3.4. Limits including uncertainties 113

10. Summary and Outlook **115**

A. Parametrization of the angular error from reconstruction **119**

B. Event selection cuts expanded **121**
B.1. ICECUBE 22-string Northern sky binned event sample cuts 121
B.2. ICECUBE 40-string all-sky unbinned event sample cuts 122

Bibliography **124**

List of Figures **135**

List of Tables **137**

Abbreviations **139**

1. Introduction

Wovon man nicht sprechen kann, darüber muss man schweigen.
Ludwig Wittgenstein 1889-1921
Tractatus logico-philosophicus

Neutrinos were first introduced by Pauli in 1930 to account for missing energy in beta decays. The detection of these chargeless, almost massless, weakly interacting particles took first place in 1956 by the Cowan-Reines experiment. At the beginning of the 1960's the idea of looking for astrophysical neutrinos was first postulated [Rei60]. Since these particles interact only weakly with matter, they would propagate virtually undeflected and with unchanged energy from their sources. In contrast, protons can be deflected by magnetic fields and more frequently interact. In addition, photons, even though they preserve their direction, can easily be absorbed in the cosmic microwave background radiation or cannot escape very dense media. Therefore neutrinos can be a powerful tool to explore the universe at large distances with good pointing accuracy.

A detector for high energy neutrinos (neutrino telescope) consists of a large three dimensional array of photomultiplier tubes in a Cherenkov medium like clear water or ice, with nanosecond timing precision in order to reconstruct the tracks. The first attempt to build a detector for high-energy neutrino astronomy was funded as a feasibility study in 1979. The project, to be constructed near Hawaii, was called DUMAND (Deep Underwater Muon And Neutrino Detector) [Rob92]. It carried out first feasibility studies but was cancelled in 1995. The Baikal experiment [B$^+$97] (its first stage installed in 1993 in Lake Baikal, Russia) was the first high energy neutrino telescope to detect atmospheric neutrinos. It proved the concept of three-dimensional Cherenkov light mapping deep underwater, also verifying that the muon background can be suppressed. At present, the ICECUBE detector, which began its deployment in 2005 at the geographical South Pole, is the biggest working neutrino telescope. The goal of a cubic kilometer neutrino detector, needed because of the small neutrino cross-section, is almost a reality.

Theories regarding the production of neutrinos in extraterrestrial sources have predicted different fluxes, many of which are expected to be observed by ICECUBE. Our knowledge about the sources is so far restricted to photon astronomy. The observations expand nowadays over a broad range of wavelengths, from optical and radio to x-rays and gamma rays. Some of the most luminous sources, like blazars, are observed in flaring states over time windows of several minutes to days. Other sources emit a steady, yet powerful flux of photons. Most of these astrophysical objects are possible candidates of correlated neutrinos.

The field of neutrino astronomy has just begun. So far the various analyses performed looking for an excess of high-energy extraterrestrial neutrinos have given null results. Neutrino flux upper limits have been lowered several times as newer and bigger detectors have been built. With the end of the construction period of ICECUBE in 2011, the astrophysics neutrino community faces an exciting time, where discoveries

might be possible.

The present thesis analyzes neutrino data from partial configurations of the ICECUBE detector to look for point sources of neutrinos from astrophysical objects that are in a steady or flaring state. Two types of analyses are developed: a time-integrated and a time-dependent. The thesis is divided into two main parts. The first part (chapters 2-5) gives a wide overview of neutrino-related astroparticle physics topics on theory and experiments. It is divided as follows: in Chapter 2 the candidate sources of astrophysical neutrinos are introduced, as well as their neutrino production mechanism and expected fluxes. In Chapter 3 the detection process of these neutrinos on Earth is presented, including the sources of background. In Chapter 4 the ICECUBE detector is characterized together with the event signatures and triggers. In Chapter 5 the detector event simulations and the track reconstructions and associated parameters are described.

The second part (chapters 6-10) is devoted to the analyses developed within the context of this work and their results. It is divided as follows: in Chapter 6 the two main analysis methods (time integrated and time dependent) and their corresponding binned and unbinned implementations are presented for a point source search. In Chapter 7 the event selection and final samples of the different datasets used are described. In Chapter 8 the selection of astrophysical steady and flaring source candidates is given. In Chapter 9 the results of applying both methods to the chosen datasets for the whole sky and source lists are shown and discussed. Given that the results are compatible with background fluctuations, neutrino flux and fluence upper limits are calculated. The results are followed by a review of the statistical and systematic uncertainties. Finally in Chapter 10 the main conclusions and prospects for the future search of astrophysical neutrinos are given.

2. High Energy Neutrino Astronomy

Jeder preist mir eine andere Theorie an,
doch die Realität, die man mir bietet, ist dieselbe ...
Friedrich Dürrenmatt 1921-1990
Die Physiker

Photon astronomy has a long and well established tradition, that has given us a vast knowledge about our universe. On the contrary, high energy neutrino astronomy has not yet been established. However, this new field has much potential to be exploited. Neutrinos are unique messengers to explore the universe because they have no charge and can only interact via the weak force. Since cosmic rays are a main motivation for neutrino astronomy, they are discussed first. Different extraterrestrial sources that are expected to produce neutrinos are briefly presented here. Then the production mechanism of neutrinos is introduced in its current, not yet established, phenomenology.

2.1. Cosmic-ray connection

Energetic particles, mainly protons ($\sim$79%) [A$^+$08] and nuclei, make up cosmic rays. The cosmic ray energy spectrum extends several orders of magnitude, from a few 10^8 eV, reaching up to energies of $\sim 10^{20}$ eV [A$^+$10b]. Neutrino production scenarios require high-energy protons. The fact that protons can be accelerated up to these energies is a powerful argument to support the idea of neutrinos being produced in the same sources. Unfortunately, these sources have not yet been singled out.

The flux of cosmic rays drops with energy, in the GeV-EeV range, about 30 orders of magnitude [HÖ6a], following different power laws. The presence of power laws is an indication of the non-thermal origin of the particles. The largest fluxes correspond to the lowest energies with a few particles per square centimeter per second. For the highest energies ($E > 10^{20}$eV) the flux is reduced to less than one particle per square kilometer in 100 years. The latter particles are believed to originate outside our galaxy, because the magnetic field inside the Milky Way is not strong enough to confine them.

Different features, changes of slope, of cosmic rays can be seen in Fig. 2.1a and Fig. 2.1b. In Fig. 2.1a the all-particle cosmic-ray spectrum is shown, while in Fig. 2.1b the indexes of the corresponding power laws are shown for different energy ranges. Up to energies about $\sim 3 \times 10^{15}$eV, where the *knee* [HÖ3] is located, it is believed that cosmic rays have a galactic origin. These energies can be reached in supernovae, where particles are accelerated by means of shock waves. The *knee* could point to the maximum energy for proton acceleration in supernova remnants. The second knee, at $\sim 4 \times 10^{17}$ eV, might be caused by contributions from heavy elements [HÖ6a] or it could represent the end of the galactic cosmic ray spectrum.

At about 3×10^{18}eV another break in the power law, called the *ankle*, appears. There are arguments in favor of explaining this feature as the transition from galactic to extragalactic sources. However, there have been speculations that this break could result

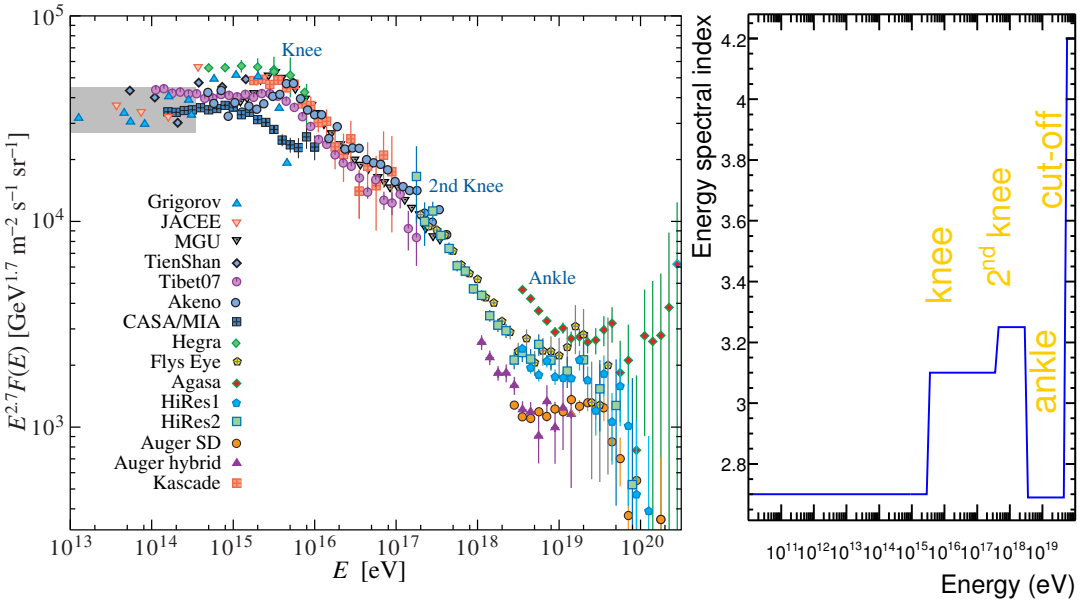

(a) Cosmic-ray spectrum

(b) Spectral index

Figure 2.1.: Left: Cosmic-ray all-particle spectrum from air shower measurements, taken from [A$^+$08]. Right: Cosmic rays energy spectral index as a function of energy. Values taken from [AM09].

from the propagation of protons from extragalactic sources [Ber06], thus the galactic/extragalactic transition could be at much lower energies. In this scenario protons would interact with the CMB resulting in pair production (e^+, e^-). This feature between 10^{18} and 10^{19} eV is also called the *dip*.

The last feature of the cosmic ray flux is seen at energies above 4×10^{19}eV [A$^+$10b] showing a suppression deviating from a power law. It can be attributed to the predicted Greisen-Zatsepin-Kuz'min (GZK) [Gre66] effect[1] or could be correlated with a maximum energy achievable by the production sources. The GZK cut-off also predicts a flux of high energy neutrinos due to photo-pion production caused by the interaction of high energy protons with the CMB.

The largest array used at present to detect ultra-high-energy cosmic rays (UHECR) is the Pierre Auger Southern Observatory [A$^+$10b] in Malargüe, Argentina. It detects simultaneously the shower particles generated by the interaction of cosmic rays in the Earth's atmosphere and the associated fluorescence light produced in the atmosphere. Data from this detector has been used to perform correlation studies between the directions of the highest energy cosmic rays and neutrinos [Lau10].

[1]The GZK cut-off gives the average maximum energy and distance of high energy protons before they are absorbed in the interaction with the cosmic microwave background (CMB) radiation. This interaction determines an average maximum radius of 100 Mpc for high-energy protons (> 50 EeV) that can still reach Earth without interacting in their propagation through the intergalactic medium.

2.2. Possible sources of high energy neutrinos

At present no identifiable source of high energy (E>10 GeV) neutrinos has been observed. However, at lower energies (MeV), two neutrino sources outside Earth have been detected: the Sun and SN1987a [AM09]. A handful of neutrinos coming from the supernova SN1987a was observed with three different detectors: Kamiokande II (11 neutrinos, [H^+87]), IMB (8 neutrinos, [B^+87]) and Baksan. The measurement of a deficit in the solar neutrino flux by several experiments (starting with the Homestake experiment) supported the idea of neutrino oscillations and, thus, neutrino mass, which was confirmed by SNO (Sudbury Neutrino Observatory).

The candidate sources for producing high-energy neutrinos are divided into galactic (lower energies) and extragalactic (up to higher energies). These objects are selected because they meet the minimum necessary requirements for accelerating protons to very high energies. This means they should have a strong magnetic field and a relative large size.

2.2.1. Galactic source candidates

Inside our Galaxy there are different astrophysical objects that could be responsible for the production of neutrinos, if hadronic processes take place in them. A short selection and description of these objects is given below.

Supernova remnants

Stars exploding in a supernova lead to the so-called supernova remnants (SNR). This structure is defined by a expanding shock wave of the ejected material that interacts with the interstellar medium. In this process, cosmic rays are believed to be accelerated, producing also neutrinos with energies greater than 1 TeV. Some of the brightest objects detected by EGRET are SNR [Der06]. They show a hard energy spectrum ($\sim E^{-2}$). Observations in the TeV energy range (e.g. from HESS) exhibit a cutoff around $\sim$ 10 TeV.

X-ray binaries

This class corresponds to a system of two astrophysical objects, where one, usually a stellar object (e.g. brown dwarf, main sequence star [Gri03]), is loosing matter to its compact companion (e.g. white dwarf, neutron star or black hole). This process releases gravitational potential energy which is then converted mainly into X-rays. According to the mass of the star, which also determines its visibility in the optical range, they can be subdivided into low-mass X-ray binaries (LMXB, fainter in optical observations) and high-mass X-ray binaries (HMXB, strong in both optical and X-rays). Time dependence due to orbital modulations is also observed. One mechanism to produce neutrinos in accreting neutron stars would be when protons, accelerated in the magnetosphere of the system, collide with the accretion disk [A^+03].

Microquasars

Microquasars are smaller versions of quasars, actually a sub-class of X-ray binaries, where the compact object (e.g. neutron star or black hole) has only a few solar masses.

The compact object presents an accretion disk and relativistic jets. The jets, outflows of plasma perpendicular to the accretion disk, are observable at radio wavelengths, showing time variability. Since they are not extremely massive, their variations are faster compared to a normal quasar and can be observed in the order of days. Most microquasars also show an extremely rapid variation in X-rays. Neutrino with energies between 1-100 TeV could be produced in the outbursts of these objects [LW01], if protons are accelerated in their jets to $\sim 10^{16}$ eV and interact with synchrotron photons emitted by accelerated electrons. In addition, proton-proton collisions could also lead to neutrinos.

Pulsar wind nebulae

The main example of a pulsar wind nebulae is the Crab Nebula, which contains a rapidly rotating highly magnetized young neutron star (i.e. pulsar). This pulsar creates a magnetized particle wind which emits synchrotron radiation. Protons could also be accelerated by these highly relativistic winds emitted by the rotating neutron star, leading subsequently to the production of neutrinos [GS06].

Magnetars

Magnetars are neutron stars with very strong surface magnetic fields in the order of $B_s \sim 10^{17}$ G. They are powered by decaying magnetic fields and rotate in the order of seconds. These objects could accelerate protons from the polar cap region above the photomeson threshold, which would allow for the production of neutrinos [Z$^+$03].

2.2.2. Extragalactic source candidates

The experimental basis to predict the existence of extragalactic neutrino sources is the observation of extremely high energy cosmic rays, which can not be confined inside our galaxy. These sources are grouped into Active Galactic Nuclei (AGNs) and Gamma Ray Bursts (GRBs). In the analyses presented in this thesis only AGNs are discussed. Due to their special transient nature, GRBs are analyzed elsewhere [Rot09, A$^+$10a].

Active Galactic Nuclei

Active Galactic Nuclei (AGNs) [UP95, CO96] are among the brightest and most distant objects in the universe, with an observed luminosity between $10^{42} - 10^{49}$ erg/s, located at vast distances up to $z \sim 6.4$. In this type of galaxies the central emission out-shines the stars. The central engine is a supermassive black hole ($10^6 - 10^{10}$ solar masses) with an accretion disk rotating around it. The angular momentum flattens the in-falling matter (a few solar masses per year) forming the accretion disk. The efficiency of the accretion mechanism in converting matter into energy is on average in the range from 2% to 15% [BZ03]. Another important characteristic of AGNs, though not a necessary property, is that they show two ultrarelativistic jets moving in opposite directions, perpendicular to the accretion disk. Surrounding the accretion disk, there are gas clouds that produce, in most AGN classes, broad spectral lines. An optically thick torus around the accretion disk and radio-lobes, which extends for several thousands of parsecs at the end of the jets, complete the picture of an AGN. Particles could be

accelerated to high energies at shocks in the accretion flow, close to the black hole, or at internal shocks in the relativistic jets far from the black hole [RBRD07].

AGNs unify [UP95] different classes of galaxies which have the same internal structure, but that look different to us according to their orientation towards Earth. Other different properties include: spectral index, radio-frequency component (radio-quiet or radio-loud), luminosity (low-luminous: Seyferts, highly luminous: quasars), optical spectral lines (broad spectral lines: Type 1 AGN, narrow-lines: Type 2 AGN), accretion rate and mass of the central black hole. Some of the sub-classes are listed below:

- **Radio Galaxies** (RG): Gigant elliptical galaxies with strong radio emission and steep radio spectrum ($\nu^{-0.8}$). They have extended radio lobes.
- **Fanaroff-Riley Type I/II** (FR I/II): They are radio galaxies showing prominent smooth jets that end in large-scale radio-lobes (hotspots). Type I and II correspond to a division in luminosity, FR-II being more luminous in radio.
- **Quasi-stellar objects** (QSO): Also called quasars, are compact powerful AGNs sub-divided into HPQ (highly polarized quasar) and LPQ (low-polarized quasar), with the division at 3% of polarization [MS81]. They can be also categorized into FSRQ (Flat spectrum radio quasars) or SSRQ (steep spectrum radio quasars), depending on the radio spectral index, α, given a power-law spectrum ($\nu^{-\alpha}$) of the frequency, ν, with the division set at $\alpha = 0.5$. FSRQs have strong atomic emission lines in their spectra.
- **Seyfert**: They are believed to be low-luminosity, nearby AGNs with very broad nuclear spectral line emissions from ionized gas. Most of them are spiral galaxies.
- **Blazars**: They are blazing quasars with one of its relativistic jets pointing towards Earth, thus mainly the emission from the jet region is observed. The radiation from the jet is relativistically beamed because the matter is moving at velocities close to the speed of light. Given the time dilation caused by the relativistic effects, the observed speed of release of energy is faster than at the blazars rest frame. Therefore the photon flux can vary abruptly in short periods of time (from minutes to days). The subclass of BL Lac objects show a featureless continuum spectrum due to the strong emission from the jet that out-shines the spectral lines.

The spectral energy distribution (SED) of AGNs presents three characteristic components. A non-thermal component, from radio wavelengths through optical/UV frequencies in quasars and to X-rays for BL Lacs, can be attributed to synchrotron radiation, in which relativistic electrons spiral around magnetic fields. If the individual electron spectra are integrated, they form a power-law spectrum ($F_\nu(\nu) \propto \nu^{-\alpha}$). At a transition frequency about 10^{12} Hz a synchrotron self-absorption process starts, where the plasma of spiraling electrons becomes opaque to its own synchrotron radiation [CO96].

A second component of thermal origin shows two peaks in their energy output: one at infra-red frequencies (IR-bump) and one at ultra-violet/optical frequencies (UV/optical/blue bump). This component is associated with the black body radiation of a normal galaxy and is thought to be generated from compact dust distribution (torus) and from the gas in the accretion disk, for each peak respectively. Nevertheless, this feature is not prominent compared to the other two non-thermal components.

The third component, mostly present in blazars, in the energy range of MeV-TeV, can be explained by leptonic and hadronic models, which also try to fit the other components of the SED. According to leptonic jet models, inverse Compton scattering [2] is responsible for the observed radiation at X-rays and γ-rays. In this framework, relativistic electrons dominate the radiative signatures of the jet. The target photons for the accelerated electrons could come from the synchrotron radiation, from external photons from the accretion disk, from the surrounding dust, etc. In hadronic models, accelerated protons collide with the surrounding radiation, gas clouds, or other protons, generating subsequently among other particles neutral pions which decay into high energy γ-rays. Also charged pions would be generated which would lead finally to neutrinos, that are a unique signature of this class of models (see Sec. 2.4). The origin of the high energy SED component could be determined with extended observations of γ-rays or of neutrinos. The detection of the latter ones would undoubtedly confirm the validity of hadronic models.

Gamma-Ray Bursts

Gamma-Ray Bursts can be classified according to their duration into long-duration GRBs ($\Delta t \gtrsim 2$ s) and short-duration GRBs ($\Delta t \lesssim 2$ s). Long ones are believed to emerge from the core collapse of a massive star[3] into a black hole, while short ones are thought to result from merging two compact objects (e.g. neutron stars) into a black hole [A$^+$10a].

The fireball shock model explains the production of high energy emission in GRBs. In this model, the prompt γ-rays are originated by expanding shocks in the plasma expelled from a finite-time relativistic jet. These outflows are produced by the merging of neutron stars or by the formation of a black hole. In this environment protons could also be shock-accelerated, leading to the production of neutrinos after the interaction with ambient radiation or plasma material [RBRD07].

2.3. Acceleration Mechanism

Protons can be accelerated stochastically by shock waves in the jets of AGNs in the energy range of PeV-EeV, following the Fermi model, which leads to a power-law spectrum $E^{-\gamma}$. In the standard case $\gamma = 2$ is achieved by strong shocks, though the spectral index has a wide range and its value depends on the shock compression ratio (i.e. ratio between the upstream (u_u) and downstream (u_d) velocities of the magnetic turbulent structures) [RBRD07]:

$$\gamma = \frac{\frac{u_u}{u_d} + 2}{\frac{u_u}{u_d} - 1} \ , \tag{2.1}$$

where $1 < \frac{u_u}{u_d} \leq 4$. It can have values lower than 2, if non-linear effects are included, like strong shock modifications.

The diffusive shock acceleration mechanism that produces the power law spectrum includes the plasma motion, the particle diffusion along magnetic fields and the adia-

[2] When a photon gains energy transferred by a colliding electron.

[3] Starts with less than $\sim$20 solar masses and above the Chandrasekhar limit would produce a neutron star. Therefore, more massive stars are needed to produce a black hole and consequently a GRB.

batic energy gains and losses of the charged particle. In the first order Fermi acceleration [Fer49], the energy gain in each shock is proportional to the velocity of the shock and $\gamma \geq 2$. The charged particle gains energy through multiple reflections inside a shock wave due to the magnetic inhomogeneities, which can change its directions from upstream to downstream of the shock and vice versa. However, only particles with energies exceeding the thermal energy can enter the shock wave and start the acceleration process.

Since an astrophysical source (e.g. AGN) has a maximum attainable energy, E^{thr}, an energy cut-off should be added to take this property into account:

$$\frac{d\Phi_\nu}{dE_\nu} \propto E_\nu^{-\gamma} \exp\left(-\frac{E_\nu}{E^{thr}}\right) \quad . \tag{2.2}$$

Another possible acceleration mechanism [RA08], which does not involve shock acceleration in the jets, can be present in low-luminous, non-blazar AGNs (e.g. M87). The acceleration can happen at the base of the rotating jet magnetosphere (close to the central black hole). There, particles would be centrifugally accelerated, gaining rotational energy while moving outwards along the rotating magnetic field lines.

2.4. Neutrino Production

Extraterrestrial neutrino production is predicted by hadronic models for the aforementioned source candidates. There are two essential factors for this production: proton (nucleon) acceleration in stochastic processes up to very high energies (subsequently requiring strong magnetic fields, extended acceleration regions and/or supermassive black holes) and a certain density of target photons (internal photons, mainly from synchrotron origin, or from an external radiation field) or plasma material (nucleons).

The main particle interactions that lead to the generation of neutrinos are:

$$\begin{aligned} p\gamma &\rightarrow \Delta^+ \rightarrow n\pi^+ \\ n\gamma &\rightarrow \Delta^0 \rightarrow p\pi^- \\ pp &\rightarrow p\Delta^+ \rightarrow pn\pi^+ \\ np &\rightarrow p\Delta^0 \rightarrow pp\pi^- \end{aligned}$$

The first two correspond to photonuclear interactions, while the last two are inelastic nuclear collisions. In all cases, a proton minimum energy (bounded to the target particle's energy) is required for the production of the short-lived delta, Δ(1232 MeV). For example, for a UV photon with energy $E \sim 30$ eV, the proton needs an energy around 10^{16}eV. Then the produced neutrinos will have an energy of $\sim 5 \times 10^{14}$eV.

The delta resonance decays, almost exclusively (99%), fastly ($\sim 10^{-24}$ s), via the

strong force, into a nucleon and a pion. The charged pions decay producing neutrinos:

$$\begin{aligned} \pi^+ &\rightarrow \mu^+ \nu_\mu \rightarrow e^+ \nu_e \bar{\nu_\mu} \nu_\mu \\ \pi^- &\rightarrow \mu^- \bar{\nu_\mu} \rightarrow e^- \bar{\nu_e} \nu_\mu \bar{\nu_\mu} \\ n &\rightarrow p e^- \bar{\nu_e} \end{aligned}$$

The occurrence of these processes depends on each source and the model adopted. Usually, the pion photoproduction ($p\gamma$) is the main channel. It was estimated [SS96] that pp collisions (*blob-blob*) would account for ∼10% of produced neutrinos in AGN.

Proton-photon interactions are the most studied case. In this scenario, a proton resonance $\Delta^+(1232)$ is produced, which then decays into $N\pi$ ($\frac{2}{3} : \pi^0 p$, $\frac{1}{3} : \pi^+ n$). The photo-production cross section at the resonance peak is $\sigma_{p\pi\rightarrow\Delta} \simeq 10^{-32}\mathrm{m}^2$. The photo-produced pions give rise in the neutral case to γ-rays ($\pi^0 \rightarrow 2\gamma$, 98.79% branching ratio) and through the charged branch to neutrinos ($\pi^+ \rightarrow \mu^+ \nu_\mu \rightarrow e^+ \nu_e \bar{\nu_\mu} \nu_\mu$, 99.98% branching ratio). The latter decay chain produces a neutrino flux: $\nu_e : \nu_\mu : \nu_\tau = 1 : 2 : 0$. If the surrounding medium is optically thick, the charged pions will still decay promptly but the muons will be absorbed (charged current interaction) before decaying. In such scenarios the neutrino ratio is $\nu_\mu : \nu_e : \nu_\tau = 1 : 0 : 0$.

The energy of neutrinos from proton-photon interactions can be expressed as a function of the parent proton energy by: $\langle E_\nu \rangle = \langle x_{p\rightarrow\pi^+} \rangle \langle x_{\pi\rightarrow\nu_\mu} \rangle \langle E_p \rangle$, where $\langle x \rangle$ is the average fraction of the transferred energy. Numerically this is equivalent to: $E_\nu \approx \frac{1}{4} E_\mu \approx \frac{1}{4} \left(\frac{1}{5} E_p\right) = \frac{1}{20} E_p$. For proton-proton collisions the energy of the proton that goes into the pion is $\frac{1}{3} E_p$, thus $E_\nu \approx \frac{1}{12} E_p$.

The γ-ray and neutrino fluxes can be related by the following expression [AMH02]:

$$\int_{E_\gamma^{min}}^{E_\gamma^{max}} E_\gamma \frac{d\Phi_\gamma}{dE_\gamma} dE_\gamma = K \int_{E_\nu^{min}}^{E_\nu^{max}} E_\nu \frac{d\Phi_\nu}{dE_\nu} dE_\nu \ , \tag{2.3}$$

where K depends on whether the pions are coming from $p\gamma$ interactions ($K = 4$) or from pp collisions ($K = 1$). However, this relations holds only after production at the source. The observed fluxes, specially of γ-rays are different to those predicted at the source due to absorption while travelling towards Earth.

2.5. Neutrino oscillations

Neutrinos produced at astrophysical sources travel astronomical distances without being deflected by magnetic fields. Their flux is kept almost constant until they reach Earth, because they seldom interact in their propagation through space. The only difference between the produced neutrinos and the ones arriving at Earth is their flavor composition due to oscillations during propagation.

The calculation of the vacuum oscillation probability is simplified since the oscillation length is very small compared to the distances between the astrophysical sources and Earth ($\delta m^2 \times \frac{L}{E} \gg 1$). Therefore the relative phases between the propagating mass eigenstates are washed out and the neutrinos become an incoherent mixture of mass eigenstates. Considering three neutrino species and based on the constraints from the solar, atmospheric and reactor neutrino data, the following values for the elements of

the neutrino mixing matrix can be assumed: $|U_{e3}|^2 \ll 1$ and $|U_{\mu 3}| \simeq |U_{\tau 3}|$ [A$^+$00], in order to calculate the final ratio of the astrophysical neutrino flux.

Taking into account the previous considerations, if the initial flux ratio is $\Phi_{\nu_e} : \Phi_{\nu_\mu} : \Phi_{\nu_\tau}$ (1:2:0), after oscillations it becomes (1:1:1) [B$^+$03]. Therefore in the case of muon neutrinos, only half of the produced neutrinos would be observable at Earth.

2.6. Expected neutrino fluxes

There are several predictions of astrophysical neutrinos from specific sources and also for diffuse fluxes. The sensitivity range of present experiments starts to be within the reach of these fluxes, thus it might be possible to either rule them out or confirm them. Some examples of astrophysical neutrino flux predictions follow.

It is possible to predict a neutrino flux upper limit (per flavor) for Centaurus A, a close-by extremely bright radio galaxy. This prediction is based on Auger observations from Centaurus A (initial proton flux input) and HESS gamma-ray flux limits[4]. One model [HO08] gives the following prediction:

$$\frac{dN_\nu}{dE} \leq 5 \times 10^{-13} \left(\frac{E}{\mathrm{TeV}}\right)^{-2} \mathrm{TeV}^{-1}\mathrm{cm}^{-2}\mathrm{s}^{-1} \ . \tag{2.4}$$

This would mean 0.8 events per year expected in 1 km^2 effective muon area detector for an E^{-2} initial neutrino flux at the source. Another model [CH08] predicts also less than one event (0.4-0.6 events) per year in the same type of detector, above a threshold energy of 100 TeV. For a detection of this source in neutrinos, several years of observation should be necessary.

A diffuse flux can be also calculated assuming similar characteristic luminosities for the same kind of FRI radio galaxies, using their density function and assuming they are uniformly distributed within their horizon. These calculations [HO08] give a diffuse flux of:

$$2 \times 10^{-9} \left(\frac{E}{\mathrm{TeV}}\right)^{-2} \mathrm{TeV}^{-1}\mathrm{cm}^{-2}\mathrm{s}^{-1}\mathrm{sr}^{-1} \ , \tag{2.5}$$

with corresponding 19 expected events per year in the Northern sky for a similar detector.

A well know upper bound on the high energy neutrino flux from cosmic ray observations was obtained by Waxman & Bahcall [WB01] for neutrinos produced in $p-\gamma$ or $p-p(n)$ interactions. The sources of these neutrinos should be optically thin to photo-meson or nucleon-meson interactions, so that protons can escape. An upper limit to the astrophysical proton production rate can be set. Using this limit a conservative upper bound to the neutrino flux can be derived. The value of this limit is set to $E_\nu^2 \Phi_\nu < 2 \times 10^{-8}\mathrm{GeV/cm}^2\mathrm{s\ sr}$. For GRBs, in the energy range $10^{14}\mathrm{eV} < E < 10^{16}\mathrm{eV}$, it is $E^2 dN/dE \sim 0.3 \times 10^{-8}\mathrm{GeV/cm}^2\mathrm{s\ sr}$. Current measurements with ICECUBE in its 40 string configuration have reached this limit for GRBs, though no signal has been found yet. If the optical depth, τ (dimensionless measurement of the transparency of the medium), is smaller than expected, the upper bound would overestimate the most likely neutrino flux by a factor of $5/\tau$ [WB01].

[4] After the article with the predictions [HO08] was published, HESS discovered a faint very high energy γ-ray emission from Centaurus A [A$^+$09f].

2.7. Multi-messenger astronomy

According to present models of neutrino production in astrophysical sources, neutrino emission is connected with high energy photons and protons fluxes from the same sources. Therefore correlation studies between these observations is natural. This kind of analysis is also referred as multi-messenger astronomy. Since many γ-ray telescopes have a small field of view (e.g. Imaging Atmospheric Cherenkov Telescopes (IACTs) like MAGIC, HESS and Veritas have a typical 4^o diameter field of view), they cannot look at a wide region of sources at the same time as in the case of neutrino (all-sky) or cosmic ray (an hemisphere) detectors. In addition, IACTs have an overall duty cycle of around $\sim$ 15%. On the other hand, satellite telescopes like Fermi have a field of view of about 20% of the sky and are taking data continously, however, it covers a lower energy range. Furthermore, water Cherenkov γ-ray observatories like Milagro and the future HAWC can observe an entire half hemisphere all the time, however they have a worse angular resolution ($\sim 1^o$, while for IACTs it is about 0.05^o - 0.1^o).

A time dependent analysis using photon and neutrino offline data enhances the discovery probability by profiting from the photon-neutrino correlation. However, since for many sources there might be missing photon data, due to the reasons given above, an online analysis improves the chances of detection. In case of an online analysis, a significant neutrino observation can trigger the follow-up observations from IACTs. Such Neutrino triggered Target of Opportunity (NToO) programs have been carried out between AMANDA-II and MAGIC [A$^+$07b] and are planned for ICECUBE and MAGIC [FB09]. In case of cosmic ray observations, as for neutrino detectors, a large area of the sky is constantly covered, thus correlation studies are done offline [Lau10].

3. High Energy Neutrino Detection

Sieh dir einen Menschen genau genug an,
so weisst du mehr von ihm als er selber.
Hermann Hesse 1877-1962
Demian

The same characteristic that makes neutrinos unique for carrying information from the deep universe, makes them difficult to detect. They have an extremely low cross-section and interact only via the weak force. Given this very low interaction probability, extremely large detector volumes are necessary.

In the present chapter, after a brief description of the principles of a neutrino telescope, the interactions of neutrinos after arriving at the Earth's atmosphere until reaching the detector are described. This includes the neutrino survival probability and the probability to interact near the detector, the subsequent muon propagation and Cherenkov light production and propagation. In addition, the different classes of background are described. The focus will be given to ν_μ because, in its charged current interaction, it produces a muon that can be detected and reconstructed with a good angular resolution, necessary for point source studies.

3.1. Neutrino telescope principle

A realistic solution to the high-energy neutrino detection problem is to use a natural clear extended medium, like large volumes of water (lakes or seas) or ice. Water or ice are used as target material to convert neutrinos into charged leptons (e.g. muons). In this kind of medium it is possible to indirectly detect neutrinos by recording the Cherenkov light cone produced by the charged leptons created in neutrino-nucleon charged current interactions. The Cherenkov light can propagate through water or ice and can be detected by photomultiplier tubes. Furthermore, given the considerable background produced by cosmic rays, it is necessary that the detector should be located at large depths, so that the thick layer of water or ice can act as a shield from penetrating atmospheric muons.

The structure of such a detector should be a 3-dimensional array of photomultipliers that collect the Cherenkov light. Given a good timing resolution from the electronics and using the recorded charge, the direction and energy of the leptons can be reconstructed. In case of muons, a good angular resolution ($< 1^o$) is achieved, while the energy estimation has an error of 0.3 log(E[GeV]). The properties of electron-neutrino and low energy tau-neutrino induced events (cascades) are inverted with respect to those from muon-neutrinos, having a better energy resolution (0.1-0.2 log(E[GeV])), but poor angular resolution ($> 30^o$ in ice) [M$^+$09b].

3.2. Neutrino-induced events

Using a simplified approach an expression can be written to calculate the number of muon events induced by $\nu_\mu + \bar{\nu}_\mu$ detectable in a generic neutrino telescope as:

$$N_\mu = T \int d\Omega \int dE_{\nu_\mu} \frac{d\phi_{\nu_\mu}}{dE_{\nu_\mu}} \cdot A_{eff}(E_{\nu_\mu}, \theta) \cdot P_{surv}(E_{\nu_\mu}, \theta) \cdot P_{int}(E_{\nu_\mu}, E_\mu^{thr}) \ , \tag{3.1}$$

where T is the exposure time, $\frac{d\phi_{\nu_\mu}}{dE_{\nu_\mu}}$ is the differential flux of muon neutrinos, which is assumed to be $\propto E_{\nu_\mu}^{-2}$ (standard case), A_{eff} is the detector effective area which includes the global detector efficiency, θ is the zenith coordinate, $P_{surv}(E_{\nu_\mu}, \theta)$ is the neutrino survival probability while traversing the Earth, and $P_{int}(E_{\nu_\mu}, E_\mu^{thr})$ is the probability that the muon, which was produced in a charged current interaction, interacts near the detector and reaches it, before loosing its energy below the detector threshold (E_μ^{thr}).

3.2.1. Survival probability

The survival probability of a neutrino not being absorbed in the Earth is given by [G+98]:

$$P_{surv}(E_{\nu_\mu}, \theta) \equiv \exp\left[-\frac{\chi(\theta)}{L_{int}^{tot}(E_{\nu_\mu})}\right] \ , \tag{3.2}$$

where $\chi(\theta)$ is the column density and $L_{int}^{tot}(E_{\nu_\mu})$ is the total interaction length, considering both neutral and charged current interactions. The column density is obtained by:

$$\chi(\theta) \equiv \int_0^{l_{\nu_\mu}(\theta)} \rho(r(\theta, l)) dl \ , \tag{3.3}$$

where l_{ν_μ} is the distance traveled by the neutrino inside the Earth until reaching the detector at a certain depth and $\rho(r)$ is the Earth's density that is integrated along the path of the neutrino. The Preliminary Reference Earth Model (PREM) [DA81] defines average values for this density. The total interaction length is given by:

$$L_{int}^{tot}(E_{\nu_\mu}) \equiv \frac{1}{\sigma_{\nu N}^{tot}(E_{\nu_\mu}) N_{Av}} \ , \tag{3.4}$$

where $\sigma_{\nu N}^{tot} = \sigma_{\nu N}^{cc} + \sigma_{\nu N}^{nc}$ is the inclusive cross section, that includes contributions from charged and neutral current interactions and N_{Av} is the Avogadro number.

Neutrino-Nucleon cross-section

These two types of neutrino-nucleon (neutrino-quark) interactions via weak force can be written in general as:

$$(\nu_l, \bar{\nu}_l) + N \xrightarrow{W^\pm} (l^-, l^+) + X \qquad \text{charged-current (CC)}$$

$$(\nu_l, \bar{\nu}_l) + N \xrightarrow{Z^o} (\nu_l, \bar{\nu}_l) + X \qquad \text{neutral-current (NC)}$$

where l represents the flavor of the lepton (a muon in our case), $N \equiv \frac{n+p}{2}$ is an isoscalar nucleon (combination of neutron (n) and proton (p)) and X represents the nuclear remnant and the associated hadronic cascade originated by the hadronization of the target nucleon. The type of interaction is determined by the boson ($W^{\pm}$ or Z^{o}) that mediates it.

Depending on the neutrino energy, the interaction can be either an elastic scattering, where the nucleon form factors are suitable to describe the process, or for higher energies an inelastic scattering, where the parton density functions describe the nucleon quark structure. In this work the neutrino energies correspond to a deep inelastic scattering. An example of a CC neutrino-nucleon interaction can be represented using a Feynman diagram as shown in Fig. 3.1. The cross-section (see Fig. 3.2) increases nearly linearly with energy up to ∼10 TeV and then, up to E_ν ∼10^{21} eV, rises more slowly [LM00]. It is roughly the same for neutrinos and anti-neutrinos, numerically [G$^+$98] (for 10^{16} eV $\leq E_\nu \geq 10^{21}$ eV):

$$\sigma_{cc}(\nu N) \approx \sigma_{cc}(\bar{\nu} N) = 5.53 \times 10^{-36} \mathrm{cm}^2 \left(\frac{E_\nu}{1\mathrm{GeV}}\right)^{0.363} \tag{3.5}$$

$$\sigma_{nc}(\nu N) \approx \sigma_{nc}(\bar{\nu} N) = 2.31 \times 10^{-36} \mathrm{cm}^2 \left(\frac{E_\nu}{1\mathrm{GeV}}\right)^{0.363} \tag{3.6}$$

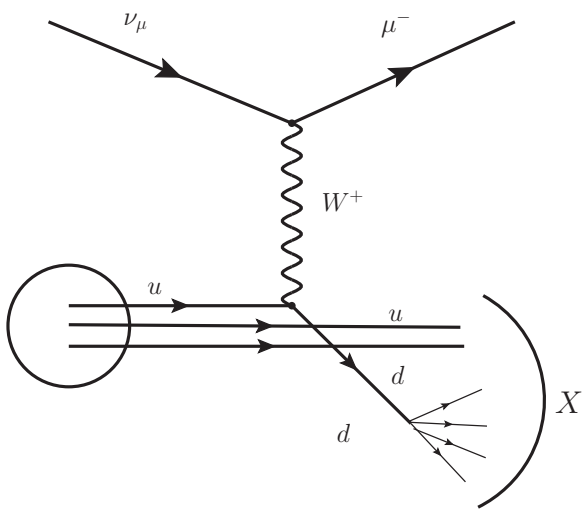

Figure 3.1.: Example of a Feynman diagram for a charged current neutrino-nucleon interaction in a deep inelastic regime.

3.2.2. Interaction probability

The probability that a muon neutrino produces a muon that reaches the detector with an energy that is still observable is expressed as [G$^+$98]:

$$P_{int}(E_{\nu_\mu}, E_\mu^{thr}) \equiv 1 - \exp\left[\frac{\left\langle R(E_{\nu_\mu}, E_{mu}^{thr})\right\rangle}{L_{int}^{cc}(E_{\nu_\mu})}\right] \approx N_{Av}\sigma_{cc}(E_{\nu_\mu})\left\langle R(E_{\nu_\mu}, E_\mu^{thr})\right\rangle \ , \tag{3.7}$$

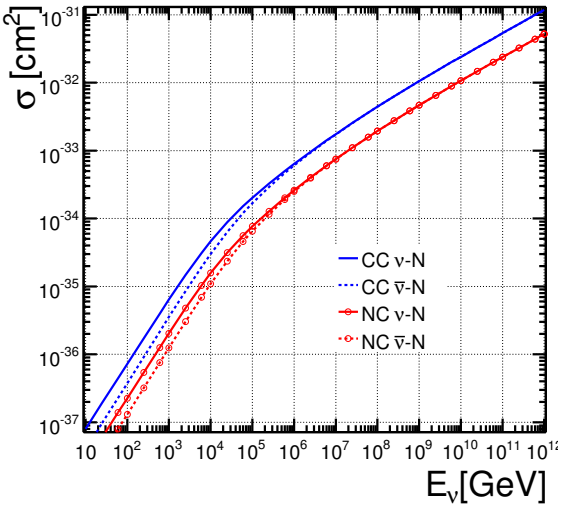

Figure 3.2.: Cross sections for νN and $\bar{\nu}$N interactions as a function of energy for charged and neutral current interactions (data taken from [G$^+$98]).

where N_{Av} is Avogadro's number, σ_{cc} is the neutrino charged current cross section and $\left\langle R(E_{\nu_\mu}, E_\mu^{thr}) \right\rangle$ is the average muon range obtained by:

$$\left\langle R(E_{\nu_\mu}, E_{mu}^{thr}) \right\rangle \equiv \frac{1}{\sigma_{cc}(E_{\nu_\mu})} \int_0^{1-\frac{E_{mu}{}^{thr}}{E_{\nu_\mu}}} dy \frac{d\sigma_{cc}}{dy}(E_{\nu_\mu}, y) R(E_{\nu_\mu}(1-y), E_\mu^{thr}) \ , \tag{3.8}$$

where $y = \nu / E_\nu$ is a Bjorken scaling variable, with $\nu = E_\nu - E_\mu$ the energy loss in the laboratory frame and E_μ^{thr} is the detector's energy threshold.

Muon energy loss

The muon range can be written in a simplified way as:

$$R(E_\mu, E_\mu^{thr}) = \frac{1}{b} \ln \frac{a + bE_\mu}{a + bE_\mu^{thr}} \ , \tag{3.9}$$

which comes from the energy-loss relation:

$$-\frac{dE_\mu}{dx} = a(E_\mu) + b(E_\mu)E_\mu \ , \tag{3.10}$$

where the coefficient a=2.0$\times 10^{-3}$ GeV cmwe^{-1} represents the energy losses by ionization and b=3.9$\times 10^{-6}$cmwe^{-1} adds up the fractional energy loss from radiative processes (i.e. Bremsstrahlung, pair production (e$^+$, e$^-$), photo-production).

For an accurate estimation, where a and b are not longer energy independent, a muon propagation simulation is necessary (see for example [LS91]). The ionization loss grows logarithmically with energy. Up to 10 TeV the energy limit, where b is constant, is not yet reached. For energies greater than a few TeV the radiative losses start to dominate and fluctuations appear, because the energy loss is no longer constant.

3.3. Cherenkov Effect

The charged particles, created in neutrino-nucleon charged current interactions, will travel through a polarizable dielectric material (electrical insulator, i.e. ice). If they have a velocity faster than the phase velocity of light in such medium, Cherenkov photons [Che37] are produced. The process occurs because the charged particles polarize the atoms, which in turn return to their ground states emitting photons. The photons are emitted perpendicular to the conical coherent radiation wavefront that moves along the axis of the particle's trajectory. The Cherenkov photons describe an angle θ_c with the particle's track given by:

$$\cos(\theta_c) = \frac{1}{\beta n} \ , \tag{3.11}$$

where $\beta = v/c > 1/n$ and n is the refraction index of the medium, which for ice or water is $n = 1.33$, thus for a relativistic particle ($\beta \approx 1$) the Cherenkov angle is $\theta_c \approx 41^o$.

The Frank-Tamm formula for the Cherenkov effect gives the spectral distribution of the emitted photons by:

$$\frac{dN}{dxd\lambda} = \frac{2\pi\alpha}{\lambda^2}\left(1 - \frac{1}{\beta^2 n(\lambda)^2}\right) \ , \tag{3.12}$$

where λ is the photon's wavelength and $\alpha \sim 1/137$ is the fine structure constant. From Eq. 3.12 it can be calculated that a relativistic muon will produce around 3×10^4 photons/meter while traveling in ice in the spectral range 300-600 nm (visible to the ICECUBE detector, see Chapter 4). These photons are observed by photomultiplier tubes.

3.4. Background

The search for astrophysical neutrinos has to cope with an extremely large background, which is six orders of magnitude larger than the expected neutrino signal flux. In this section the different types of background are described, as well as how they are generated. The background is mainly composed of atmospheric muons produced by cosmic rays. Once the atmospheric muon background is removed, a second type of background, consisting of atmospheric neutrinos, becomes relevant.

3.4.1. Atmospheric muons

Primary cosmic rays reach the Earth's upper atmosphere, where they interact with air nuclei. As a result of this interaction, secondaries are produced, mainly pions, but also kaons and other particles. Atmospheric muons are produced, if they have not interacted before, by the decay of these charged mesons. The main decay channels leading to muons [A$^+$08] are listed next, where the branching ratios are quoted in parenthesis (the charge conjugated decay modes should also be considered).

$$
\begin{aligned}
\pi^+ &\longrightarrow \mu^+ + \nu_\mu && (99.98\%)\\
K^+ &\longrightarrow \mu^+ + \nu_\mu && (63.55\%)\\
&\longrightarrow \pi^+ + \pi^o && (20.66\%)\\
&\longrightarrow \pi^+ + \pi^\pm + \pi^\mp && (5.59\%)\\
&\longrightarrow \pi^o + \mu^+ + \nu_\mu && (3.35\%)
\end{aligned}
$$

The flux of high energy atmospheric muons observed in IceCube, deep in the ice, is subject to temperature variations in the middle stratosphere. These yearly and daily changes are observed as seasonal oscillations on the level of $\pm 10\%$ [T$^+$09]. During winter, the stratosphere is cold and dense, making it more likely for the charged mesons to interact and produce secondary low energy particles (less high energy muons). On the contrary, during summer, the stratosphere is warmer, thus less dense, allowing mesons to decay more often rather than to interact, which results in more high energy muons.

3.4.2. Atmospheric neutrinos

The atmospheric neutrino spectrum can be roughly modelled by a power-law: $E^{-3.7}$ for $E > 1$ TeV [GHS95]. The seasonal effect for atmospheric neutrinos is less than 1% [AB05]. The theoretical uncertainty in the atmospheric neutrino flux ranges from 7% to 25% depending on energy. They can be subdivided into two categories: conventional and prompt atmospheric neutrinos.

Conventional atmospheric neutrinos

Conventional atmospheric neutrinos (ν_e,ν_μ) are produced by the decay of muons (μ), pions (π) and kaons (K). The muon decay contribution is considerable up to a few GeV, while charged pion and kaon decays are still important at 10-100 TeV.

The Honda model [H$^+$07] is used in this thesis. This model modifies the spectral index of primary cosmic ray protons from -2.71 to -2.66 above 100 GeV. Below 100 GeV, where pions are the main source of atmospheric neutrinos, the predictions, based on data, are robust. At higher energies (E>1 TeV), the uncertainties associated with K production are higher and scarce data are available. The estimated uncertainty for this model is subdivided for energy regions: $\sim$ 7% from 1 to 10 GeV, $\sim$ 14% at 100 GeV, and $\sim$ 25% at 1 TeV [H$^+$07].

Prompt atmospheric neutrinos

Prompt atmospheric neutrinos, important in the energy region from 100 TeV to 10 PeV, are produced by the semi-leptonic decay of hadrons that contain charm quarks, mainly D-mesons ($D \rightarrow K + \mu + \nu$) and Λ_c^+ particles ($\Lambda_c \rightarrow \Lambda_0 + \mu + \nu$). The corresponding energy spectrum is harder than for conventional neutrinos, i.e. $\sim E^{-2.7}$. Even though its production rate is low, they still represent a considerable background in high energy searches of neutrinos.

In this thesis the Naumov model [FNV01] is used in the atmospheric neutrino simulation. The cross section applied for charm production in interactions of nucleons and pions with light nuclei is taken from the RQPM (Recombination Quark Parton Model).

4. The ICECUBE Observatory

Ich wünsche zu wissen, wer Sie eigentlich seien
und woher Sie kommen und wohin Sie wollen?
Gottfried Keller 1819-1890
Kleider machen Leute

The ICECUBE Neutrino Observatory [A$^+$01a, A$^+$06a] is a kilometer-scale neutrino telescope located at the geographic South Pole. It consists of three sub-detectors: ICECUBE (see Sec. 4.1.1), ICETOP (see Sec. 4.1.2) and DEEPCORE (see Sec. 4.1.3), described below. Its principal detector component is an optical sensor called digital optical module (DOM) (see Sec. 4.2), which contains a large area photomultiplier tube (PMT) that detects the Cherenkov light (see Sec. 3.3) produced by charged particles. In total there will be 5484 installed DOMs (ICECUBE:4680, ICETOP: 324 and DEEPCORE: 480). In the case of ICECUBE and DEEPCORE the DOMs are positioned along strings deep inside the Antarctic ice, while ICETOP DOMs are housed inside tanks at the surface. Fig. 4.1 shows the 3D view of the ICECUBE Observatory, where the different depths are emphasized. An schematic top view of the placement of the sub-detectors' components is shown in Fig. 4.2. The energy ranges that the sub-detectors cover are sketched in Fig. 4.3.

Its construction began in the austral summer of 2004/2005. Each year additional components are deployed. The historical deployment in number of strings, stations and DOMs by season is shown in Table 4.1. Currently $\sim$ 92% of the detector is deployed. Next season, 2010/11, the ICECUBE Neutrino Observatory will be completed.

Deployment Season	Name (code)	ICECUBE Strings	ICETOP Stations	DEEPCORE Strings	Total DOMs
2004/05	IC1 / IT4	1	4	0	76
2005/06	IC9 / IT16	8	12	0	528
2006/07	IC22 / IT26	13	10	0	820
2007/08	IC40 / IT40	18	14	0	1136
2008/09	IC59 / IT59	18	18	1	1212
2009/10	IC79 / IT73	15	15	5	1260
2010/11	IC86 / IT81	5	8	2	452
Total		78	81	7	5484

Table 4.1.: Historical and future deployment by season of the total number of strings, stations and DOMs for the different sub-detectors of the ICECUBE Neutrino Observatory.

Research and development (R&D) studies to extend the energy range beyond EeV energies are underway. They include radio (AURA: Askaryan Under-ice Radio Array) and acoustic (SPATS: South Pole Acoustic Test Setup) techniques.

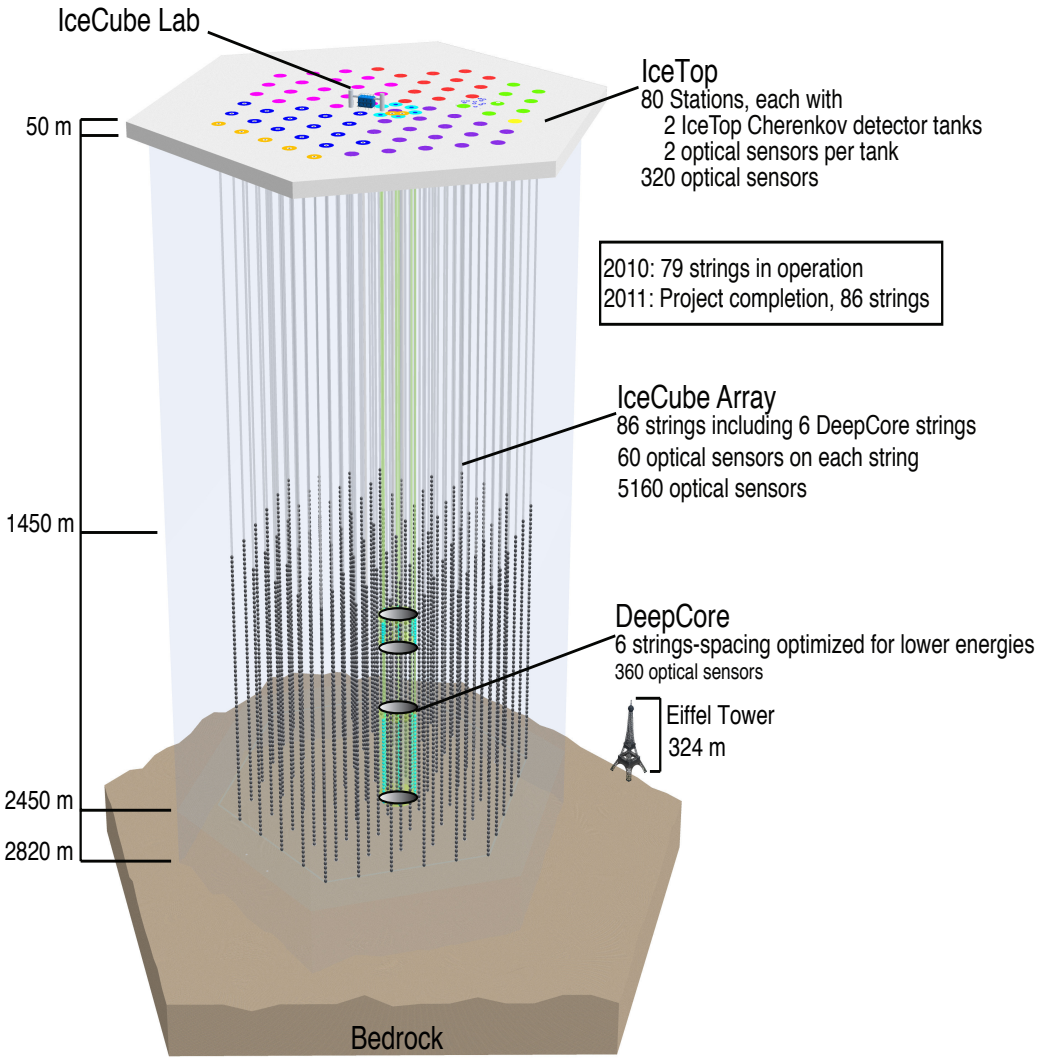

Figure 4.1.: Side 3D view of the complete ICECUBE Observatory highlighting its sub-detectors: ICECUBE, ICETOP and DEEPCORE [Mal10].

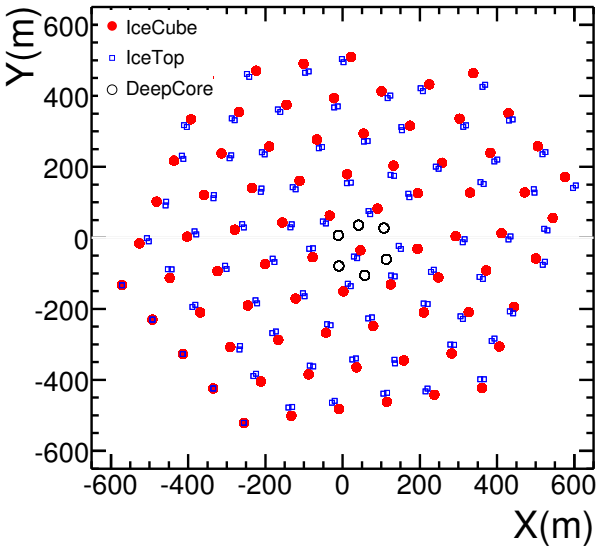

Figure 4.2.: Top view of the complete ICECUBE Observatory highlighting its sub-detectors: ICECUBE (filled circles), ICETOP (squares) and DEEPCORE (open circles).

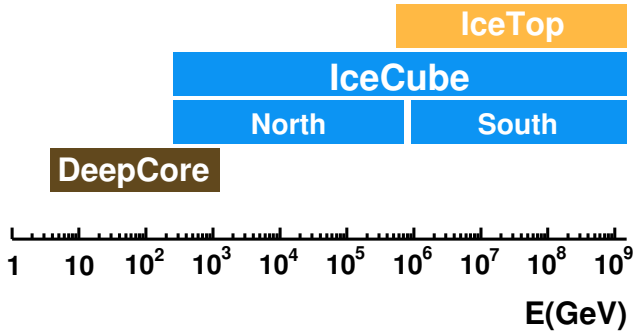

Figure 4.3.: Diagram of the most sensitive energy regions of ICECUBE Observatory's sub-detectors. In the case of ICECUBE and DEEPCORE the energy correspond to neutrinos and for ICETOP it represents the air shower energy. For ICECUBE the Northern and Southern hemispheres cover different energy regions.

Other neutrino telescopes and prototypes, which are operating or under development in the Northern hemisphere (complementary to ICECUBE), are briefly summarized next.

The neutrino telescope NT200 [B$^+$97], in the Siberian Lake Baikal (Russia), has been operating since 1998 and in its upgraded version, NT200+, since 2005 [Wis08]. NT200+ is a 10 Mton detector in water, at a depth of 1.1 km, with a negligible background light from K^{40} decay. R&D activities towards a km^3-detector at the same site have been started.

ANTARES (Astronomy with a Neutrino Telescope and Abyss environmental RESearch) [Car08] is an underwater neutrino telescope, which was completed in 2008. It is currently the largest neutrino telescope in the Northern hemisphere, with a surface area of 0.02 km^2, a similar size as AMANDA-II (Antarctic Muon and Neutrino Detector Array) (ICECUBE's precursor, [A$^+$01b]). It is located 40 km offshore from Toulon (France), deep in the Mediterranean sea (at a depth of 2475 m).

NEMO (NEutrino Mediterranean Observatory) (in Capo Passero, Italy) [Mig06] and NESTOR (Neutrino Extended Submarine Telescope with Oceanographic Research) (in Pylos, Greece) [Res06] are pilot projects which are exploring different technologies, deploying small prototypes in the Mediterranean sea at depths between 3 and 4.5 km.

ANTARES, NEMO and NESTOR have joined efforts to form the KM3Net Consortium [KM3]. They are designing a neutrino telescope with a volume of at least one cubic kilometer at the bottom of the Mediterranean sea using high quantum efficiency PMTs. It would be the Northern hemisphere counterpart of ICECUBE.

4.1. Sub-detectors

4.1.1. ICECUBE

ICECUBE, the main detector of the Neutrino Observatory, will contain 4680 DOMs installed on 78 strings[1] (vertical cables), 60 DOMs each, deployed in the Antarctic Ice at depths between 1450 m to 2450 m. The strings are arranged in a hexagonal pattern with a mean interstring spacing of 125 m and vertical separation between DOMs of 17 m. The string separation was chosen in order to improve the detection and muon reconstruction capabilities in the TeV energy region. The layers of ice above the detector work as a partial shield from atmospheric muons.

It is designed to detect astrophysical neutrinos in the energy range from a few 100 GeV up to 10^9 GeV, covering both Northern (TeV-PeV) and Southern skies (PeV-EeV). However, the most sensitive region corresponds to the Northern sky, given the reasons explained in Sec. 3.4. Neutrino-induced events inside or close to the detector are detected by the DOMs that record the Cherenkov light produced by charged leptons as described in Sec. 3.3.

In this work, the data from two ICECUBE configurations are used. These correspond to the 22-string and 40-string configurations which are described below. The following abbreviations will be used throughout the text to refer to these configuration: IC22 (ICECUBE 22-string configuration) and IC40 (ICECUBE 40-string configuration).

[1] There were 80 strings planned in the original proposal. However, two could not be deployed in the specified place because of old debris buried in the ice. These two strings will be used in the DeepCore array.

ICECUBE 22-string configuration (IC22)

During the data taking period from May 31st 2007 to April 5th 2008, ICECUBE was working with a 22-string configuration [Kar07], with the strings positioned at the locations shown in Fig. 4.4. This asymmetric distribution, with a major and minor axis, affects the azimuth exposure.

ICECUBE 40-string configuration (IC40)

From April 5th 2008 to May 19th 2009, ICECUBE took data with a 40-string configuration [Kar08]. The geometry of this configuration is shown in Fig. 4.4. The azimuthal asymmetry is larger for this configuration.

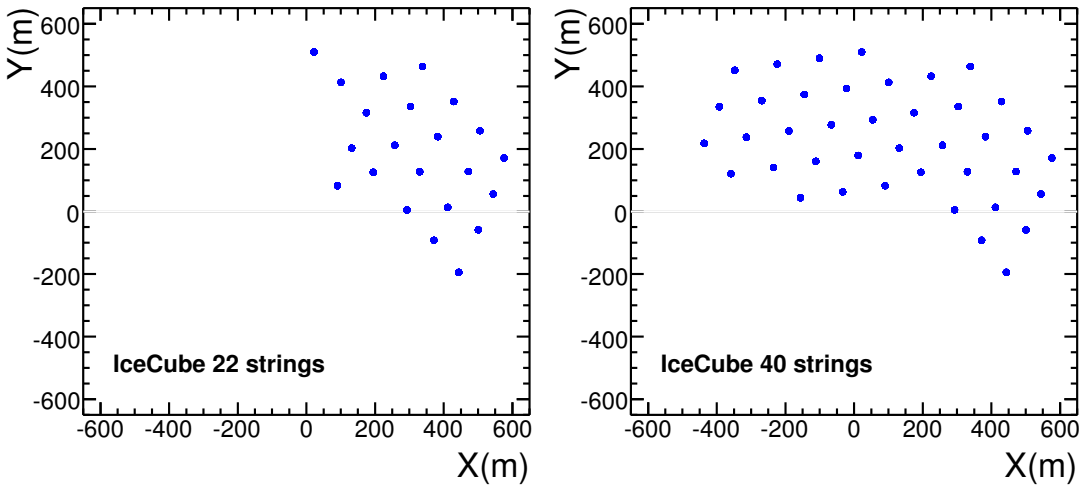

Figure 4.4.: Top view of the ICECUBE detector's strings at intermediate deployment steps: Left: 22 strings (2007/08 season), Right: 40 strings (2008/09 season).

4.1.2. IceTop

ICETOP [Gai07] is an extensive air shower array under construction at the surface of the ICECUBE site. It is located at an altitude of 2835 m (680 g/cm^2). In its final configuration the array will cover a 1 km^2 area, with 81 stations, 78 of them located on top of each ICECUBE string and the rest distributed in the inner region of the ICECUBE array. Each station consists of a pair of cylindrical ice-filled tanks separated from each other by 10 m on average.

Each tank, with surface area of 2.7 m^2 and height of 90 cm, is instrumented with two standard ICECUBE DOMs that record the light produced by charged particles coming from air showers generated in the atmosphere. Each DOM is operating at a different (high or low) gain to extend the dynamic range of the tank. In total there will be 324 DOMs. The tank has a reflective coating on the inside for homogeneously reflecting the induced Cherenkov light. The PMT of the DOM is facing downwards.

Because of its high altitude, ICETOP can observe extensive air showers between 10^{15} eV and 10^{17} eV at the maximum of their development. Therefore, the measured signals

are dominated by the electromagnetic component of the air showers. The effective threshold for ICETOP is about 500 TeV for a trigger requirement of five or more stations. Local coincidence between two tanks at a station is used to discriminate signal showers from random noise coming from uncorrelated photons, electrons or muons.

Among its physics goals are: the measurement of the primary cosmic-ray energy spectrum and the study of its composition in the knee region and above, the calibration of the ICECUBE event reconstruction and vetoing muon background for ICECUBE.

4.1.3. DeepCore

DEEPCORE [Sch08, Wie09] is a low-energy extension of the ICECUBE Neutrino Observatory, which replaces the decommissioned AMANDA-II [A$^+$01b] detector. Its purpose is to enhance the sensitivity of ICECUBE below 1 TeV and to lower the detection threshold below 10 GeV (the nominal threshold for ICECUBE-only is 100 GeV). Therefore it has been designed as a compact Cherenkov detector and located in the clear ice at the bottom center of ICECUBE.

It consists of 6 more densely instrumented strings, each holding 60 high quantum efficiency photomultiplier tubes (HQE PMTs), plus the two pending ICECUBE strings together with the 7 central ICECUBE strings. The DeepCore PMTs have a quantum efficiency that is 40% higher than for the standard ICECUBE PMTs, while the noise-level is on average increased by about 35%. In contrast to the standard ICECUBE strings, DEEPCORE strings have an interstring spacing of 72 m, they are divided into two components: a veto consisting of ten DOMs (10 m vertical spacing) at shallow depths between 1750 m and 1850 m, and the deep detector consisting of 50 DOMs (7 m vertical spacing) installed in the clear ice at depths between 2100 m and 2450 m. The volume in between is not instrumented because it comprises a major dust-layer of poorer optical transparency. The outer ICECUBE detector is used as a veto shield against the background of down-going atmospheric muons.

The physics potential of DEEPCORE includes: the search for galactic point sources of neutrinos, the indirect detection of dark matter and the study of atmospheric neutrino oscillation. The search for point sources of neutrinos is focused on lower energies (≤ 1 TeV) looking for galactic sources. Most of these sources are believed to have a soft energy spectrum. Particularly, supernova remnants older than a few hundred years are thought to have an energy cut-off at a few TeV. A large number of galactic sources are located at the Southern hemisphere, which is not accessible at lower energies with ICECUBE. Therefore DeepCore will extend the field of view of the combined detector.

4.2. Digital Optical Module and Data Acquisition

The DOM [A$^+$09d] constitutes the main detector element of ICECUBE. Each DOM is an independent data acquisition (DAQ) platform that can capture, digitize and time-stamp PMT pulses, calibrate the PMT gain and time, store data internally and transmit them to the surface DAQ. An schematic view of the DOM is presented in Fig. 4.5. Its parts are listed and described below:

- **Glass pressure housing**- A 35.6 cm diameter, 13 mm thick glass sphere made of borosilicate that contains the PMT and electronics boards. It is filled with dry nitrogen at a pressure of 0.5 atm and can resist a pressure up to 400 atm.

- **PMT**- A 25 cm diameter R7081-02 Hamamatsu PMT, which can reach an amplification around 10^7. It is supplied with 2 kV high voltage (HV) from the surface. The PMT discriminator threshold is set to a charge corresponding to 1/4 photo-electrons (pe). ICETOP has a different discriminator threshold.

- **RTV gel**- The PMT is optically coupled to the glass sphere with RTV (Room-Temperature Vulcanizing) optical gel.

- **Mu-metal grid**- It is made of a nickel-iron alloy that has a very high magnetic permeability, thus it shields the PMT against the Earth's magnetic field, increasing the PMT efficiency.

- **LED flasher board**- It contains 12 LEDs used to send light pulses at a wavelength of about 405 nm to other DOMs in order to calibrate the timing, signal amplitude and geometry of the array.

- **DOM mainboard**- It digitizes the pulses (signals) from the PMT, activates the LEDs and communicates with the surface. It includes the analog front-end electronics and two independent types of waveform digitizers: two Analog Transient Waveform Digitizers (ATWDs), which collect 128 samples of 10-bit data over the first 420 ns at 300 MHz each and a fast Analog to Digital Converter (fADC), collecting 256 samples of 10-bit at 40 MHz, which can record longer pulses up to 6.4 μs. In order to minimize the dead-time the ATWDs are used in a ping-pong fashion. The digital electronics are based on a Field-Programmable Gate Array (FPGA) which has a 32-bit CPU, 8 MB of flash storage and 32 MB of RAM.

- **Delay board**- A 11.2 m long stripline that delays the signal to the ATWD by 75 ns. This time interval is necessary to adjust the delay in the trigger logic and to ensure that the leading edge of the PMT waveform is inside the sampling time.

- **HV divider**- It generates the high voltage and distributes the high voltage to the PMT dynodes.

- **Penetrator**- It provides a path where the wires carrying the signals and power to/from the surface can pass through the glass sphere across the boundary. Four DOMs share a quad cable that connects them to the surface.

The data acquisition [A$^+$06a] starts when a PMT signal, from a DOM in the ice, exceeds a threshold (trigger discriminator) set to 0.25 photo-electrons (pe). The trigger is time-stamped by the local clock and both ATWD and fADC collect data. The entire waveform is captured within a time window of $\pm 5\mu$s. An event generated from a Simple Majority Trigger (SMT) is recorded when 8 DOMs are triggered within 5 μs. Data are transmitted to the central counting house located at the surface. The filtering farm applies fast event reconstruction algorithms. The results are used to reduce the data volume and select the physics streams, which are transmitted via satellite to the data center in the North.

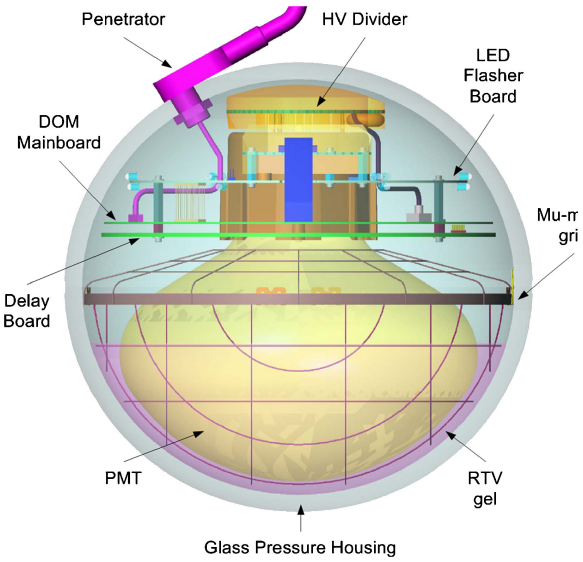

Figure 4.5.: Schematics of a Digital Optical Module. The different components are explained in the text. Source: [A+09d].

4.3. Detector Calibration

4.3.1. Time calibration

The time calibration is achieved by determining the frequency and phase of the DOM's local oscillator relative to a master GPS-controlled oscillator at the surface, using a procedure called Reciprocal Active Pulsing (RAP [S+98]). This calibration is performed recurrently almost every second. On average the time resolution is better than 2 ns.

4.3.2. Gain calibration

DOMCal is a piece of software installed in the DOM that performs several calibrations, converting the DOM digital readout to waveforms in units of voltage and time. Its most important functions are: calibrating the front-end electronics (ATWD gain and sampling frequency, fADC gain and time offset from ATWD), the PMT gain as a function of HV, the discriminator threshold and the signal transit time. This calibration is carried out once a month during special runs.

4.4. Optical properties of ice

In order to understand the light propagation and be able to reconstruct the tracks of the neutrino-induced events, it is necessary to understand the optical properties of the deep glacial ice at the South Pole [A+06b]. Measurements have been done for depths between 1100 and 2350 m. Deeper values have been extrapolated from ice core dust measurements. One of the main characteristics of the ice is the presence of vertical variations (layers) of the concentration of dust impurities, that are consequences of climatological changes. These layers are reflected in the scattering and absorption coefficients.

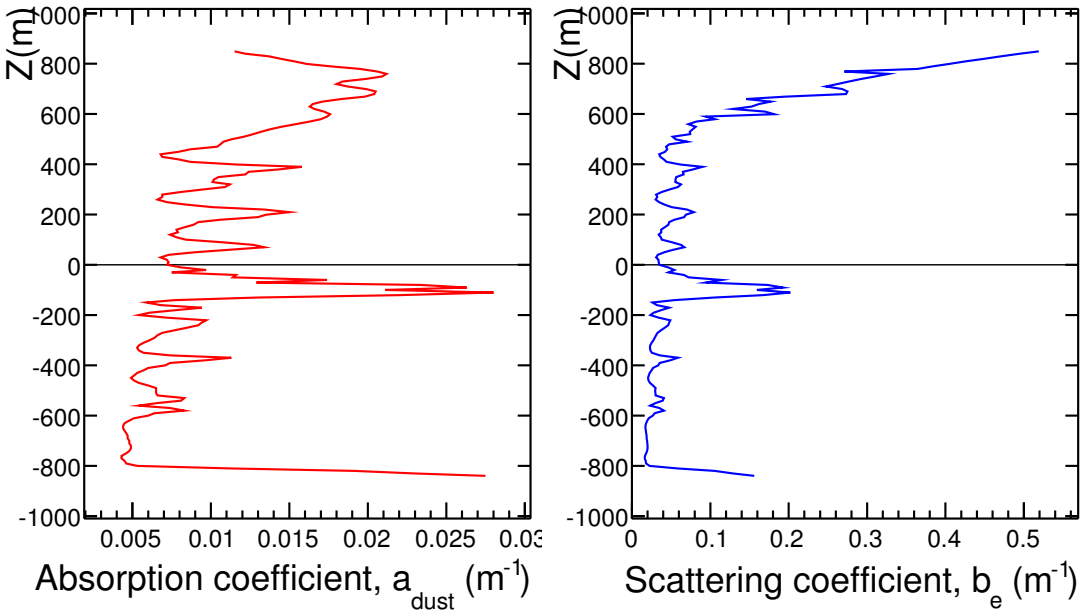

Figure 4.6.: Depth dependence of the effective absorption (left) and scattering (right) of the Antarctic ice at the ICECUBE site at 400 nm wavelength. Data taken from the AHA (Additionally Heterogeneous Absorption) ice model (05-17-2007) [W+07]. The depth, z, is given in detector coordinates, with z=0 corresponding to a depth of 1950 m.

4.4.1. Scattering

In the shallow ice above -1400 m, light scattering can be explained by air bubbles, while below this region it is dominantly caused by the mineral grain component of the dust. For ICECUBE, the light recorded by the PMTs has been usually scattered several times. Therefore photon multiple scattering theory [Kir99] can be applied. It tells us that the average cosine of the light field after n scatterings, $\langle \cos\theta \rangle_n$, can be written in terms of the average cosine of a single scatter, $\langle \cos\theta \rangle$, by $\langle \cos\theta \rangle_n = \langle \cos\theta \rangle^n$.

The average scattering angle for the South Pole ice obtained from simulations using Mie scattering calculations is $\langle \cos\theta \rangle = 0.94$ ($\theta \approx 20^o$), thus the scattering is strongly forward peaked. The scattering mean free path, λ_s, is the average distance between scatters. The effective scattering length, λ_e, defined as the length scale over which randomization occurs, is equal to λ_s for isotropic scattering. For large n it holds:

$$\lambda_e = \frac{\lambda_s}{1 - \langle \cos\theta \rangle} \quad . \tag{4.1}$$

The effective scattering coefficient, b_e, is defined as the reciprocal of the effective length:

$$b_e = \frac{1}{\lambda_e} \quad . \tag{4.2}$$

For ICECUBE $\langle \lambda_e \rangle \approx 25$ m, thus $\langle \lambda_s \rangle \approx 1.5$ m. Depth dependent variations are shown

in Fig. 4.6.

The scattering coefficient depends on the wavelength and can be approximated in the range 300-600 nm by a power law:

$$b_e(\lambda) \propto \lambda^{-0.9} \ . \tag{4.3}$$

4.4.2. Absorption

The path over which the survival probability of a photon traveling inside a medium drops to $1/e$ is called the absorption length, λ_a. Its reciprocal defines the absorption coefficient, also called absorptivity:

$$a = \frac{1}{\lambda_a} \ . \tag{4.4}$$

For ICECUBE $\lambda_a \approx 100$ m. The depth profile of the absorptivity is shown in Fig. 4.6. The absorptivity is also wavelength dependent and can be parametrized. In the wavelength range between 200 to 500 nm the polar ice is extremely transparent and absorption is mainly caused by the presence of insoluble dust impurities (a_{dust}).

The propagation length, λ_p, helps describing the combined effect of scattering and absorption over large distances and is defined in terms of λ_e and λ_a by:

$$\lambda_p = \sqrt{\frac{\lambda_e \lambda_a}{3}} \ . \tag{4.5}$$

For ICECUBE an average value of 29 m is found.

There is yet another characteristic of the ICECUBE environment that affects the optical properties around the DOMs. This concerns the residual air bubbles that are produced during the refreezing process of the drilled string hole. The refrozen ice is usually referred as *hole ice*. These bubbles increment the scattering in the medium, increasing the probability for downgoing light to reach the PMT. Therefore it isotropizes the angular sensitivity of the DOM. This property is difficult to characterize. In the simulation it is quantified by applying a modified angular DOM sensitivity respect to the one measured in the laboratory.

4.5. Neutrino event signatures

Each neutrino-induced event has a particular signature that helps to identify their flavor (electron, muon or tau). In case of a ν_μ charged current interaction the resulting muon produces a track-like trace which is particularly useful for point-like source searches due to its good angular resolution ($\lesssim 1^o$). A fraction of tau neutrinos can also lead to muons by the decay of taus produced in charged current interactions.

A cascade-like signature is produced by neutrino-induced electromagnetic and hadronic particle showers from charged current interactions of ν_e and low energy (below PeV) ν_τ and from neutral current interactions of all neutrino flavors. For a cascade the present angular resolution in ICECUBE is $\sim 30^o$ [M$^+$09b] and in water it can be 10^o or better [Har06]. For ICECUBE this angular resolution is not good enough for standard point-like source searches, though GRB analyses can be done. However, cascades

have a very good energy resolution, since most events are *contained* inside the detector. The number of emitted photons scales linearly with the deposited energy. In the case of hadronic cascades, there are about 20% fewer photons than for electromagnetic cascades.

Tau neutrino events with energies above a few PeV [Seo09] can lead to composite signatures called "double bang", "lollipop" and "inverted lollipop". A *double bang* event, coming from a charged current ν_τ interaction, shows the production of a τ, a cascade, followed by the path of the tau, track-like, ending in the decay of the τ, cascade-like. The *lollipop* and *inverted lollipop* topologies present a part of the *double bang* event, with either the production or decay vertex of the tau lepton outside the detector fiducial volume. Tau neutrino events are almost background-free because the flux of atmospheric ν_τ's either from conventional or prompt origin is nearly zero, thus detecting these signatures would directly confirm the extraterrestrial origin of these neutrinos.

4.6. Triggers, filters and data processing

For the purpose of this thesis ICECUBE data coming from two filters applied to the SMT trigger were used. As mentioned in Sec. 4.2, the SMT requires a minimum number of 8 hit DOMs within a 5 μs coincidence window. Only the hard local coincidence (HLC) readouts are recorded (i.e. a DOM reports only if one of its nearest neighbors is hit). Other triggers not used here include: the ICETOP SMT trigger ($\geq$6 DOMs hit in 5 μs), string trigger ($\geq$5 DOMs hit on a string out of a series of 7 DOMs within 1.5 μs and no hits in the top 3 DOM layers), ULEE (Ultra Low Energy Events), etc.

On top of the SMT trigger several online physics filters [B$^+$07] are applied in order to accommodate the amount of data transferred via satellite to the available bandwidth. The main ICECUBE-only filters during the 2007/08 season, ordered by amount of data transferred [F$^+$07], quoting their rates range, were:

- Muon: 19-24 Hz.
- Cascade: 17.7-22 Hz.
- Moon: 12-18 Hz.
- Low Energy Contained: 4-5 Hz.
- Minimum Bias: 2.5-3.4 Hz, after prescaling (1/200).
- EHE (Extremely High Energy): 1.2-1.8 Hz.

The muon and EHE filters are used in point source searches of neutrinos. The cascade filter is used mostly for diffuse flux and GRB searches. The moon filter is applied in the analysis of the moon shadow, verifying the absolute pointing and the angular resolution of the detector. The *low energy contained* filter looks for low energy muon neutrino generated in the atmosphere or in decays of WIMPS (weakly interacting massive particles) annihilating in the Earth. The minimum bias filter is employed to check filter and trigger performances.

In total 32 GB of filtered data were transferred per day during the 2007/2008 season to the data warehouse in the North using the Tracking and Data Relay Satellite System

(TDRSS) . Once in the North, the data follow a level-by-level processing as summarized below:

- Level 1: Uncompress and unpack raw data, apply calibrations and reproduce reconstructions used at Pole for filtering.
- Level 2: Apply higher level reconstructions that are CPU intensive.
- Level 3: Separate streams relevant for each working group, apply their specific reconstructions and generate ROOT files.

5. Simulation & Reconstruction

Der klassische Friede zwischen der Wirklichkeit und dem Gedanken
war immer schwer zu schließen.
Thomas Mann 1875-1955

5.1. Simulation

Even though in a point source analysis the background is estimated from data alone, it is necessary to simulate and verify the agreement between observations and the predicted background and to estimate the level of purity of the final sample. In this way the understanding of the detector and its response is checked. In case of the high energy neutrino signal, since no direct observation has been made so far, the way to include it in the analysis is by simulation.

The simulation chain [H$^+$06b], explained in detail in the next sections, is summarized here. First the *event generators* create the primary particle with an energy distribution according to a certain model. Then *propagators* transport leptons (e.g. muons) through different media accounting for energy losses and secondaries' production. The Cherenkov light generated by charged particles is tracked by *photon propagators*. When the photons reach the DOMs the *detector response* is calculated.

5.1.1. Event generators

Event generators produce particles by either simulating a reaction or by injecting particles according to a given spectrum. Two types of generators are distinguished , one that produces the main background of atmospheric muons, CORSIKA (COsmic Ray SImulations for KAscade) [H$^+$98], and another one that generates neutrinos, NEUTRINO-GENERATOR/ANIS (All Neutrino Interaction Simulation) [I$^+$07, GK05], that can be applied for background, atmospheric neutrinos or signal simulation (i.e. astrophysical neutrinos).

CORSIKA simulates extensive air showers initiated by high energy cosmic rays, which in turn generate muons that are propagated through the atmosphere. Single and coincident (from two or more independent air-showers) muon events are simulated separately.

NEUTRINO-GENERATOR injects primary neutrinos of any flavor with a certain flux and energy spectrum in the Earth's surface using the physics implemented in ANIS and cross-section parametrization from CTEQ-5 [L$^+$00]. A propagator module transports the neutrinos through the Earth. If they reach a specified volume around the detector, they are forced to interact via charged or neutral currents, creating according to the interaction probabilities either a charged lepton and/or hadrons or a neutrino. All neutrinos are forced to interact in order to make the simulation more efficient, otherwise since their cross section is extremely small, it would be necessary to inject many

more neutrinos. Therefore the values of the interaction probabilities are stored and used later as weights for calculating the real number of expected neutrino events.

Event weighting

The generated neutrinos can be reweighted, for the derived energy spectrum and flux strength, in order to simulate either an atmospheric neutrino spectrum or an astrophysical signal. Usually standard simulations are done for an E^{-1} spectrum so as to maximize the statistics in the high energy region.

The atmospheric spectrum, which is proportional to $E^{-3.7}$ for $E > 1$ TeV [GHS95], follows the conventional neutrino component from the Honda model [H$^+$07] and the prompt neutrino component from the Naumov RQPM (Recombination Quark Parton Model) model [FNV01].

For the extraterrestrial neutrino flux a generic E^{-2} energy spectrum is usually applied. However, harder $E^{-1.5}$ or softer E^{-3} spectra are also used to test higher energy models in the southern sky or less energetic ones in the northern sky.

5.1.2. Particle propagation

The Muon Monte Carlo (MMC) [CR04] propagates leptons through rock and ice. In case of muons, they loose energy due to ionization, bremsstrahlung, photo-nuclear interactions and pair production. Theses energy losses are stochastic, however below an energy threshold they are treated as continuous to speed up the calculation. Cherenkov photons from the muon and secondary showers along its track are estimated.

5.1.3. Photon propagation

The anisotropic Cherenkov photons are tracked inside the heterogeneous detector medium surrounding the light source using PHOTONICS [L$^+$07]. Scattering and absorption depend on the optical properties of the ice (see Sec. 4.4). This is taken into account by using wavelength and position dependent parametrizations. PHOTONICS pre-calculates and stores in tables the photon amplitudes and time distribution at all points in a regularly spaced grid inside the simulated volume. Therefore there is no need for a real-time photon propagation and the values can be read from the table specifying the location of the light sources with respect to the detector.

5.1.4. Detector response

The ICECUBE simulation has several modules that represent the response of the detector. The first step is to generate hits from the photons tracked by PHOTONICS. This is done by HITMAKER for each DOM. Additional random noise hits are injected. A PMT-simulator generates a PMT waveform given a series of all these hits, which have an assigned charge. Saturation, if present, is also handled.

Next the DOM mainboard response is reproduced by DOMSIMULATOR. This means checking the discriminator condition, above which the ATWD recording is started. The DOMLaunches, waveforms from the fADC and ATWD, are filled and the local coincidence requirement is tested.

The last step is carried out by TRIGGER-SIM, a module which applies the trigger logic, accepting or rejecting events. For example, it checks that there is a certain number of DOMLaunches within a given time window (8 hit DOMs within 5 μs, SMT trigger, see Sec. 4.6).

The detector properties can be read from the database and are stored in GCD files (Geometry Calibration and Detector status), used for simulation and reconstruction.

5.2. Reconstruction

Data and simulation constitute a bulk of events holding information on spatial coordinates, times and waveforms recorded by the DOMs. For these values to be useful, the event direction and energy, as well as other track related parameters, must be reconstructed and calculated. In this section, the different reconstruction techniques, later used in the analysis, are described. Since the analysis is focused on point sources of neutrinos, only the muon track-like related reconstruction are described here.

It must be noticed that the reconstructed properties are those of the daughter muon and not directly from the neutrino. However, the space angular difference between the parent neutrino direction and that of the generated muon decreases with energy. This difference is on average[LM00]:

$$\langle \Delta\Psi_{\nu l} \rangle = 0.7^{o} \left(\frac{E_{\nu}}{1\text{TeV}} \right)^{-0.7} . \tag{5.1}$$

Therefore for high energy neutrinos both tracks lay almost in the same line, meaning that the angular resolution of the neutrino will mostly depend on the precision of the reconstructed muon track, rather than on $\langle \Delta\Psi_{\nu l} \rangle$.

5.2.1. Extraction of photoelectrons from digitized waveforms

A common step to all reconstructions is the extraction of a series of Cherenkov photon arrival times and the total charge of the recorded waveforms by the ATWD or fADC. This is done by a module called FEATURE EXTRACTOR [Chi07]. The output of this algorithm is rendered in two forms: a RECOHIT, which only stores the arrival time of a single photon and a RECOPULSE [1], which in addition to the leading edge time includes the total charge and width of a waveform pulse.

Before applying this module, a list of problematic DOMs (around 1%) is removed from the configuration and only HLC (see Sec. 4.6) readouts are taken into account. In order to do the feature extraction the module calculates the baseline in the absence of pulses. The largest pulse (single-peak) above the baseline or a multi-peak extraction can be performed using an iterative Bayesian unfolding [D'A95].

For the subsequent reconstructions only the hits/pulses inside a time window of 6 μs are used.

[1] The pulse is formed by photons that arrive very close in time.

5.2.2. First-guess track reconstruction

A simple semi-accurate initial track reconstruction algorithm is needed for fast background reduction and as a track seed for more advanced reconstructions. The LINE-FIT [A+04] algorithm is used for this purpose.

Line-Fit

This algorithm reconstructs a track using the times t_i of all hits, N_{hit}, in an event, assuming a straight light path, thus not taking into account the geometry of the Cherenkov cone, nor the optical properties of the medium. The light travels with velocity $\vec{v}$ and has a vertex point $\vec{r}$. Then the position of each triggered PMT, $\vec{r}_i$, is given by:

$$\vec{r}_i \approx \vec{r} + \vec{v} \cdot t_i \quad . \tag{5.2}$$

The corresponding χ^2 distribution is defined as:

$$\chi^2 \equiv \sum_{i=1}^{N_{hit}} (\vec{r}_i - \vec{r} - \vec{v} \cdot t_i)^2 \quad . \tag{5.3}$$

It can be analytically minimized differentiating with respect to $\vec{v}$ and $\vec{r}$. The vertex and direction of the track are then easily found. The actual implementation uses the first leading edge time of the hits. No amplitude weight is included and a minimum of 2 hits is required.

5.2.3. Maximum Likelihood track reconstruction

Higher level reconstructions [A+04] apply maximum likelihood statistical methods. The track directions obtained with these time-consuming algorithms are the ones used in the final analysis. A maximum likelihood method estimates a set of unknown parameters a, given a set of measured quantities x by maximizing the likelihood, $\mathcal{L}(x|a)$, defined by:

$$\mathcal{L} = \prod_i p\,(x_i|a) \quad , \tag{5.4}$$

where $p(x_i|a)$ is the probability density function (pdf) of the independently measured x_i values given the set of parameters a. For the present analysis measured photon arrival times (time likelihood) and total charge were used. The full waveform information was not included.

Single-Photo Electron likelihood

The Single-Photo Electron (SPE) time-likelihood is constructed based on the pdfs of single photons arrival times at the positions of the hit DOMs and ignores the pulse charge. It is defined by:

$$\mathcal{L}^{SPE}_{time} = \prod_i^{N_{hits}} p_1\,(t_{res_i}|(\vec{r}_0, t_0, \vec{p}, E_0)) \quad , \tag{5.5}$$

where t_{res} is the residual time (relative arrival time) defined by $t_{res} \equiv t_{hit} - t_{geo}$, the difference between the observed hit time, t_{hit}, and the hit time expected for a *direct photon* (without scattering), t_{geo}. In the actual implementation only the first hit in a DOM is used, because it is less scattered. A parametrization of the photon arrival time distribution, called *Pandel function* [Pan96, JR05], can be used to describe $p_1(t_{res})$ as follows:

$$p_1(t_{res_i}) = \frac{\rho^\xi t_{res_i}^{\xi-1}}{\Gamma(\xi)} e^{-\rho t_{res_i}} \quad , \tag{5.6}$$

where $\Gamma(\xi)$ is the gamma function, $\xi \equiv \frac{R}{\lambda}$ is the distance between emission and detection locations of a Cherenkov photon in units of the mean photon scattering length and $\rho \equiv \frac{1}{\tau} + \frac{c_{med}}{\lambda_a}$, where λ_a is the absorption length (98 m), c_{med} is the speed of light in the medium (ice), τ and λ are free phenomenological parameters determined by photon propagation simulation. One limitation of this parametrization is that it assumes a bulk clear ice without dust layers. As a matter of fact, the absorption length has a range from 37 m, in the dust layer, to 200 m, in the clearest ice (see Fig. 4.6). Therefore, taking an average value (98 m) disregards its depth dependence. However, it still gives a good approximation.

Nevertheless the physical description of the system is incomplete unless the PMT jitter and random noise are included. These effects can produce negative time residuals which the Pandel function cannot handle. Therefore the Pandel function needs to be convoluted with a Gaussian [vE+07], that accounts for the finite time resolution of the detector. The result of this convolution can be approximated in different regions of the distance-time residual space and evaluated numerically in a fast enough way desirable for reconstructing the large amount of filtered events.

The module that performs the track reconstruction, named *gulliver*, uses as a first seed the output from LINE-FIT. According to the chosen options an iterative fitting procedure is carried out. The module uses a minimizer algorithm to find the global minimum of the negative logarithm of the likelihood (LLH) function. The subsequent track hypothesis in further iterations are taken from randomized directions within a certain zenith range or inside a half-sphere parametrization.

Multi-Photo-Electron likelihood

An improvement with respect to the SPE reconstruction, which refines the angular resolution specially for higher energies, is the Multi-Photo-Electron (MPE) likelihood. It uses the arrival time of the first of a total of N photons (less scattered one), thus including information on the total charge, given by the total number of recorded photons. The corresponding likelihood is defined by:

$$\mathcal{L}_{time}^{MPE} = \prod_{i}^{DOMs} p_N^1(t_{res_i}) = \prod_{i}^{N_{hits}} \left(N \cdot p_1(t_{res}) \cdot \left(\int_{t_{res}}^{\infty} p_1(t) dt \right)^{(N-1)} \right) \quad , \tag{5.7}$$

where p_1 is the cumulative distribution of the single photon pdf.

Bayesian likelihood

The Bayesian likelihood [Hil01], also called zenith weighted likelihood, adds to the above mentioned likelihoods extra knowledge of the probabilities of the atmospheric

background muon hypothesis making use of Baye's Theorem. The original likelihood is weighted by a prior probability that describes the direction distribution (i.e. zenith distribution) of the background particles. Therefore the Bayesian likelihood is written as:

$$\mathcal{L}_{Baye} = \mathcal{L}_{time} \cdot P(\theta) \ , \tag{5.8}$$

This result comes from Baye's theorem, which states that for two hypothesis, a (inferred muon track parameters) and x (observed hits), the probability of a given x is described by:

$$P(a|x) = \frac{P(x|a)P(a)}{P(x)} \ , \tag{5.9}$$

where $P(x|a) = \mathcal{L}_{time}$, and both $P(a)$ and $P(x)$ are the priors. $P(x)$ as a normalization constant is not necessary for the likelihood, because the likelihood is defined up to an arbitrary constant.

In Eq. 5.8, the prior $P(\theta)$ is a polynomial fit to the zenith distribution of down-going atmospheric muons, thus the tracks are forced to be reconstructed as down-going.

The ratio of the likelihoods (see Sec. 7.3.2 for more details) can be used to reject misreconstructed atmospheric muon background. Lower values of the ratio indicate that an event is most likely down-going.

5.2.4. Angular uncertainty estimation

Once a track is reconstructed, it is important to estimate the accuracy (space angle separation between the reconstructed and true direction) of the obtained direction. This estimate can be used as a cutting parameter to reject wrongly reconstructed events and also as a parameter in the analysis method. A semi-analytic method [Neu06] that estimates the angular resolution of tracks reconstructed with a likelihood algorithm is used. This method fits the negative log likelihood space around the minimum of the reconstructed track and does not depend on simulation. The confidence ellipse is defined in the parameter space of $-\log(\mathcal{L})$ (the negative of the logarithm of the likelihood). The size of the error ellipse is determined when the parameter $(-\log(\mathcal{L}))$ changes by $1/2$ its minimum value. This method is usually called *paraboloid*.

5.2.5. Energy estimation

A likelihood algorithm for reconstructing the event direction can also include an energy proxy (photon density). Then all track parameters are found together during minimization. However, the procedure can be divided by first finding the track with a standard likelihood without energy proxy and then directly using the resulting track to calculate the energy proxy without minimization. This last step is done by a module called *mue* [ZC07, Chi08]. The output of this estimator is given as photon density (i.e. photons per unit length per PMT effective area).

The total expected number of photons, μ, arriving at each OM can be approximated by $\mu = N_l \cdot \mu_0(d)$, where N_l is the reconstructed photon density and $\mu_o(d)$ is the average number of photons emitted per unit length, which depends on the distance from the track. This quantity can be constructed combining two approximations, one that accounts for the Cherenkov photons (in a cone around the track) emitted in the immediate vicinity of the track, so that they are unscattered, and a second component that

describes the photons coming far from the track with a diffuse approximation.

Above a certain energy threshold ($\approx$ 1 TeV) the muon energy loss is then dominated by stochastic processes. The muon and its secondaries produce a number of Cherenkov photons per unit length that is proportional to the muon energy. Thus the N_l can be computed as a function of the muon energy.

This reconstruction achieves in the energy range of $10^{4.4}$ to $10^{7.4}$ GeV an energy resolution of 30% in $\log_{10}(E[GeV])$.

5.2.6. Double muon reconstruction

Given the presence of coincident (e.g. double) down-going atmospheric muon events that can mimic, for a single fit, an upgoing neutrino, it is necessary to introduce track reconstructions that address this problem. This is done in the module called *double-muon* [B$^+$09b]. Two simple approaches, where the pulses are split into two parts and reconstructed separately, are described here:

- **Time splitting**.- The pulses are divided into two sets depending on when they happen with respect to the average time of the pulses.
- **Geometrical splitting**.- The pulses are separated by a plane defined to be perpendicular to the single-muon-fit-track and that contains the center of gravity of the pulses.

Each subset of pulses is reconstructed with a normal single-muon fit, either LINEFIT or a likelihood fit. Thus it becomes a 2x5 parameter fit. For a single signal upgoing neutrino event both sub-event fits should also be reconstructed as up-going. However, in the case of coincident muons it is expected that least one fit points downwards.

5.2.7. Online reconstruction & selection

The advanced reconstructions and cut selection are usually done in the North, which means a delayed offline processing. Nevertheless, with more analysis experience, it should be possible to apply more efficient filters and more reconstructions at the South Pole obtaining an online neutrino sample. In this direction a first attempt to create an *Online Level2 filter* [BA$^+$08b] was carried out during this work. The aim of this work was focused on the Neutrino triggered Target of Opportunity (NToO) programs, which require a fast alert system to trigger optical and gamma-ray telescopes. This filter was created for IC40 (2008/09) providing a reduced rate of the order of 2 Hz. The events were later reconstructed with more CPU intensive algorithms, providing a higher signal-to-background rejection power. The output of this filter should provide a generic sample that can be used for different applications.

The Level2 filtering scheme is applied to the output of the Muon Filter. The cuts are simple and stable and include the following variables: zenith angle of LineFit (θ_{LF}) and LLH fits (θ_{LLH}), the number of direct hits (NDirC) and the reduced loglikelihood (RLogL) (see Sec. 7.3 for the description of these parameters). The numerical values of the cuts and the corresponding passing rates for IC40 are shown in Table 5.1.

For upgoing ($\theta_{true} > 80^o$) well reconstructed events, defined as having an angular mis-match of less than 3^o, the online Level2 filter is 97(94)% efficient for an $E^{-2}(E^{-3})$

[1] By using *or* instead of *and* the signal efficiency at very low and high energies is improved.

Cut	Corsika	Corsika coin.	E^{-2}	E^{-3}
Muon Filter	21.5(100)	8.2(100)	(100)	(100)
$\theta_{LLH(1\&2)} \geq 80^o$	6.8(31)	6.5(79)	(85.9)	(88.8)
$\theta_{LF} \geq 70^o$	5.6(26)	5.5(67)	(83.1)	(85.8)
NDirC ≥ 5 or [1] RLogL ≤ 10	1.1(4.9)	1.2(14)	(77.2)	(72.8)

Table 5.1.: Passing rates in Hz for consecutive application of cuts used in the online Level2 filter for IC40. The values in parenthesis represent the percentage (%) of events passing the cuts with respect to the Muon filter.

spectrum. The efficiency is relative constant in zenith as well as in energy. The events that pass this filter are reconstructed again using a 10-fold LLH fit, a Bayesian fit and their paraboloid angular error estimate is calculated.

6. Analysis methods

Manche Seele wird man nie entdecken,
es sei denn, dass man sie zuerst erfindet.
Friedrich Nietzsche 1844-1900
Also sprach Zarathustra

Astrophysical neutrinos can be searched for in several ways. This work focuses on extraterrestrial point sources of neutrinos. The possible source candidates have been described in Sec. 2.2. In order to give a broader view of the available analysis methods, other related neutrino searches, not carried out in this work, are briefly discussed and compared to the point source search. These analyses include the search for neutrinos associated with GRBs and the search for diffuse neutrino fluxes.

A neutrino point source search looks for events coming from a restricted angular region, which could be identified with a known astrophysical object. Transient objects, such as GRBs, deserve a particular analysis given that they last for a very short time. A GRB analysis is similar to the time variable search presented here (see Sec. 6.3), to the extend that both are looking for spatial and temporal coincidences. Nevertheless, a specialized GRB search focuses only on short time windows around the observed GRBs, which have time-scales much shorter than the flares from sources studied here. However, in principle the untriggered flare search presented here is also capable of finding a GRB-like signal, since there is no lower threshold on the duration of a flare, though it is not the aim of the analysis.

The most promising astrophysical sources listed in Sec. 2.2 can be analyzed looking for a neutrino signal. If no evidence for a point source is found from these locations, every direction in the sky can be searched for. These two point sources searches are covered in this work. If the neutrino fluxes from point sources are too weak, a stacking of several known sources can be done, trying to enhance the discovery chance. In such an analysis, the contributions from each source are added up. An alternative method is to enlarge the angular window from a point-like object to a extended region of the sky.

If the sources are still too weak to be observed, then adding up the extraterrestrial neutrinos contribution from all directions in the sky would increase the chances of discovery. This is done in a diffuse flux search, where unresolved sources distributed over the sky are combined to produce an observable signal. A point source search and a diffuse flux search have different ways to deal with background. For point sources the background can be estimated directly from data. However, in case of a diffuse search, where no off-source region is available, the prediction of the expected background comes from simulation, making it more challenging to understand the background. The background estimation relies on theoretical predictions of atmospheric neutrino fluxes, which are less certain, especially for atmospheric prompt neutrinos. In a diffuse search, the difference in the energy spectrum between signal astrophysical neutrinos and background atmospheric neutrinos, plus other contamination, plays a

key role. A diffuse signal would manifest itself as an excess of events at higher energies, since the atmospheric neutrino spectrum ($E^{-3.7}$) is softer than for the predicted astrophysical one (E^{-2}).

Two types of point source searches are investigated here: a time integrated one and a time variable one, which perform better for steady and flaring sources respectively. In each case two methods are presented: a binned and an unbinned maximum likelihood method. The latter one is found to have a better performance in the resulting sensitivity and discovery potential. A comparison of both methods is also discussed in this chapter.

6.1. Point source search concept

Finding neutrino point sources in the sky means to locate an excess of events from a particular direction over the background. These events might present additional features that distinguish them from background, for example a different energy spectrum or time structure.

Neutrinos travel from their source to Earth without being deflected by magnetic fields, since they have no charge, and can therefore point back to their sources. Muon neutrinos after a charged current interaction produce muons. In addition tau neutrinos can give rise to muons, if they interact via charged current, producing a tau, which then decays in 17.4% of the cases into muon and two neutrinos. These muons, for enough high energies, follow the same direction of the parent neutrino. Therefore the reconstruction direction of the muon track points to the astrophysical source.

If the background is uniform, the clustering of the signal events around the source location may become significant, if the strength of the signal is high enough. It would be an easy task to spot a point source in a skymap, if the background would be low or if the neutrino flux would be high enough. However, none of the last premises is real. There is an overwhelming background of atmospheric muons that needs to be removed, after which the atmospheric neutrino background becomes considerable. The atmospheric neutrino background can be regarded as relative uniform inside a small declination band. Assuming the recorded data have a negligible signal contribution, the background and its properties can be estimated from them.

The question remains how to disentangle signal events from background. Counting events around a possible source location (inside a circle with a radius proportional to the error of the reconstruction) and comparing this number to the estimated background using binomial statistics is the solution given by the binned method. This can be partially improved by using the information on the error estimate of the reconstruction in an unbinned method. Then events outside a standard bin search radius, might also contribute to the signal, if their angular error is large.

Furthermore, the energy spectrum of the standard signal and background atmospheric neutrinos is different, thus the energy estimate of each event can be included to further separate signal from background. The time information is another property of the events that can be used. If the sources are flaring, reducing the observation period around a possible flare increases the signal to background ratio.

6.2. Time integrated search

A time integrated search uses year-long data, adding up in time possible contributions from sources. Such a search is more sensitive to steady sources, though it is also applied to variable sources. In the context of this thesis a binned method, described in this section, was applied to ICECUBE data. In addition, an unbinned method is presented for comparison purposes and due to the fact that it is later used for the variable sources search.

6.2.1. Binned method

The binned method [A$^+$07a] distinguishes a localized excess of signal events (coming from an extraterrestrial neutrino point source) from a uniform background ($\nu_{\mu_{atm}}$ and misreconstructed μ_{atm}) using a circular angular search bin. It is assumed, as well as in the unbinned method, that the signal neutrino contribution in a given declination band is negligible, therefore the mean number of background events can be estimated directly from data. The flux sensitivity, Φ^{sen}, in a given declination band, is calculated by comparing the number of simulated signal events reconstructed inside the search bin, n_{sig}, to the average number of background events from data, using:

$$\Phi^{sen} = \Phi_0 \frac{\left\langle \mu_{90}^{FC}(n_{bg}) \right\rangle}{n_{sig}} \ , \tag{6.1}$$

where Φ_0 is the initial signal flux that yields n_{sig} events, $\left\langle \mu_{90}^{FC}(n_{bg}) \right\rangle$, represents the average event upper limit (90% C.L.), in the Feldman & Cousins (FC) approach [FC98], for the expected background in the bin, n_{bg}, and no true signal. In other words, the signal flux has to be scaled by $\left\langle \mu_{90}^{FC}(n_{bg}) \right\rangle / n_{sig}$ in order to be excluded at 90% confidence level. A sensitivity can be obtained for each signal model, i.e. different energy slopes assumed in the power law spectrum (e.g. E^{-2}).

The sky is divided into declination bands. The bands are selected in $\sin(\delta)$ steps in order to have a uniform solid angle coverage and are overlapping [Ack06]. The number of background events in the search bin is estimated from the declination band by:

$$n_{bg} = n_{bg}^{\delta} \frac{A_{bin}}{A_{\delta}} \ , \tag{6.2}$$

where n_{bg}^{δ} is the number of background events inside the declination band, A_{δ} and A_{bin} are the solid angle of the declination band and bin respectively, they are defined as:

$$A_{\delta} = 2\pi \left[\sin(\delta + R_{bin}) - \sin(\delta - R_{bin}) \right] - A_{bin} \ , \tag{6.3}$$

$$A_{bin} = 2\pi \left[1 - \cos(R_{bin}) \right] \ , \tag{6.4}$$

where R_{bin} is the radius of the bin. The solid angle ratio $\frac{A_{bin}}{A_{\delta}}$ scales the events in the band to the search bin.

The number of signal events are those counted inside the bin radius. However, since a point-like signal simulation was not available, only a diffuse flux simulation, a different approach was used to emulate a point-like simulation. Therefore the number of

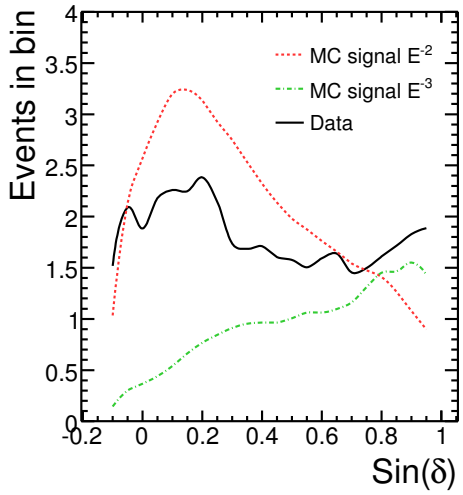

Figure 6.1.: Number of events per bin in IC22, for a signal input flux of 10^{-11}TeVcm^{-2}s^{-1} (E^{-2}) and 10^{-4}TeVcm^{-2}s^{-1} (E^{-3}).

signal events from a point-like source using a diffuse flux simulation is approximated by:

$$n_{sig} = n^{\delta}_{sig}(\Delta\Psi < R_{bin})\,\frac{1}{A_{\delta}}\ , \tag{6.5}$$

where n^{δ}_{sig} is the number of signal events inside the declination band, $\Delta\Psi$ is the space angular difference between the true and reconstructed track.

The p-value of a certain observation for a particular direction is calculated using binomial statistics by:

$$\text{p-value} = \sum_{k=n_{obs}}^{\infty} \binom{n^{\delta}_{bg}}{k} p^k (1-p)^{n^{\delta}_{bg}-k}\ , \tag{6.6}$$

where n_{obs} is the number of observed events inside the angular search bin, n^{δ}_{bg} was already defined as the number of events inside the declination band, and the probability p is the ratio between the area of the search bin (A_{bin}) and the area of the declination band (A_{δ}).

If after analyzing the real data no signal is found, the corresponding flux upper limit is calculated by:

$$\Phi^{lim} = \Phi_0 \frac{\mu^{FC}_{90}(n_{bg}, n_{obs})}{n_{sig}}\ , \tag{6.7}$$

where n_{obs} is the number of observed events inside the search bin and $\mu^{FC}_{90}(n_{bg}, n_{obs})$ is the FC event upper limit for n_{bg} expected background events and n_{obs} observed events.

The binned method is applied to IC22 data to both a catalog of pre-defined sources and the whole Northern sky. In the latter case, a net of overlapping bins is applied in order to maximize the discovery potential, thus the search bin is more likely centered around any possible source location. This approach does not increase much the number of trials, given the large level of correlations between the neighboring bins. For a detailed study of this effect see [Hau04]. The chosen system of bins for this analysis is

the same as the one adopted in [A$^+$07a].

The overall effect of trials and bin correlations is taken into account by MC simulation, in which randomized (i.e. azimuth shuffled events) sky maps from data are generated and scanned using the same grid. Shuffling the events' azimuth or right ascension, while keeping the other events' properties, simulates a random experiment. This randomization is justified since a uniform distribution of atmospheric neutrinos, atmospheric muons and cosmic rays is expected.

The number of events in a bin (radius as given in Eq. 7.5) used in the binned method is shown declination-wise in Fig. 6.1 for IC22 data and two possible neutrino energy spectra. The mean value for background is 1.8 events, while for a E^{-2} neutrino signal with flux 10^{-8}GeVcm^{-2}s^{-1} the mean value is 2.1 events. The zenith structure is modulated by the interaction and absorption of neutrinos in the Earth and the effect of the event selection.

Sensitivity and discovery potential

The power of the method can be evaluated and compared to other methods calculating the neutrino flux sensitivity and discovery potential (minimum signal flux needed for a 5σ detection with 50% probability). In Fig. 6.2 the results are presented for the Northern sky with IC22 data assuming two energy spectral indexes, the canonical E^{-2} and a softer spectra with E^{-3}. The sensitivities and discovery potentials are compared for two different event selections (sets of cuts): mathematical best cuts optimized with respect to sensitivity, chosen independently for each spectrum (cuts shown in Fig. 7.4) and a simplified version of the latter cuts (selected for the analysis and described in Sec. 7.4). The simplified cuts are chosen as a compromise between the two spectra.

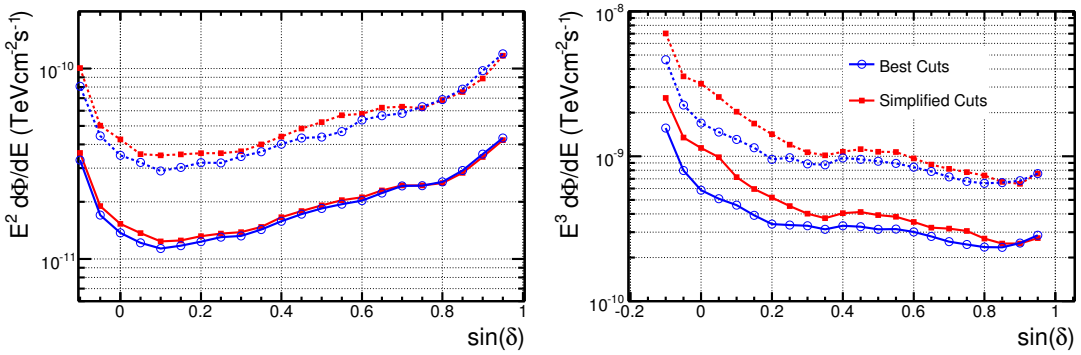

(a) E^{-2} signal (b) E^{-3} signal

Figure 6.2.: Sensitivity (solid lines) and discovery potential (dashed lines) to point sources from the binned method with different neutrino energy spectra as function of declination for different sets of cuts, using IC22 data. The best cuts are different for E^{-2} and E^{-3}. They are the optimal in each spectrum.

6.2.2. Unbinned maximum likelihood method

The unbinned method [Neu03, B$^+$08] exceeds the binned method by including additional information from the events, such as the angular uncertainty and the energy and

makes use of a maximization procedure. The likelihood of the data having $\hat{n}_s$ signal events and $\hat{\gamma}_s$ source spectral index, is given by the product of the probability density of all events, n_{tot}:

$$\mathcal{L} = \prod_{i=1}^{n_{tot}} \left(\frac{n_s}{n_{tot}} S_i + \left(1 - \frac{n_s}{n_{tot}} \right) B_i \right) \quad , \tag{6.8}$$

where S_i and B_i are the signal and background probability distribution functions. The space parameter of the likelihood is scanned and its maximum is found, in fact the minimum of $-\log(\mathcal{L})$ is calculated.

A restriction to a sub-set of events from a smaller region around the source location is used to speed up the calculation. This region should be chosen such that it is larger than the event's angular resolution. Events far from the source hardly contribute to the signal term and can be disregarded. A zenith band of 6° is used for convenience.

In order to calculate the significance of the likelihood, a likelihood ratio test statistic, λ, is defined:

$$\lambda = -2 \log \left[\frac{\mathcal{L}(\vec{x}_s, n_s = 0)}{\mathcal{L}(\vec{x}_s, \hat{n}_s, \hat{\gamma}_s)} \right] \quad , \tag{6.9}$$

where $\hat{n}_s$ and $\hat{\gamma}_s$ are the best estimates of the number of signal events[1] and source spectral index, respectively, which are found by maximizing the likelihood, ($\mathcal{L}$). The location of the source is represented by $\vec{x}_s$. The null hypothesis corresponds to $\mathcal{L}(n_s = 0)$.

The final goal is to obtain a confidence level for the rejection of the null hypothesis. For this purpose, a distribution of λ for the null hypothesis is created using scrambled dataset simulations where the signal is considered to be negligible. The p-value of a given λ is the fraction of the null-hypothesis-distribution above λ.

Background term

The background probability density function (pdf), B_i, calculated purely from data distributions, is given by:

$$B_i = P_i^{space}(\theta_i, \phi_i) P_i^{energy}(E_i, \theta_i) \quad , \tag{6.10}$$

where P_i^{space} describes the distribution of events in a given area and P_i^{energy} is the energy probability determined from data distributions. In a simple case, the P^{space} probability would be uniform because of random distribution of background events. However, due to the applied cuts, Earth absorption properties and detector geometry, this probability is dependent on zenith [2], θ_i, and azimuth, ϕ_i. The irregular azimuthal distribution caused by the detector geometry is shown as a function of zenith in Fig. 6.3. For time integrated analyses covering one year the dependence on the azimuth is negligible because the exposure for all right ascension directions is integrated. P^{space} has value unity when integrated over solid angle inside the test region (i.e. zenith band).

The energy probability, P_i^{energy}, is determined from the energy distribution of data and depends on the zenith coordinate. Instead of the real energy, an energy proxy is

[1] The number of signal events is restricted to be positive, not allowing for negative fluctuations. Therefore the test statistics has always a positve value. Having a negative number of signal events would mean to fit an energy spectral index to non-existent events.

[2] In the IceCube coordinate system, the zenith is defined to be zero for particles coming directly from the South, while particles from the North have $\theta = 180°$.

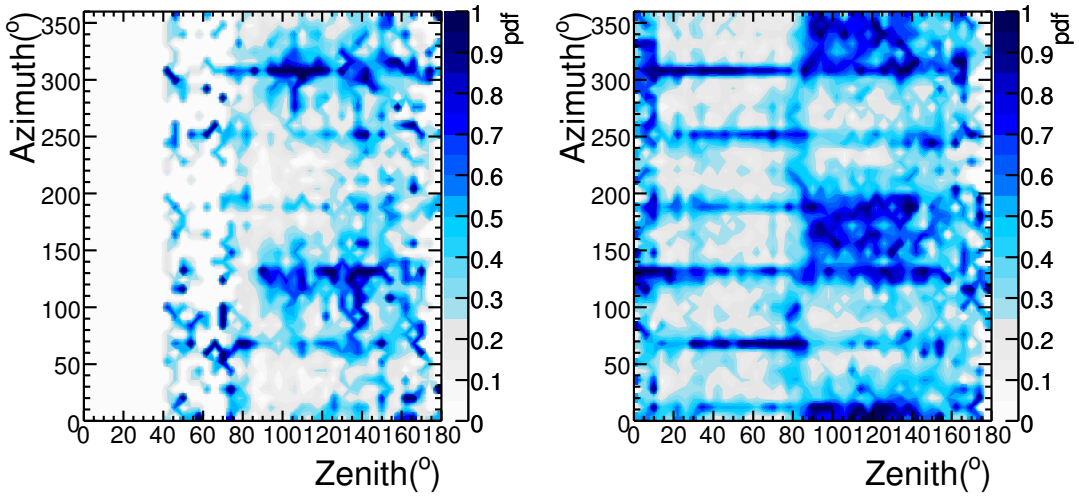

(a) IceCube 22 (b) IceCube 40

Figure 6.3.: Azimuth and zenith distribution of data normalized for each zenith band. For IC22 there are no events below $\theta = 40^o$ because the event sample did not cover the entire Southern sky.

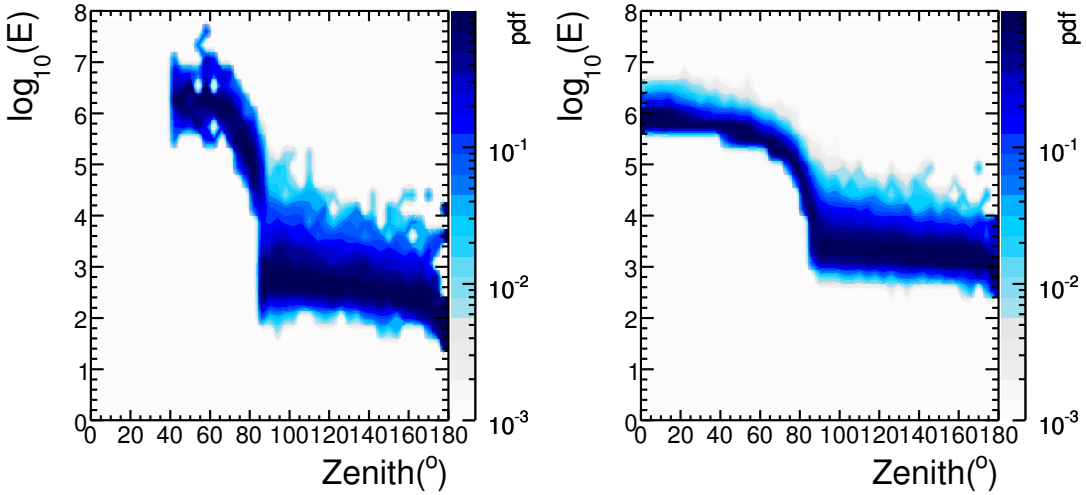

(a) IceCube 22 (b) IceCube 40

Figure 6.4.: Background pdf of reconstructed energy estimator from data as a function of zenith angle. The Southern sky corresponds to zenith<90.

used. The energy reconstruction applied (see Sec. 5.2.5) gives the number of photons per track length.

In the Southern sky an energy sensitive event selection is the most efficient way to reduce the atmospheric muon background [Lau10]. This energy cut decreases for larger zenith angles, thus creating a zenith dependence of the energy. Therefore a zenith dependent energy probability, shown in Fig. 6.4, is needed. Note that for the Northern sky the energy dependence on zenith is small.

The region around the horizon between 75° - 90° is special, because it contains the transition between higher to lower energies, going from the Southern to the Northern sky, due to the selection cuts. In this transition region, the background energy distribution greatly overlaps with the signal energy range for an E^{-2} spectrum (see Fig. 6.6), thus decreasing the enhancement obtained by including an energy term in the likelihood.

Signal term

The signal pdf, S_i, is given by:

$$S_i = P_i^{space}(\mid \vec{x}_i - \vec{x}_s \mid, \sigma_i) P_i^{energy}(E_i, \theta_i, \gamma_s) \ , \tag{6.11}$$

where the spatial probability, P_i^{space} is a Gaussian function of $\mid \vec{x}_i - \vec{x}_s \mid$, the space angular difference between the source location, $\vec{x}_s$, and each event's reconstructed direction, $\vec{x}_i$, and σ_i the angular error of the reconstructed track. The 2-D Gaussian function used to model the angular uncertainty is given by:

$$P_i^{space}(\mid \vec{x}_i - \vec{x}_s \mid, \sigma_i) = \frac{1}{2\pi\sigma_i^2} \exp^{-\frac{|\vec{x}_i - \vec{x}_s|^2}{2\sigma_i^2}} \ . \tag{6.12}$$

The estimator used for σ_i, paraboloid sigma (see Sec. 7.3.2), is the size of the error ellipse, in the log likelihood space, around the minimum of the reconstructed track.

The energy probability, P_i^{energy}, constructed from signal simulation, is a function of the event energy estimation, E_i, the zenith coordinate, θ_i, and the assumed energy spectral index of the source, γ_s ($E^{-\gamma_s}$). A projection of P_i^{energy} for the whole sky is shown in Fig. 6.5 and for different zenith bands in Fig. 6.6. For a given θ_i and γ_s the energy pdf is normalized to unity over E_i.

6.3. Time dependent Search

If the sources of extragalactic neutrinos are flaring, like their gamma-ray counterparts, their detection probability is enhanced by a time dependent search over the aforementioned time-integrated search. For example, blazars, among all Active Galactic Nuclei (AGNs), show the most extreme photon flux variability at all wavelengths. The variability time-scale ranges from fast flares of few minutes, to hours and high states of several days. In hadronic models of AGNs [Aha00, BMB09], these flares arise from photo-hadronic interactions, which also lead to the coincident production of neutrinos.

Time integrated analyses looking for these astrophysical neutrinos are less sensitive in this flaring scenario because they contain a higher background of atmospheric neu-

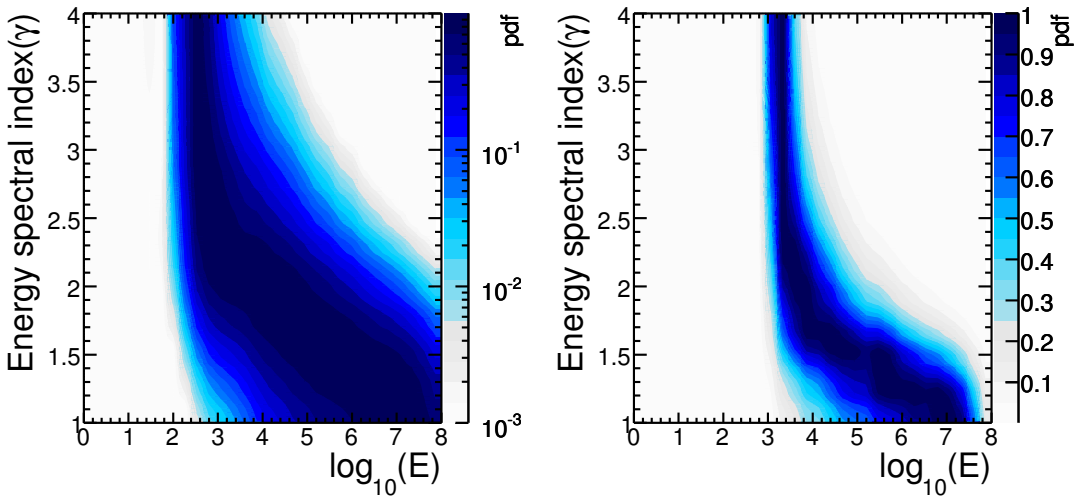

(a) IceCube 22 (b) IceCube 40

Figure 6.5.: Projection for the whole sky of the energy component of the signal pdf as a function of the energy estimator and energy spectral index.

trinos and atmospheric muons. Therefore a time dependent analysis is expected to be more sensitive since it reduces the background by searching smaller time windows around the flare.

Transient sources, like Gamma-Ray Bursts (GRBs), are also candidates of photon-correlated astrophysical neutrinos. Their shorter duration, in the order of seconds, makes their search almost background free. These objects require in principle a similar time dependent analysis. However, due to the different modelling of the sources and their precise occurrence in time, they are analyzed separately in [A$^+$10a]. However, it is still possible that a GRB falls within one of the directions tested in the present analysis. Therefore, the directions of GRBs bursting during the data taking periods of the analyzed data (IC22, IC40) were compared to the selected sources of the present analysis. For IC22 there were no coincidences, while for IC40 there was only one overlapping source within 1 degree radius. Nevertheless, the results coming from a specialized GRB analysis constrain much more the flux upper limit.

There are two approaches to neutrino time dependent searches:

- **Triggered Flare Search**: Looking directly for photon-neutrino correlations from AGNs using specific sources lightcurves from Multi-WaveLength (MWL) observations (for IceCube 22-string results see [B$^+$09a]).
- **Untriggered Flare Search**: A generalized search for neutrino flares, motivated but not associated with MWL observations, because these are scarce and not available for all sources during complete periods. In addition, there could be a time lag between observed photon flares and the associated neutrino flares.

In the context of this thesis the second approach was chosen. An untriggered unbinned flare search was developed and applied to IC22 and IC40 data, using a compact list of pre-defined source directions. A time-clustering algorithm (see [S$^+$07, BA$^+$09]), that finds the most significant flare in a long period, is the basis of the analysis. The

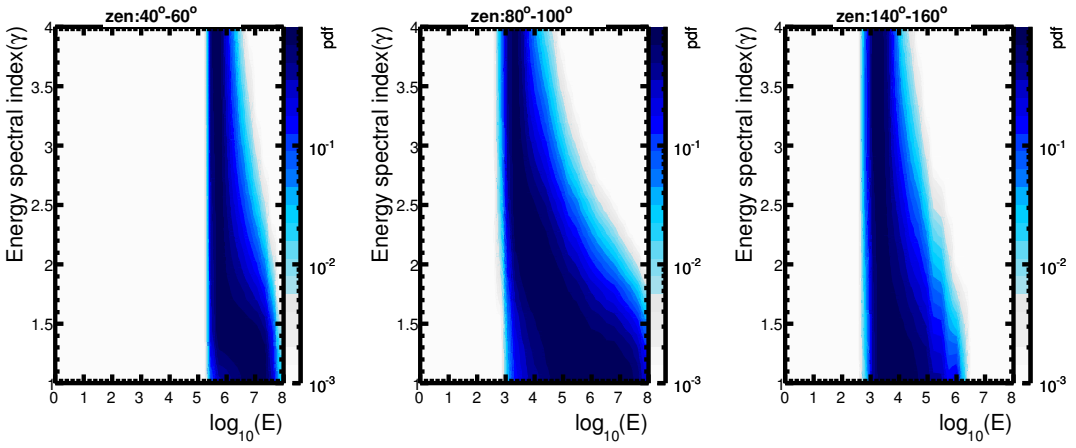

Figure 6.6.: Energy component of the signal pdf as a function of the energy estimator and energy spectral index for different zenith bands using IC40 neutrino signal simulation.

algorithm tests the most promising time-windows, which are fixed from the neutrino data event times themselves. The selected times correspond to the events that have more signal-like properties (e.g. reconstructed direction closer to the candidate source, high energy). In the case of a binned method, those events inside the search bin are used and in the unbinned method those with $S_i/B_i > 1$. Each combination of these event times assigns a starting and ending time, that define the flare search windows Δt_i.

Even though the number of trials coming from all combinations of event times is increased, reducing the significance, for flares sufficiently shorter than the total observation period, the time clustering algorithm is more sensitive than a time integrated analysis. For a flare of width around 100 days [B$^+$10a] a time integrated analysis starts to deliver a higher discovery probability than a time dependent search (see Fig. 6.10a for a detailed comparison). Since the predicted time scales (less than 30 days, [G$^+$08, P$^+$09]) are well below this threshold (i.e. $\sim$ 100 days), the method is well-motivated.

The data were analyzed with an unbinned method. However, for completeness also the binned method, which is less sensitive, is briefly summarized.

6.3.1. Binned method

In the binned method [S$^+$07], a circular angular search bin (e.g. 2.5° and 1.5° radius, for IC22 and IC40, respectively) around the source direction is used. The times of the events that define the search time windows (Δt_i) are given by all the events inside this bin. In [S$^+$07] a variable bin size that optimized the discovery potential was used. However, in this work a simple fixed bin size is applied, since the focus was given to the unbinned method, which does not depend on a search bin.

The significance parameter is obtained from Poisson statistics, given the number of expected background events inside the bin and the observed events in each cluster with multiplicity m. The integral of the Poisson distribution of the background events starts at $(m-1)$ since the beginning and end of the time period are fixed from the data themselves.

Background modeling

The number of expected background events inside a bin around the source location is estimated from a declination band with the size of the bin. For each individual cluster being tested this value is equal to:

$$N_{bg}^{bin} = \int_{t_{start}}^{t_{end}} Rate_{bg}^{bin}(t)\ Uptime(t_{start}, t_{end})\ Azi_{corr}(\phi_{start}, \phi_{end}, \Delta t)\ dt\ , \tag{6.13}$$

where the background rate in a bin, $Rate_{bg}^{bin}$ is integrated in the given time window, Δt, defined by t_{start} and t_{end}. This value has two corrections, one coming from the detector uptime (see Sec. 7.1.2) fraction, $Uptime(t_{start}, t_{end})$, and one from the azimuth correction, $Azi_{corr}(\phi_{start}, \phi_{end}, \Delta t)$, which will depend on Δt. A correction for the azimuth direction is needed since the detector does not have a symmetrical geometry. There are some preferred directions with higher acceptance (see Fig. 7.16). If $\Delta t \gg$ 1day, the azimuth correction is not significant, given that all azimuth directions are covered, averaging the acceptance.

Assuming that the event rate does not depend on declination, the rate in a declination band around the source is obtained from the corresponding rate fraction in the whole hemisphere. This is done in order to reduce the error due to statistical fluctuations. In this way, the rate is more robust compared to calculating it only with events from the declination band.

The event rate, $Rate_{sky}(t)$, depends in general on time. For a given bin it is obtained by:

$$Rate_{bg}^{bin} = Rate_{sky}(t)\ \frac{N_\delta}{N_{sky}}\ \frac{A_{bin}}{A_\delta}\ , \tag{6.14}$$

where $Rate_{sky}(t)$ is the event rate for either the Northern or Southern skies, N_δ is the number of events in the given declination band, N_{sky} is the number of events in the corresponding hemisphere, A_{bin} and A_δ are the areas of the bin and declination band, respectively.

The final data sample in the Northern sky consists mostly of atmospheric neutrinos which do not show a significant seasonal variation (<1%), therefore the rate is usually constant. On the other hand, the Southern sky retains mainly high energy atmospheric muons with larger seasonal variations ($\pm$6%). In order to give an accurate estimate of the rates, a fit is used. Two behaviors are assumed: a steady rate (constant) and a periodical varying rate (sinusoidal) for the whole year. The Northern and Southern skies are fitted separately. In Fig. 6.7 the rates corrected for uptime[3] are plotted for the whole data-taking period of IC22 and IC40 together with their fits. In both cases the best fit for the Northern sky was a constant and for the Southern sky a sinusoidal fit. The fits parameters and errors are summarized in Table 6.1. It has been verified that the time modulations for different zenith bands within a half hemisphere are the same, thus it is valid to use all events inside the half hemisphere to fit the rates.

6.3.2. Unbinned maximum likelihood method

In order to extend the unbinned method to time-variable sources [BA$^+$09, B$^+$10b], a time term needs to be included in the likelihood description. In general, the mean time

[3]The uptime takes into account the inefficiency periods and data gaps after data quality selection.

FIT	Param	SOUTH	NORTH
Icecube 22			
Constant	cst (Hz)	3.2×10^{-5}	2.02×10^{-4}
	χ^2_{red}	2.74	0.50
Sinusoidal	a (Hz)	7.9×10^{-6}	5.5×10^{-6}
	b	-0.01807	-0.01807
	c (MJD)	54566.9	54566.9
	d (Hz)	3.3×10^{-5}	2.02×10^{-4}
	χ^2_{red}	0.36	0.53
Icecube 40			
Constant	cst (Hz)	7.10×10^{-4}	4.35×10^{-4}
	χ^2_{red}	3.05	0.94
Sinusoidal	a (Hz)	4.67×10^{-5}	-5.87×10^{-7}
	b	-0.0184	-0.0184
	c (MJD)	54930.8	54930.8
	d (Hz)	7.14×10^{-4}	4.35×10^{-4}
	χ^2_{red}	1.88	0.97

Table 6.1.: Rate fit parameters and errors for IC22 and IC40, for the Northern and Southern skies. The goodness of the fit is evaluated with the reduced χ^2, $\chi^2_{\text{red}} = \chi^2/(n.d.f.)$ (n.d.f.= number of degrees of freedom). The sinusoidal fit is parametrized as: $a \sin[b(t-c)] + d$.

and width of the flare should be added as free parameters in the minimization process. However, a faster semi-binned approach is adopted, namely, $\mathcal{L}$ is only calculated for the most promising flare time windows. When compared to the general minimization method, the approach used in this thesis gave similar results.

The time windows are previously selected based on the times of the most signal-like events from the analyzed data. A signal-like event is defined as having $S_i/B_i > 1$, where S_i (Eq. 6.11) and B_i (Eq. 6.10) come from the time-integrated method, including spatial and energy terms. Each pair of these event times assigns a starting and ending time (t_s and t_e, respectively) of the flare search time window ($\Delta t_i = t_e - t_s$). For each Δt_i, defined by any set of signal-like events, a significance parameter λ_i (Eq. 6.9) is calculated. The semi-binned algorithm returns the best λ_i, λ_{max}, corresponding to the most significant cluster. The significance is obtained as in the time-dependent unbinned maximum likelihood method. The largest flare duration is constrained in the algorithm to be less than 30 days, which is sensible from γ-ray observations.

The test statistic λ is defined as in Eq. 6.9 and the general form of $\mathcal{L}$ as written in Eq. 6.8 is the same. The background probability distribution function, B_i, (Eq. 6.10) is modified by adding a time term:

$$B_i = P_i^{space}(\theta_i, \phi_i) P_i^{energy}(E_i, \theta_i) P_i^{time}(t_i, \theta_i) \ , \tag{6.15}$$

where the new term $P_i^{time}(t_i, \theta_i)$ describes the time probability distribution of the background. The azimuth correction included in $P_i^{space}(\theta_i, \phi_i)$ becomes important for time scales shorter than 1 day, reaching up to 40% and 75% difference for IC22 and IC40

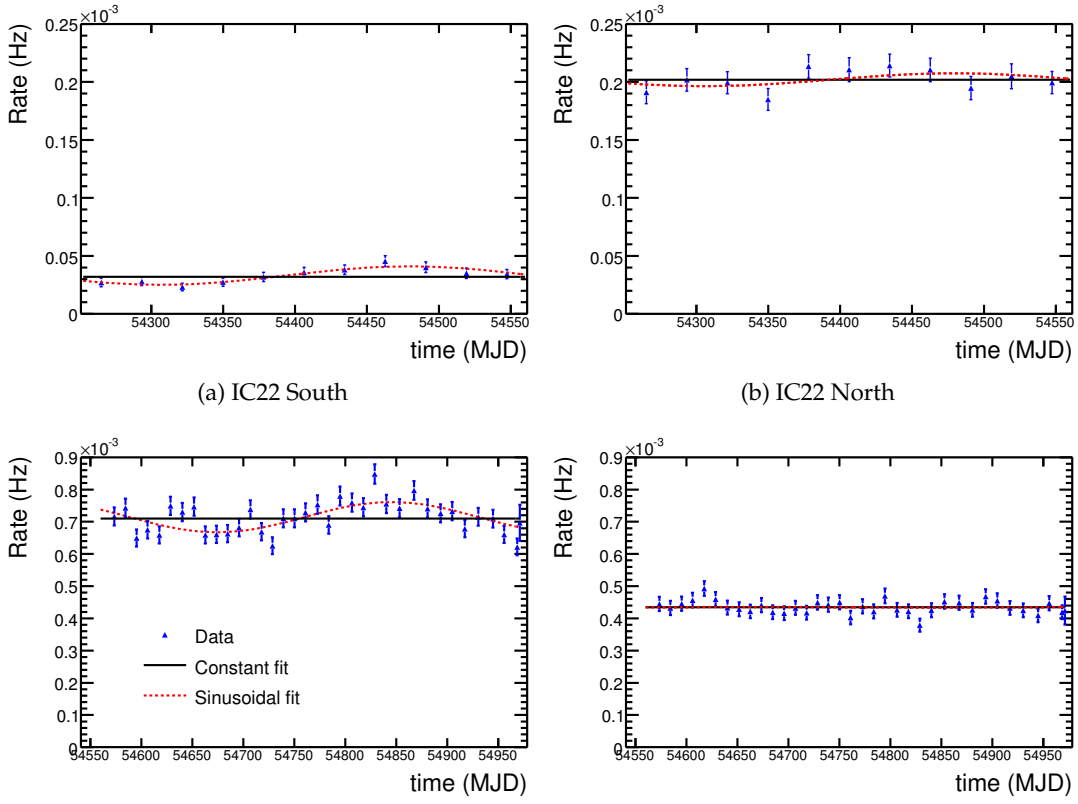

(a) IC22 South

(b) IC22 North

(c) IC40 South

(d) IC40 North

Figure 6.7.: Uptime corrected rates and their fits for the Southern and Northern skies for IC22 and IC40.

respectively, thus its importance for time dependent analyses.

The time probability P^{time} is defined by:

$$P_i^{time}(t_i, \theta_i) = \frac{1}{\Delta T_{tot}} R(t_i, \theta_i) \ , \tag{6.16}$$

where ΔT_{tot} is a normalization constant to the whole data taking period and $R(t_i, \theta_i)$ is a normalized fitted function of the event rates in the entire observed period as a function of time (t_i). Two regions of the sky (South and North) are distinguished because they have different properties, thus the zenith, θ_i, dependence of P^{time}. The Northern sky sample, made up mostly of atmospheric neutrinos, uses a constant. For the Southern sky, a sinusoidal fit is applied because it is dominated by a background of high energy atmospheric muons (see Sec. 6.3.1 for a further discussion of the fits). The sinusoidal fit is given by:

$$R(t_i, \theta < 90^o) = 0.066 \sin(-0.018\ (t - 54930.8)) + 1 \ , \tag{6.17}$$

where t is given in MJD.

The signal pdf, S_i, (Eq. 6.11) is modified by adding a time term:

$$S_i = P_i^{space}(\mid \vec{x}_i - \vec{x}_s \mid, \sigma_i) P_i^{energy}(E_i, \theta_i, \gamma_s) P_i^T \ , \tag{6.18}$$

where the time probability, P_i^T, is constant since no flare time structure is assumed (i.e. taken to be uniform in time). For each Δt_j, time window tested, it is normalized by $P^T = \frac{1}{\Delta t_j}$. This is equivalent to an uniform distribution with boundaries the starting and ending times of the flare. This definition of P^T gives more significance to shorter flares. Other shapes of the flares could be assumed (i.e. Gaussian), however, since few events are expected, there is not much power to differentiate the cases.

Background and signal simulation

The background distribution of the test statistic for the best flare is based on data. The best significance obtained for a cluster can be corrected for trial factors, arising from testing different time windows for the same source direction, by using simulations. In order to represent a background-only observation, the properties of the data events (e.g. zenith, azimuth, time, reconstruction error and energy estimator) are randomly selected from their distributions while keeping the possible correlations between these parameters.

Experiments where a signal flux is present, can be recreated in simulation by injecting signal events on top of the background data. The significances obtained in these cases can be compared to the background-only hypothesis in order to calculate the discovery probability.

The properties of signal events are taken from a dedicated signal simulation and depend on the assumed energy spectral index. The reconstructed event direction has a certain error. The deviation from the true source location is reproduced with the Point Spread Function (PSF), by smearing the events around the source location. In order to investigate possible starting times of a flare, the whole data taking period is scanned, injecting randomly signal events inside the tested time window (i.e. flare duration).

The distributions from IC40 background-only simulations of the most important calculated parameters (λ, n_s, Δt) and their correlations are presented in Fig. 6.8a. In the Δt versus λ plot it should be noticed that the highest significances come from pairs of events (doublets or triplets) in a very short time and from clusters of several events in a time window of the order of days. The Δt versus n_s plot emphasizes the more frequent occurrence of doublets in short time scales, rather than larger clustering of events, which is expected from a randomized time distribution of the background.

If a simulated 15-minute flare with Poisson mean of 5 events is injected to the background, Fig. 6.8b is obtained. The λ distribution in number of trials (i.e. simulations) shows a peaked structure. This structure corresponds to the superposition of different number of injected events. Since the injected signal events follow a Poisson distribution with mean of 5 events, there is a range of actual injected events. As the number of actual injected signal events is increased, the λ distribution shifts to higher values with respect to the background-only simulation, representing a larger significance. In the Δt versus λ plot it can be seen that the largest density of simulations is concentrated at flares with duration equal or less to 15 minutes (=10^{-2}days). This shows how the method is finding the right flare, which was simulated for 15 minutes [4], since for background-only simulations, longer flares (i.e. in the order of days) would be found.

[4]The exact duration of the flare can be less since the signal events were injected randomly inside the 15-minute time window.

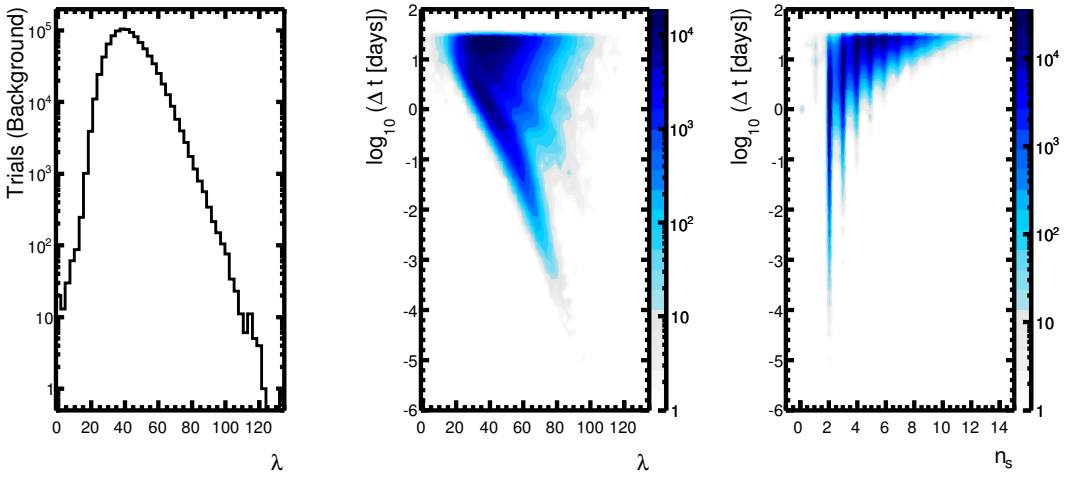

(a) Background only simulations

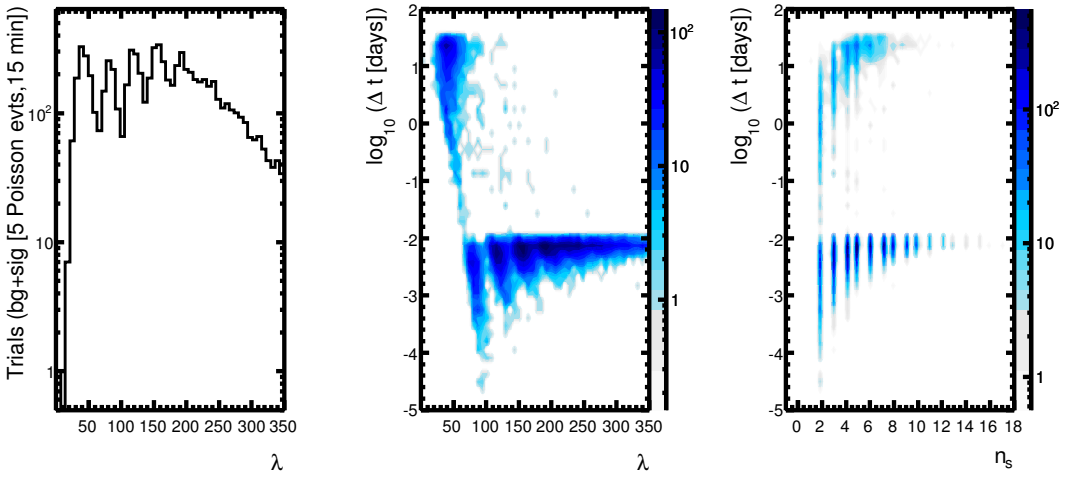

(b) Background plus signal simulations

Figure 6.8.: Probability distribution functions of the best test statistics (λ) from all time window combinations in IC40. Top: for background-only simulations for dec=16^o ra=343^o. Bottom: for simulations of background plus a signal given by a Poisson distribution with mean 5 events and flare duration of 10^{-2} days, for dec=16^o ra=343^o. Left: λ in terms of trials (i.e. simulations). Middle: duration of the flare versus λ. Right: duration of the flare versus estimated number of events.

Detection probability

The performance of a method can be assessed by means of the detection probability. The higher the detection probability, the better a method is. This probability, which depends on the signal strength and duration of the flare, is the fraction of experiments in which the background-only hypothesis can be rejected at a certain confidence level. This fraction can be calculated using simulations.

The neutrino flare 3σ detection probability for all IC40 selected sources as a function of declination is shown in Fig. 6.9, for the particular case of a 1-day flare injecting signal (E^{-2} energy spectrum) with 5 Poisson mean number of events. The binned and unbinned methods are compared. There is a 12% average improvement of the unbinned implementation over the binned one.

The regions outside the horizon, the horizon being at declination zero, show a higher detection probability. This effect is caused because there are less background events left in those areas and the same number of signal events is always injected for all declinations. In a real situation, the signal events would also be reduced, especially in the Southern sky but also in the most northern areas of the sky. This is caused by Earth absorption and the selection cuts. The region with the highest acceptance of signal neutrinos is located just below the horizon ($\delta > 0$).

In the declination range between $-10 < \delta < 0$ there is essentially no improvement from the unbinned method. In this region, the energy distribution of both background and signal events has its widest energy range because of the energy sensitive cuts applied in the event selection. In the transition to the Southern sky, the cuts reject lower energy events, increasing the energy minimum threshold steeply with lower declination.

In this declination region, the energy range of background is 10^3-$10^{5.4}$ GeV (c.f. Fig. 6.4) and for an E^{-2} signal it is $10^{3.3}$ to $10^{5.6}$ GeV (c.f. Fig. 6.6). The energy ranges of background and signal overlap, thus cancelling the discriminating power of the energy term in the likelihood (unbinned method). Therefore the unbinned and binned methods give similar results, since the binned method contains no energy weighting. It should be remarked that an energy weighting is not exclusive to the unbinned method. However, the binned method implemented here does not contain such a term.

Outside this region, the overlap of background and signal in the energy distribution is lower, thus allowing the energy term in the likelihood to play an important role in separating signal from background events.

The following discussion focuses on a particular direction in the sky (i.e. dec$= 16^o$, where the variable quasar 3C 454.3 is located), where the effect of the flare duration is analyzed. The number of Poisson average events needed for a 5σ discovery with 50% chance is calculated for different widths of the flare. The flare duration is investigated in the range from minutes to 30 days, though the algorithm can find shorter flares. In fact, the method is capable of finding GRBs (i.e. flares in the order of seconds or less), however it is unlikely (<1%) that a GRB would have the same coordinates of other flaring objects (e.g. blazars).

The results using IC40 data are shown in Fig. 6.10a. For this range of time-scales, the time dependent untriggered search needs less signal events to yield a discovery in comparison to a time integrated search. For a flare in the order of minutes, one third of the events needed in a time integrated search is necessary for a detection with the untriggered flare method. For short time-scales the number of events needed for a

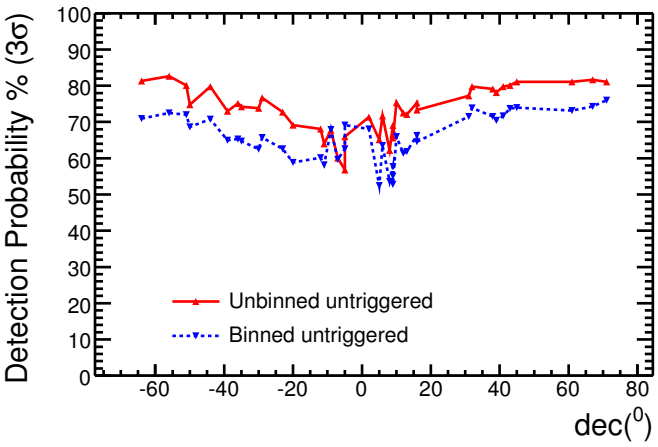

Figure 6.9.: Detection Probabilities for 40 selected sources distributed in declination for a Poisson distribution of injected (E^{-2}) signal events with mean=5, for a 1-day flare (3 sigma).

discovery approaches a threshold value of two, since always a pair of events is required to define a time window.

The longer the flares, the higher the improvement of the unbinned method over the binned one. For a several day flare, the unbinned method yields over a 20% enhancement. The explanation behind this effect lies in the number of background events. For longer flares, there are more background events. These events are distinguished from signal events more efficiently by the unbinned method, especially due to the energy term. However, for flares of width less than one day, the number of background events is less than one (see Fig. 6.10b), therefore the differentiating power of the unbinned contributes less.

Since the number of background events inside a flare of width less than one day is less than one event (see Fig. 6.10b), the difference between binned and unbinned methods remains constant at short time scales.

A third curve is also compared in Fig. 6.10a, namely the one corresponding to an unbinned method without a time term but applying the time-clustering algorithm. It can be seen that for flares shorter than 1 day, there is not a noticeable improvement due to the fact that most of the time the search is background free in these cases. Therefore only signal events are present and there is no weight in the likelihood (with no time term) that gives a higher weight to events coming closer in time (i.e. inversely proportional to the duration of the flare).

Fluence

If no flare is detected, an upper limit for the fluence can be calculated. The fluence is defined as the integral in energy (90% confinement) and time (Δt) of the flux upper limit:

$$f = \int_{t_{min}}^{t_{max}} dt \int_{E_{min}}^{E_{max}} dE.E \frac{dN}{dE} = \Delta t \int_{E_{min}}^{E_{max}} dE.E \left(\Phi_0 E^{-2}\right) = \Delta t \Phi_0 \left[\ln(E_{max}) - \ln(E_{min})\right] \ , \tag{6.19}$$

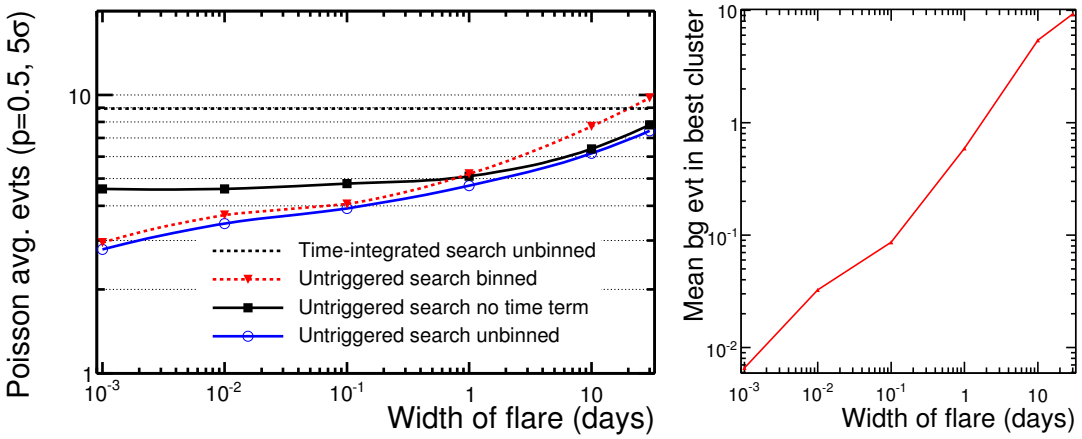

(a) Poisson average events for discovery

(b) Mean background events

Figure 6.10.: Left: Number of Poisson average events for a P=0.5, 5σ discovery for different flare durations and methods, calculated as an example for dec=16^o ra=343^o. Right: Mean number of background events in the best cluster using the unbinned method, for different widths of the flare, when 5 signal events are injected in the direction: dec=16^o ra=343^o.

where a neutrino energy spectrum of E^{-2} has been chosen as an example and Φ_0 is the flux upper limit.

6.4. Comparing binned versus unbinned methods

A corollary of these analyses is the confirmation that unbinned methods are more powerful than binned methods for time-integrated analyses as well as for time-variable ones. In the case of the time-integrated search done with IC22 a declination-average improvement of 35% in sensitivity (see Sec. 6.5.1) is obtained for the Northern sky [BA08a]. This is explicitly seen in Fig. 6.11 where also the discovery potential (see Sec. 6.5.2) is included. The improvement is rather steady over all declinations, however above the horizon it decreases. The main reason for this change is that the sample used for the unbinned method in IC22 was not optimized declination-wise and above the horizon this becomes critical. The improvement of this particular unbinned method comes from the fact that it includes more information in the analysis regarding the error in the directional reconstruction and the energy of the events, where the latter makes the largest difference. In addition, by including more variables in the likelihood the systematic errors are also increased.

It should be noticed that the inclusion of an energy term (weight) is not exclusive of unbinned (i.e. likelihood) methods. Therefore a fair comparison would exclude the energy term in the likelihood, leaving a $\sim$10% improvement. The inclusion of an energy term in the likelihood improves the results by $\sim$23%.

In the case of a time-dependent (untriggered) analysis the detection enhancement coming from an unbinned method depends on the duration of the neutrino flare as shown in Fig. 6.12. For very short flares, where the background is almost negligible, the

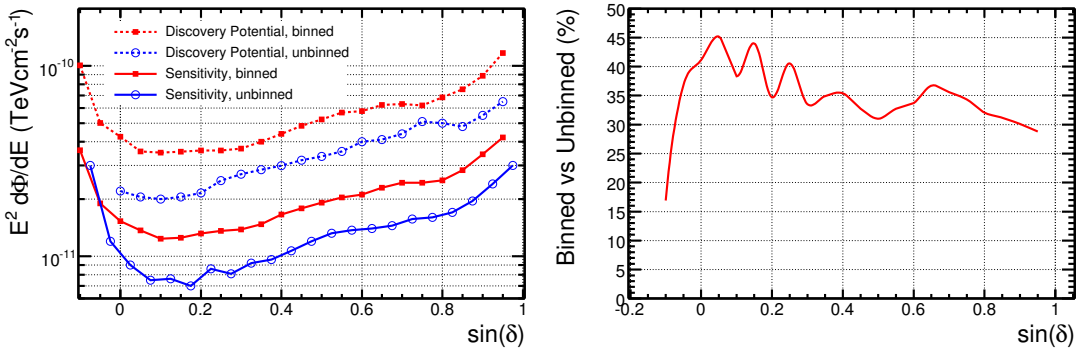

(a) Sensitivity and discovery potential (b) Sensitivity improvement

Figure 6.11.: Left: IC22 sensitivity and discovery potential to point sources with E^{-2} spectrum as functions of declination comparing the time-integrated binned and unbinned methods. The unbinned method results are taken from [A$^+$09b, BA08a]. Right: Improvement of the unbinned method over the binned method in sensitivity (E^{-2} spectrum) for IC22 as function of declination.

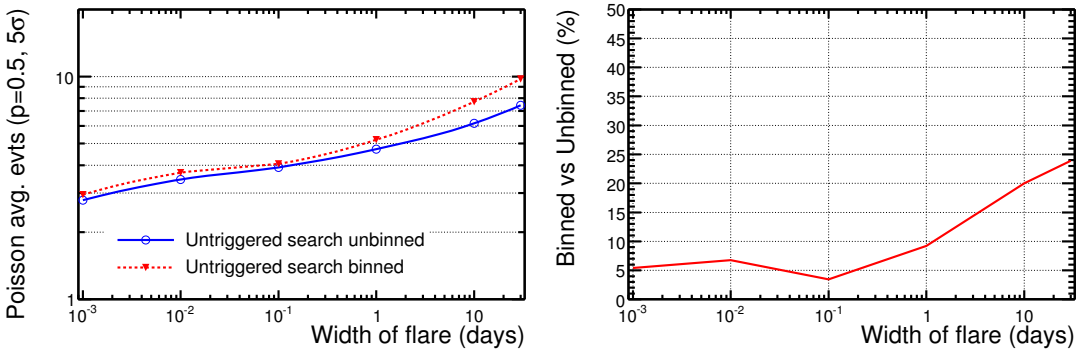

(a) Discovery (b) Discovery improvement

Figure 6.12.: IC40 discovery potential to point sources with E^{-2} spectrum as functions of the flare duration comparing the untriggered time-dependent binned and unbinned methods. Improvement of the unbinned method over the binned method in discovery potential (E^{-2} spectrum) for IC40 as a function of the width of the flare.

improvement is reduced to less than 10%, because the power of distinguishing signal from background is not used as often as when more background events are included by increasing the scanned time-window. Therefore, for longer flares the improvement increases to values larger than 20%. As seen in Fig. 6.9 the enhancement for objects distant from the horizon is larger, given that the energy regions (due to applied cuts and Earth absorption) of signal and background are not overlapping as much as around the horizon.

6.5. Sensitivity and Discovery Potential

When optimizing an analysis, two alternatives are available [H$^+$05], either to aim for setting limits (sensitivity) or for making a discovery. According to the goal of the analysis, the cuts used to select the final event sample can be tuned in a different way. Each approach is discussed below.

6.5.1. Sensitivity and Upper Limits

In order to optimize the event selection for the best sensitivity the expected upper limit is minimized, assuming the absence of a signal in the data. The model rejection factor (MRF), which is the ratio between the flux the analysis can exclude and the predicted flux, is then minimized.

Before making a real observation, a sensitivity, Φ_{sen} (see also Eq. 6.1), in terms of a flux amplitude, can be calculated in a Poisson counting experiment by [H$^+$05]:

$$\Phi_{sen} = \Phi_0 \frac{\mu_{90}(\mu_b)}{\mu_s} \ , \tag{6.20}$$

where Φ is the assumed amplitude of the signal flux described by $\Phi(E) = \Phi_0 E^{-\gamma}$, where the shape of the energy, E, is modelled by a power law (the standard assumption is $\gamma = 2$), $\mu_{90}(\mu_b)$ is the average upper limit at 90% C.L. estimated from the expected background events, μ_b, which is calculated from data where no signal is assumed and μ_s is the number of expected signal events calculated from MC, obtained by:

$$\mu_s = \int \Phi(E)\epsilon(E)dE \ , \tag{6.21}$$

where $\epsilon(E)$ is the detector response as a function of the particle's energy.

A flux upper limit Φ_{lim} can be calculated after an observation has been made, giving as a result n_{obs}, the number of observed events, by:

$$\Phi_{lim} = \Phi_0 \frac{\mu_{90}(n_{obs}, \mu_b)}{\mu_s} \ , \tag{6.22}$$

where $\mu_{90}(n_{obs}, \mu_b)$ is the event upper limit that can be estimated using two different approaches: Neyman or Feldman-Cousin [FC98]. This two approaches are:

- **Neyman approach**: The Neyman [Ney37] upper limit is constructed by asking that in 90% of the experiments (simulations) at least the median test-statistic (λ) coming from only background simulations is reached.

- **Feldman & Cousins approach**: The Feldman & Cousins experimental sensitivity [FC98] is defined for the measurement of a Poisson variable as *the average upper limit that would be obtained by an ensemble of experiments with the expected background and no true signal*. This approach constructs the confidence interval using the likelihood ratio as ordering quantity and ensures that no unphysical values are included.

The Feldman & Cousins limits are more conservative than the ones from the Neyman approach, namely their values are higher. The difference between both limits is at the level of 10%.

6.5.2. Discovery Potential

In order to claim a discovery, it is common practice in several experiments, including the ICECUBE Collaboration, to set a high threshold (5σ after trial corrections) for the probability (p-value) of such observation being caused by the background only hypothesis:

$$P(\geq n_{obs}|\mu_b) < \alpha,\ \alpha = 2.865 \times 10^{-7}\ , \tag{6.23}$$

where α corresponds to a 5σ deviation in a Gaussian distribution in the one-sided case. For a binned method $P(a|b)$ is the cumulative Poisson probability of observing a signal as high as a or larger given the expected mean b. In the case of an unbinned method the probability P is constructed from the distribution of the test-statistic λ for background-only simulations. Then this distribution is integrated for values $\lambda \geq \lambda_{obs}$.

The discovery potential (no observation yet made) is defined [H$^+$05] as the minimum signal flux needed for a 5σ detection with probability β (e.g. 50%), similarly to Eq. 6.20:

$$\Phi_{disc} = \Phi_0 \frac{\mu_{lds}(\mu_b)}{\mu_s}\ , \tag{6.24}$$

where μ_{lds} is the number of least (minimum) detectable signal events. In order to obtain μ_{lds}, first the threshold number of necessary observed events, n^{th}_{obs}, for a 5σ detection is found from $P(\geq n^{th}_{obs}|\mu_b) < \alpha$. Then μ_{lds} is calculated from $1-\beta = P(\geq n^{th}_{obs}|\mu_b + \mu_{lds}) < \alpha$, where β is chosen to be 0.5, such that in 50% of the experiments there would be a 5σ discovery.

6.6. Note on Blindness

In the ICECUBE Collaboration a blindness policy is adopted. A blind analysis [Roo03] is done in order to prevent optimizing the event selection or analysis on a statistical fluctuation. A bias can be present when the neutrino sample is selected (physics parameters and cut values), when the astrophysical sources are chosen or when the method is defined. These selections should not be tuned with the final data.

There are several ways to preserve blindness, one is to use a small subset of the events to tune the cuts, a *burn sample*, not used in the final analysis after *unblinding*, with the cuts and analysis fixed the rest of the data are analyzed. Another way is to hide the signal region, as is the case for GRBs. In the case of point source searches, the right ascension of the events is randomized (shuffled), thus if they were pointing in the same direction, this clustering is lost. Each of the three analyses presented in this thesis

underwent an unblinding process, which is the revision procedure of the analysis until it is approved and the real data can be used.

6.7. Note on Trial factors

If different tests are performed on the same dataset, a penalty (trial factor) should be accounted for when giving the final p-value. If no trial factor is taken into account, then by increasing the number of tests, the probability of rejecting the null hypothesis also increases. A fake discovery can happen because it is more likely to find an upward fluctuation of the background, if multiple tests are carried out.

The trial factor, T, of applying N analyses is defined by:

$$T = \frac{P_{post}^N}{P_{pre}} \ , \tag{6.25}$$

where P_{post} is the post-trial p-value and P_{pre} is the p-value without trial corrections. Depending on the actual case, N can represent the number of sources from a catalog, the number of bins in the sky, the number of independent tests or the number of experiments in general. It can be calculated that:

$$T = \sum_{i=N-1}^{i=0} (1 - P_{pre}) = \frac{1 - (1 - P_{pre})^N}{P_{pre}} \ . \tag{6.26}$$

If $P_{pre} \ll 1$ then $T \simeq N$, the trial factor is equal to the number of experiments. When the experiments are not independent (e.g. overlapping bins in the sky) dedicated simulations are needed to calculate the real trial factor which would be less than the number of experiments. Taking $T = N$ would be a conservative approach.

As an example the trials generated by using a list of sources is analyzed. In case of IC22, 28 sources were selected, therefore $N = 28$. However the local angular regions around these sources are not entirely uncorrelated (i.e. some overlap), thus an effective number of sources, N_{eff}, can be calculated using simulation (i.e. by shuffling the azimuth direction of the data events and repeating this test several times). N_{eff} is defined from Eq. 6.26:

$$N_{\text{eff}} = \frac{\ln(1 - P_{post})}{\ln(1 - P_{pre})} \ . \tag{6.27}$$

In Fig. 6.13 the trial factor, calculated from Eq. 6.26 and by simulation, and the effective and real number of sources are plotted for different p-values. Since there are correlations between the source locations, it is observed that the true trial factor (i.e. from simulations) is smaller than what is obtained using Eq. 6.26 with $N = 28$. Furthermore, the effective number of sources is closer to 20. The structure of N_{eff} is due to the discrete nature of the binned analysis being a Poisson-like experiment. The two trial factor curves approach as the p-value increases and will converge to 1, since p-values are probabilities and therefore cannot be greater than 1. For small p-values it can be verified that $T \simeq N$ holds.

The overall trial factor arising from performing two searches (i.e. pre-defined catalog and all-sky) can be calculated using simulations based on (randomized) data. A conservative approach would be to use $T = 2$. As seen in Fig. 6.14a, background fluc-

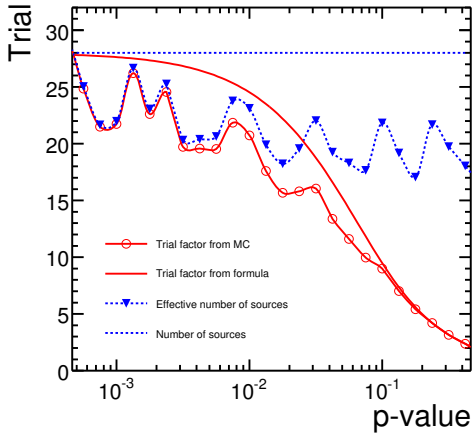

Figure 6.13.: Trial factor according to the p-value for the list of 28 source in IC22 from the time integrated binned analysis.

tuations can be more easily found if more directions of the sky are tested. Looking at all directions in the Northern sky yields higher p-values than looking at a few sources (list). Thus in order to exclude a background fluctuation at a certain confidence level a trial factor is applied.

The individually trial-factor corrected p-values for the source list and Northern sky is presented in Fig. 6.14b. The result of choosing the best of both p-values is also shown. The final corrected post trial p-value from both searches, that takes into account their correlations, comes from integrating the latter curve for p-values greater than the maximum p-value from either the list or the Northern sky searches.

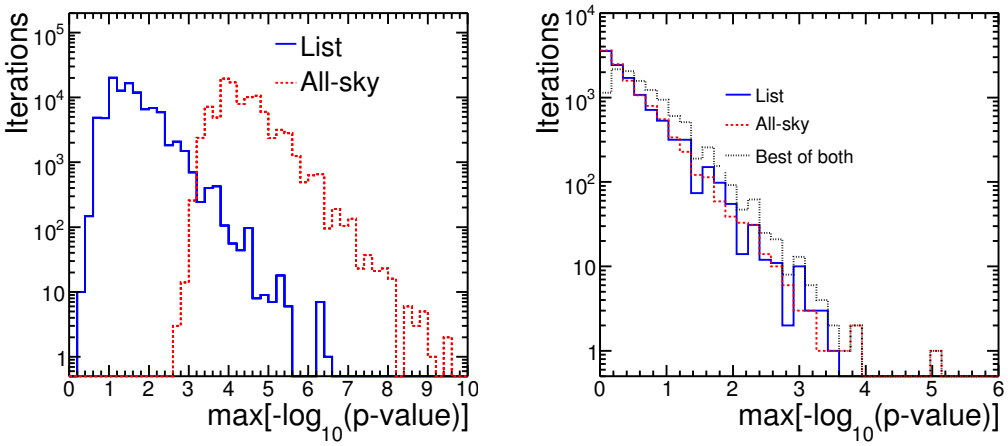

(a) Individual trials

(b) Corrected trials

Figure 6.14.: Distributions of the excess parameter for trial correction in IC22.

7. Data & Event selection

Wege entstehen dadurch, dass man sie geht.
Franz Kafka 1883-1924

The analyses presented in this thesis center on data taken by the ICECUBE detector (described in Sec. 4). The detector, still under construction, has increased its implemented volume each year by deploying more strings. Therefore for each year there has been a different running string configuration. During the period this thesis was developed, data from two ICECUBE configurations were available, processed and used: the ICECUBE 22-string (IC22) (see Sec. 4.1.1) and ICECUBE 40-string (IC40) (see Sec. 4.1.1) configurations.

IC22 data were analyzed using a time-integrated and a time-dependent method. Different event samples (i.e. event selections) are used. Only one sample is described in detail, because it was developed within the context of this thesis. IC40 data were examined with a time dependent method and a unified (all-sky) event sample was used.

Since this work is focused on point sources of neutrinos, the data selection will focus on track-like (muon) events which have the best angular resolution among the three types of neutrino event signatures.

In this chapter, the general data selection and processing are described, followed by the philosophy of the event selection and description of the cut variables used. Once the final event samples have been chosen, their main characteristics are presented and data is compared to simulation to establish the degree of agreement.

7.1. Detector stability

Because of the construction phase and continuous changes to the data acquisition and data processing at the South Pole, the detector has not been taking data uninterruptedly. Therefore, in order to select good data to analyze, the detector's stability and operation gaps needs to be checked .

7.1.1. Run selection

ICECUBE's main data unit is the *run*, with a unique identifier. Under stable operation conditions, each run corresponds to a data taking period of 8 hours, otherwise it is shorter. In order to define the list of usable data (good runs) for point source analyses, the following starting selection criteria were applied:

- Exclude flasher[1] and standard candle[2] runs. In both cases artificial light is in-

[1] Inside the DOM the flasher board contains 12 LEDs used to send light pulses to calibrate the timing and geometry of the array.

[2] An ICECUBE standard candle, is a pulsed nitrogen laser deployed on a string, that can simulate the Cherenkov light from a ν_e-induced cascade. It is used for calibration since its location and energy per pulse is well-known.

jected into the detector for calibration purposes and data should not be considered for physics analysis.

- Choose only runs where no detector issues were reported, regardless of the status of IceTop or AMANDA (TWR).

- Reject runs marked as bad by the monitoring group (e.g. runs with duration less than 10 minutes or test runs).

In order to improve the quality of the selected runs, it was required, within the context of this thesis, that:

- The duration of the run should be greater than 20 minutes (shorter runs are not monitored).

- The rate moving average [3] should not fluctuate more than 0.04 Hz from one run to the next. This ensures the stability of the detector and, at the same time, allows for a correct treatment of seasonal variations. The seasonal variations, which cause a gradual change in the atmospheric muon rates, due to atmospheric temperature variations, are preserved using the rate moving average.

After this selection, there are still runs with empty gaps due to DAQ problems. However, these runs are still used and the gaps are accounted for in the uptime estimation. The runs, duration and uptime of IC22 and IC40 are summarized in Table 7.1.

	First Run/ Date	Last Run/ Date	Total runs	Duration (days)	Lifetime (days)	Uptime fraction
IC22	107959 May 31st 2007	110773 April 5th 2008	1068	310	275.9	88.9%
IC40	110782 April 5th 2008	113821 May 20th 2009	1430	410	375.5	91.6%

Table 7.1.: Selected Good runs, data taking period and uptime fraction of ICECUBE in its 22-string and 40-string configurations.

7.1.2. Lifetime

The lifetime (uptime) of the detector corresponds to the sum of all periods when the detector was taking good data (i.e. runs that can be used for physics analyses). It is used to normalize a generic flux of simulated data to the actual number of days when events were recorded. Furthermore, for time-dependent analyses it is important to properly describe the uptime of the detector as a function of time throughout the year.

The detector is usually stable with a few breaks in data taking. The downtime is made up of: breaks between runs (1-5 min or more), empty gaps inside runs, times when the detector was completely down, removed short runs and bad runs.

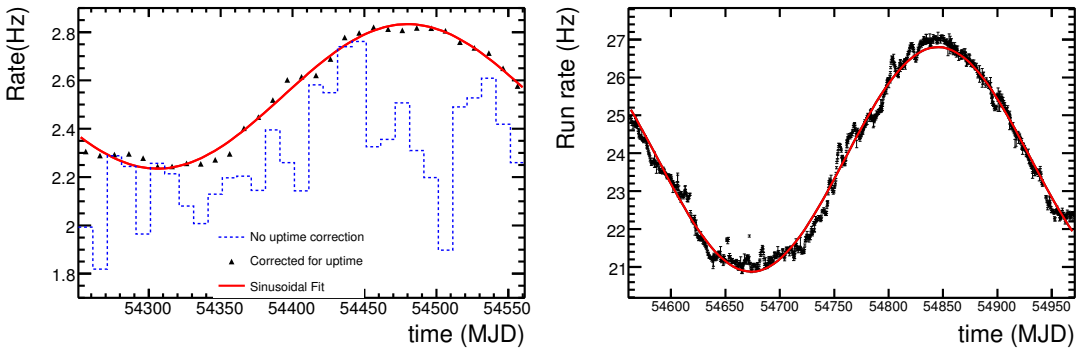

(a) IceCube 22 Level3 (b) IceCube 40 Level2

Figure 7.1.: Uptime corrected event rates as a function of time and their corresponding sinusoidal fit from seasonal variations.

Seasonal variations

In order to clearly observe the seasonal variations of atmospheric muons due to changes in the temperature in the middle stratosphere, the data rates need to be corrected for their partial uptime. In Fig. 7.1a 10-day average rates without and with uptime correction (i.e. using the real duration of the runs) are shown for IC22 at a filtering stage (Level3, see App. B.1) where data are still mainly composed of atmospheric muons. When the uptime correction is included, the seasonal behavior of the rates throughout the year becomes visible. The rates can be fitted with a sinusoidal function. Such a function describes in a first approximation the seasonal variations. However, the goodness of the fit is not optimal ($\chi^2/(n.d.f.) = 225.4$). This result can be expected since the rate variations within a year have, besides the major seasonal temperature changes, a much more complex behavior depending on the daily temperature. Nevertheless the fit is done in order to extract the phase (54566.9 MJD) and period (347.57 days) used for the fitting at higher level cuts (see Sec. 6.3.1).

In Fig. 7.1b the uptime corrected rates for each IC40 run are shown as a function of time. In such a graph without rate averaging, the day-wise atmosphere temperature changes are more pronounced, thus small oscillations inside the large seasonal pattern are observed. The goodness of the fit is slightly better ($\chi^2/(n.d.f.) = 53$). The obtained phase from the sinusoidal fit was 54930.8 MJD and the period 353.92 days.

7.2. Data processing

IceCube data undergo several processing stages called *Levels*, defined by the Collaboration. In Sec. 4.6 the main trigger, SMT trigger, and the physics filters were introduced. For point source analyses two physics filters are important: mainly the muon stream, but also the EHE stream for high energy searches. In App. B, Tables B.1 and B.3 present the cuts used to obtain these streams (Level2), for IC22 and IC40 respectively.

[3]The rate moving average is calculated from runs in the last 10 days. This backward range is update for every run, averaging out possible daily temperature fluctuations in the atmosphere, which would lead to a sudden rate variation.

The purpose of the muon filter is to select track-like muon-neutrino events while rejecting partially the overwhelming background of down-going atmospheric muons. The satellite bandwidth limitation between the South Pole and the data storage and processing in the North puts a constraint on the data rate assigned to the muon filter of about 25 Hz. The muon filter selection cuts are tuned to satisfy this constraint.

The muon filter distinguishes two regions of the sky: South (above the horizon) and North (below the horizon). A different event selection is needed in each region because the background is made up of different types of particles (event classes). In the Northern sky the main background are misreconstructed atmospheric muons (down-going events reconstructed as up-going events) and also coincident down-going muon events that can mimic an up-going neutrino event. In the Southern sky energy related cuts are needed in order to select the highest energy events, because at low energies the atmospheric muon background is extremely high. At energies above PeV, ultra high energy neutrinos can be analyzed [Lau10].

For IC22 data further processing was required because not all higher level reconstructions were included at Level2, due to CPU time constraints. At Level2 soft quality cuts were applied to reach Level3, bringing the rate down to $\sim$3.6 Hz (see the actual cuts in App. B.1). Since at Level3 the data rate has been reduced, other CPU time consuming reconstructions can be added: the angular error estimated (paraboloid), the Bayesian fit, the MPE (see Sec. 5.2.3) reconstruction and the energy estimator *mue* (see Sec. 5.2.5). In case of IC40 data, all reconstructions were already included at Level2.

7.3. Cut variables for event selection

Data at Level3 still mostly contain background events (e.g. atmospheric muons, coincident muons, etc). The purpose of an event selection is to reduce as much as possible this background contamination, while keeping the highest signal fraction. The cut variables are chosen accordingly to this goal. Some variables select events with a good angular resolution (key for point-source searches), others target specific kinds of background topologies (e.g. coincident muons: double, triple tracks), some energy related variables can separate low energy background from signal, etc. The cut variables used to arrive to the final samples of events are introduced in this section.

7.3.1. Parameters independent of the reconstructed direction

The following variables are straightforward to calculate and do not require fitting a track, thus are particularly useful for initial fast background rejection.

Number of channels

The number of channels (*NCh*) counts the number of DOMs included in the recorded event. It is a basic cut applied in the SMT trigger in order to have enough points to apply a directional reconstruction. If there are too few DOMs involved in an event, the lever arm is short and the corresponding angular resolution bad. It can also be regarded as a simple energy estimator, though it strongly depends on the track geometry. A high energy event will produce more light, thus triggering more DOMs (high NCh).

Hits per channel

Another variable that correlates better with energy, remaining simple, is the total number of hits (photo-electrons) in an event divided by the number of DOMs involved, short: *NHits/NCh*. More light is produced by a high energy event, registering more photo-electrons in a DOM, thus generating a higher NHits/NCh. This variable is useful for rejecting down-going muons above the horizon.

7.3.2. Parameters dependent on the reconstructed direction

Once an event has been reconstructed using a unbinned maximum likelihood method (see Sec. 5.2.3), several useful parameters can be calculated based on the track for further background rejection.

Reconstructed zenith

A basic output of a reconstruction is the *zenith* (θ), as well as the *azimuth* (ϕ) coordinate. Several event properties (e.g. energy, event density, etc.) greatly depend on zenith, mostly noticeable in the transition region around the horizon (above: Southern sky, below: Northern sky). The zenith variable helps to identify each region, where further cuts can be applied in a zenith dependent way.

Reduced LogLikelihood

The standard definition of the reduced log-likelihood (*RLogL*) is:

$$RLogL = \frac{\log(\mathcal{L})}{N_{dof}} = \frac{\log(\mathcal{L})}{N_{Ch} - N_{FitParam}} \ , \tag{7.1}$$

where $\mathcal{L}$ is the maximum likelihood of a track and the denominator, i.e. the number of degrees of freedom (d.o.f.), is given by the number of DOMs hit minus the number of parameters used for the fit (e.g. 5 parameters: x, y, z at $t = 0$, θ and ϕ, for an ideal infinite track). For a Gaussian probability distribution this expression would correspond to a reduced χ^2. However this does not strictly hold for the likelihood, leading to a dependence on NCh.

This variable, *RLogL*, has proven to be one of the most effective background reducers. Small values suggest that photons arrived as predicted by the convoluted Pandel function [Pan96] (see Sec. 5.2.3), therefore selecting good quality tracks and rejecting misreconstructed background events. However, it must be remarked that this variable is related to the track energy, affecting low energy events, since it includes the number of channels, thus if a wide energy coverage is desired, this variable has to be combined with others.

The likelihood in the definition of RLogL (Eq. 7.1) does not scale with the number of degrees of freedom. An effective definition, found by MonteCarlo simulations, tries to correct this problem, reducing the dependence on energy of RLogL. It is given by:

$$RLogL_{eff} = \frac{\log(\mathcal{L})}{NCh - 2.5} \ . \tag{7.2}$$

Bayesian ratio

As already mentioned in Sec. 5.2.3, the logarithm of the ratio between standard and Bayesian likelihoods:

$$Baye_{ratio} = \log(\frac{\mathcal{L}}{\mathcal{L}_{Baye}}) = \log(\mathcal{L}) - \log(\mathcal{L}_{Baye}) \ , \tag{7.3}$$

is used to reject misreconstructed muon background. The Bayesian likelihood uses a down-going atmospheric muon prior. Therefore a low value of the likelihood ratio would indicate that the event is most likely down-going. By definition this variable is useful in the Northern sky. After applying an angular cut to select events below the horizon, a condition on a minimum value of the Bayesian ratio rejects down-going events badly reconstructed as up-going.

Paraboloid Sigma

The parameter obtained from the angular uncertainty estimate (see Sec. 5.2.4), called *Paraboloid sigma* (σ_P), is defined for each event in terms of the paraboloid error ellipse estimates for the major (σ_x) and minor (σ_y) axes by:

$$\sigma_P = \sqrt{\left(\frac{\sigma_x^2 + \sigma_y^2}{2}\right)} \ , \tag{7.4}$$

where the result is given directly in angular units. Keeping events with small σ_P values improves the angular resolution. It also has a slight background rejection power, given the fact that most background events are low energetic and low energy events are usually harder to reconstruct with a good angular resolution.

The current implementation of paraboloid sigma for the MPE reconstruction does not accurately describe the angular error. Therefore its value has been rescaled as a function of the energy (see App. A) in order to match the true angular error.

Split Zenith

The zenith reconstruction results of the double-muon (i.e. two track fit) reconstruction (see Sec. 5.2.6) are used to form a cut parameter for rejecting down-going coincident muons that can resemble an up-going neutrino event. Such a parameter is used in the Northern sky, where only up-going events should remain. The *split zenith* cut requires a minimum reconstructed zenith independently for both tracks.

Energy estimator

The output from *mue* (see Sec. 5.2.5) is the best energy estimate available at the moment. It performs much better than *NCh* and *NHits/NCh*, since the estimate of the photon density (proportional to the muon energy) depends on the distance from the track. The other two approaches do not take into account this geometry dependence.

Therefore the mue energy estimate is used in the Southern sky to reject the large low energy background of atmospheric muons. In addition, it is also used as the energy

estimate for the signal and background energy probability distribution functions used in the unbinned likelihood method.

7.3.3. Parameters dependent on the time residual interval

The concept of residual time was introduced in Sec. 5.2.3 and is used to define the notion of *directness* of the hits (unscattered photons) with respect to a reconstructed track. Two time intervals are used in the present analysis:

- DirC: -15 ns$\geq t_{res} \leq 75$ ns.
- DirE: -15 ns$\geq t_{res} \leq 250$ ns.

Direct hits

The number of *direct hits* (*NDir*) is the sum of hits with small time residuals (within the above defined time intervals C or E). In the implementation used here only the first hit recorded in each DOM is used because it is usually less scattered. The more direct hits an event has, the easier it would be to reconstruct it, because the corresponding photons are less scattered, preserving the shape of the Cherenkov cone. This quality variable rejects misreconstructed events, given that hits associated with a false track would have larger time residuals.

However, the *direct hits* variable affects higher energy tracks even though they could be properly reconstructed because they have less direct hits. When only the first hit is chosen (SPE approach), it is more likely for higher energies that it is an early hit (before the time residual window), since there is a higher number of hits and because of the spatial distribution due to small cascades. If all hits would be included (MPE approach), then there would be more direct hits, given that for higher energies there are many more hits.

Direct length

The *direct length* is the distance between the projections of the two outermost direct hits onto the reconstructed track. A long direct length corresponds to a larger lever arm, thus better reconstructions are expected. Therefore a large direct length value rejects badly reconstructed events. As for the direct hits parameter, this quantity decreases the signal efficiency of high energy events because they have less direct hits.

Smoothness

The *smoothness* [A$^+$04] is a measure of the compatibility of the observed pattern of projected direct hits along a muon track, with the hypothesis of constant light emission by a muon. This parameter was motivated by the Kolmogorov-Smirnov test. A well reconstructible track is expected to have continuous hits along the particle path, since the muon emits steadily light that would be detected by the DOMs along its way. It has the property of identifying misreconstructed muons and therefore it is useful for improving the purity of the selected data sample.

7.3.4. Cut variables not used

Other cut variables were studied but not used for the actual event selection because they were less efficient. They include:

- The zenith difference between the SPE and Line-Fit reconstructions, which relates to the angular resolution of the track. If both reconstructions give the same direction, then it is more probable that it is the correct track. However, paraboloid sigma, the angular uncertainty estimate, gives a more precise direction error.
- The number of strings in which at least one DOM was triggered (*NString*). More strings are required to select higher energy events with a better angular resolution. However, one or few string events (lower energy) can still give good tracks and should not be rejected.
- Tensor of inertia and Cascade likelihood. Both parameters are used to select a different event topology, namely a spherical, cascade-like, event originated in neutral current interactions or by ν_e or ν_τ. In order to select track-like, muon, events these parameters would be used to reject cascade-like events. Nevertheless, these parameters were found to have lower background rejection capabilities than the used cut variables.

7.4. Cut optimization and final cuts for the time integrated search

As mentioned in the introduction of this chapter, only the IC22 Northern sky event sample used for the time-integrated binned point source search will be described in detail, since it was developed in this work. Compared to the unbinned event sample, it uses tighter cuts in order to reject more background. An unbinned method can accept more background events, since the likelihood can distinguish these events from signal. In addition, the binned event sample used a zenith dependent selection, motivated by the reconstruction and detection efficiency dependence on zenith.

The previously described cut parameters have been studied in order to obtain the IC22 binned time integrated event sample. Their background rejection capabilities, angular resolution improvement and signal efficiency were quantified. Before applying a CPU intensive cut tuning, the data amount at Level3 ($\sim$3.6 Hz) was further reduced to Level4 ($\sim$ 0.1 Hz) (see the actual cuts in App. B.1) using the new reconstructions added at Level3. The applied cuts help to reject coincident muon events, improve the angular resolution of the tracks and further select up-going events using the better MPE reconstruction. At Level4 the signal efficiency with respect to Level2 for a E^{-2} energy spectrum is $\sim$ 60%.

The following track quality parameters were included in the final cut optimization, starting with the event sample at Level4, since they present the highest background rejection power:

- Reduced LogLikelihood (RLogL) from the 32-iterations SPE track,
- Direct hits E (NDirE) from the MPE track,
- Bayesian Ratio from the 32-iterations SPE track,

- Paraboloid Sigma from the MPE track.

The parameters have a relative independence, addressing different classes of events, thus they can be used together. For example, the RLogL has a larger impact on low energy events, while NDirE affects high energy events

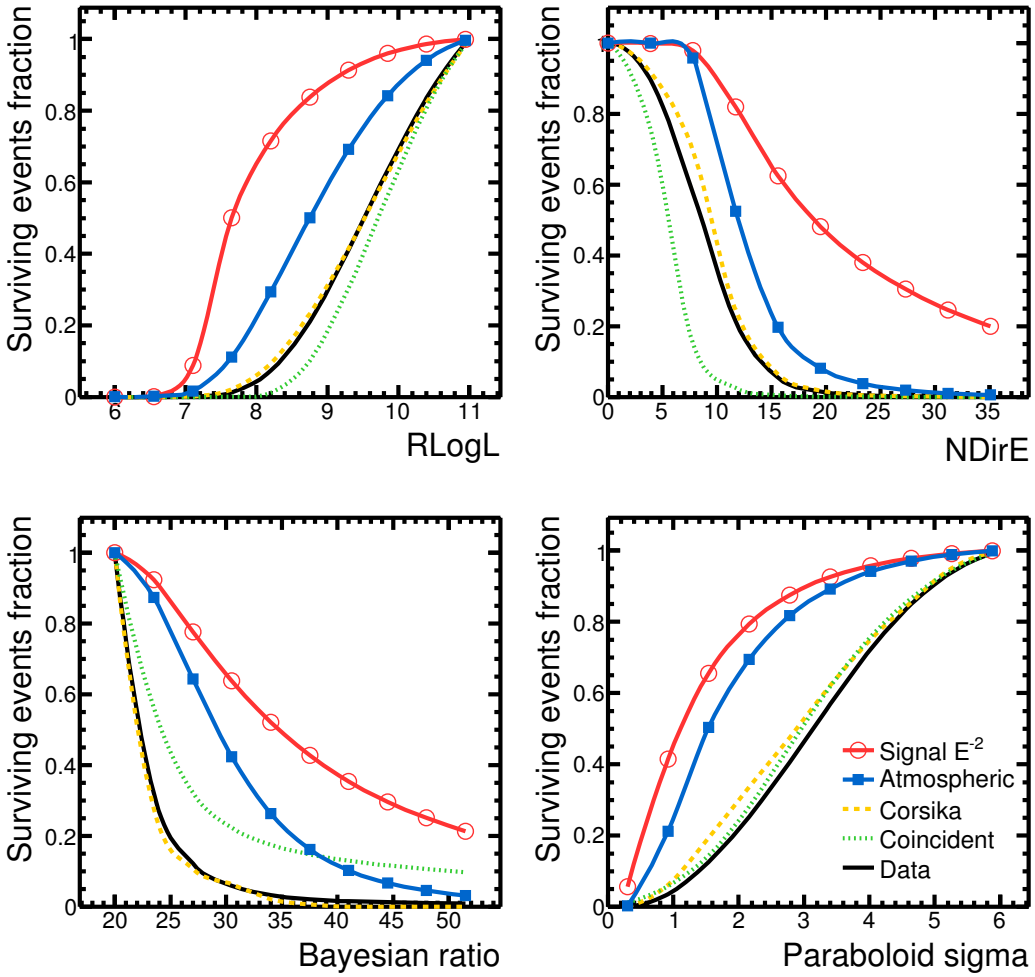

Figure 7.2.: Background rejection power for different cut parameters in IC22. The horizontal axis corresponds to the cut value applied.

The background rejection power of these parameters is illustrated in Fig. 7.2 by the fraction of surviving events, where data is compared to signal simulation (with a spectral shape of E^{-2}), atmospheric neutrino predictions, atmospheric muon simulation (Corsika) and coincident (double) muons simulation (Coincident). At this cut level (Level4) data follows the behavior of Corsika (i.e. atmospheric muons) and signal is always less affected by the cuts. The NDirE and also RLogL variables reject coincident events faster. Both cut variables are the most effective in reducing the level of background. The paraboloid error cut acts roughly in the same way on signal and atmospheric neutrinos and also on single and double atmospheric muons, however this variable has the least cutting power from the four presented here. Nevertheless, since it improves the angular resolution, it was also included.

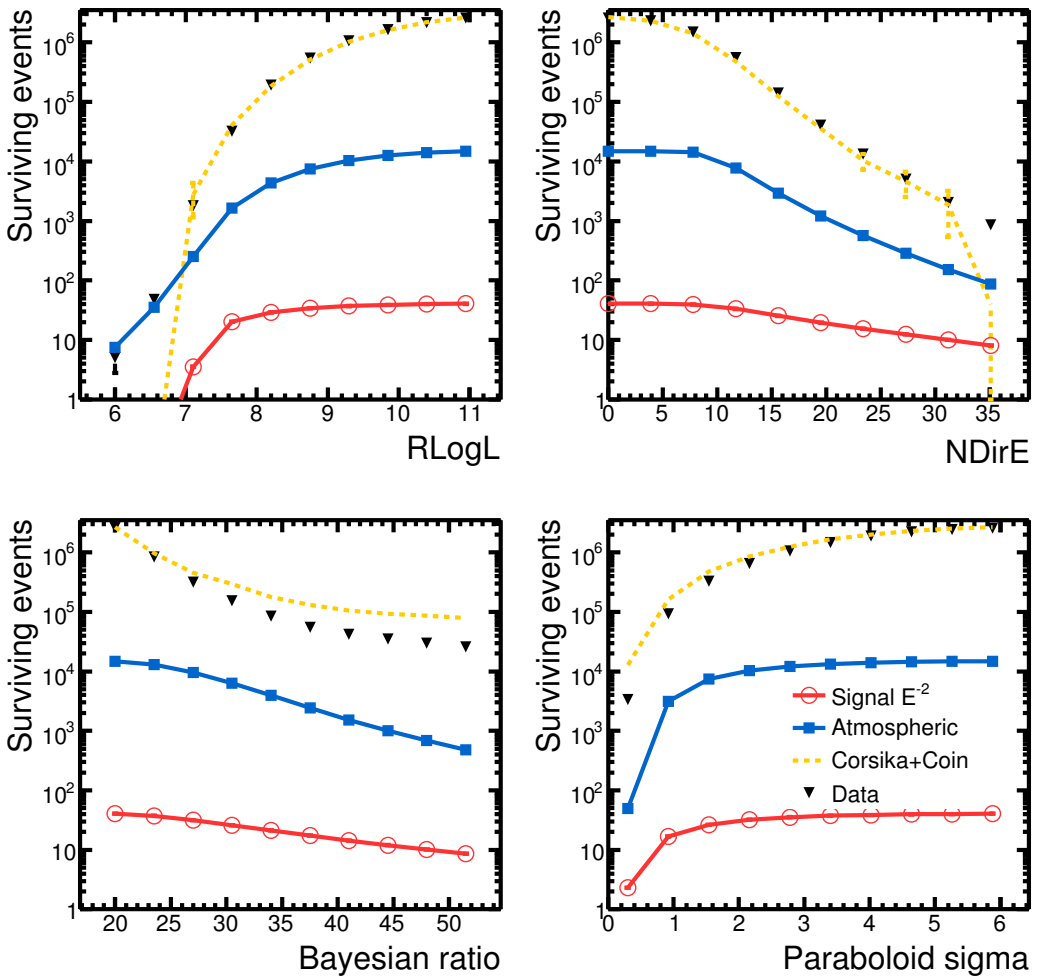

Figure 7.3.: Surviving events after increasing cuts for different kinds of background and signal in IC22. The horizontal axis corresponds to the cut value applied. *Corsika* and *coincident* refer to the single and double atmospheric muon events, respectively.

The number of surviving events after increasing cuts for these variables is shown in Fig. 7.3 for the different types of background and signal. These plots help to quantify the agreement in total number of events between data and background simulation by increasing cuts. Here both kinds of background simulated events (i.e. single and double atmospheric muon events: Corsika+Coincident) are added in order to reach the real number of data events. It can clearly be seen that RLogL could alone lead to an atmospheric neutrino sample for tight cut values. The transition from atmospheric muons to atmospheric neutrinos is evident at RLogL$\sim$ 6.6. This is the most powerful cut, having the strongest data reduction speed. However, it cannot be used alone for the final selection, given that for tight cuts the signal efficiency is very low and there is a slight disagreement between data and simulation for values lower than RLogL=7. If several cut parameters are combined, a better signal efficiency ($\sim$33% with respect to Level2) can be achieved, while reaching the same level of background rejection.

Given the reduced amount of background simulation, the NDirE plot is not continued for higher cut values. However, even if tighter NDirE cuts were applied, the data would not reach the atmospheric neutrino level. The Bayesian ratio is, of the four variables, the one with the least agreement between data and simulation. When estimating the systematic uncertainties (see Sec. 9.3.2), the disagreements between the four parameters in data and simulation are studied. The associated systematic error is calculated to be less than 2%.

The criterion used to optimize the cuts' values is the best sensitivity (see Sec. 6.5.1 for its definition), which is obtained with the binned method (Sec. 6.2.1) based on the F&C statistics [FC98]. The bin size is also a free parameter (in addition to those listed above) entering the optimization procedure. Because the reconstruction and detection efficiencies vary with declination, the cuts are optimized as a function of this coordinate (i.e. for different declination bands).

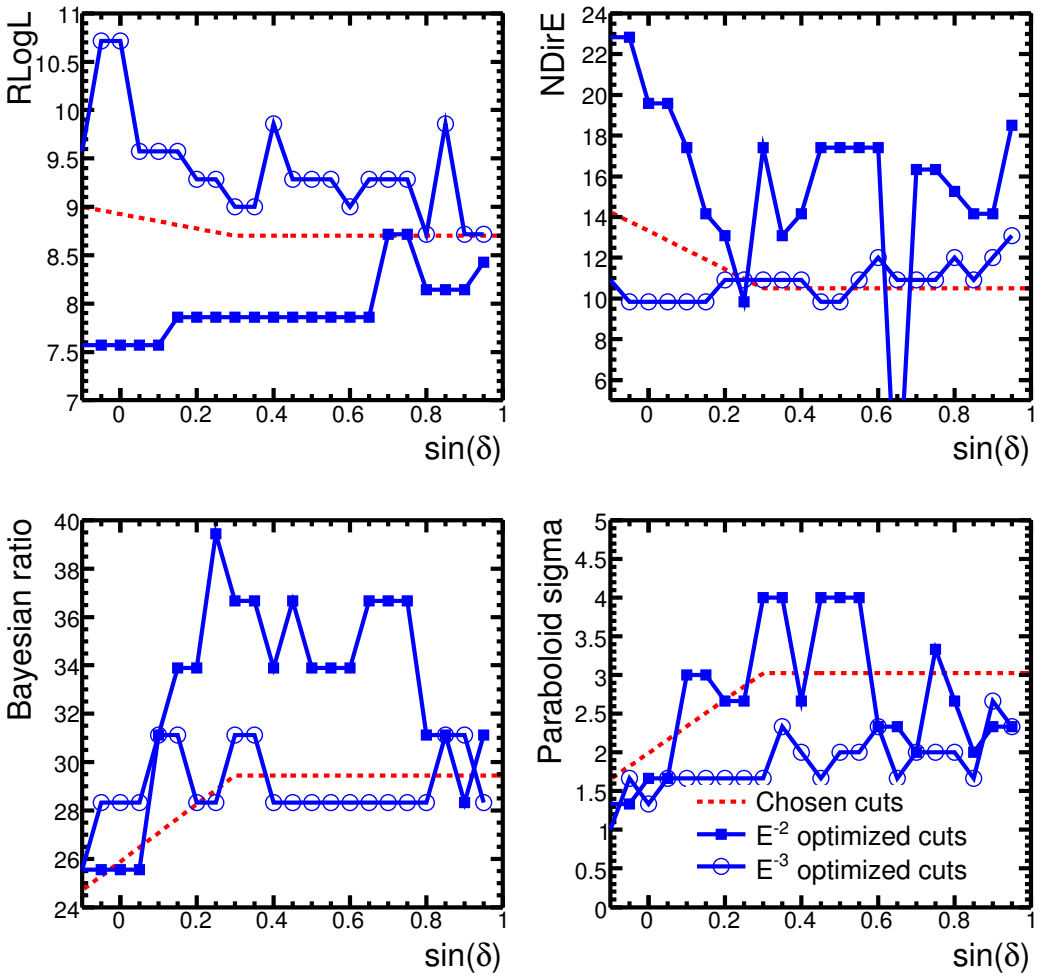

Figure 7.4.: Cuts values as a function of declination for the binned IC22 Northern sky sample.

An iterative procedure is carried out where individual cuts are progressively combined and the sensitivity is calculated. The best combination of cuts delivering the

best sensitivity (minimum MRF, see Sec. 6.5.1) is found separately for each declination band. The parameter space is investigated separately for an E^{-2} and E^{-3} energy spectrum, delivering a set of best cut values for each case. Cuts are finally parametrized to level out the effects of the statistical fluctuations of the background and are a compromise between the two spectra [A$^+$07a] (see Fig. 7.4). The cuts are relaxed and smoothed in declination, moving away from the best mathematical values, as much as not worsening the sensitivity by more than a few percent. The final parametrization of the cuts is given in App. B.1.

The cuts which have the largest effect on the event sample selection are RLogL and NDirE. This was expected since both variables have the largest background rejection capability. The Bayesian ratio cut is tighter for larger declinations, since the downgoing prior used in the likelihood reconstruction gives a worse result for more upgoing-like events. On the other hand, the paraboloid cut is tighter for events closer to the horizon, so that a better angular resolution can reject the mis-reconstructed downgoing atmospheric muon that constitute a larger contamination around the horizon.

In addition, the search bin radius (mean = 2.1°) is parametrized by (see Fig. 7.5):

$$Bin_R = 2.1 + 0.78\sin(\delta) - \sin(\delta)^2 \ . \tag{7.5}$$

The mean value of the search bin radius is 60% larger than the average median angular resolution. Even though the background is increased by enlarging the search bin, the signal that is included compensates with an improvement in sensitivity.

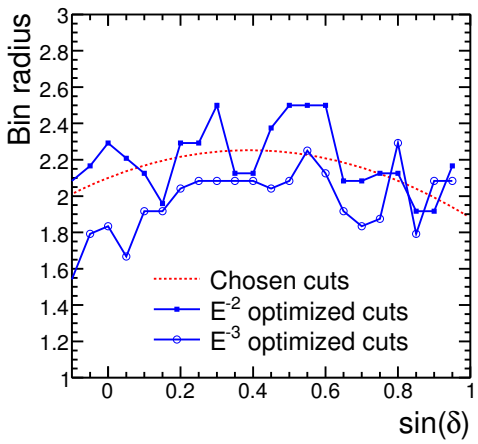

Figure 7.5.: Bin radius as a function of declination (binned IC22 Northern sky sample).

7.5. Event selection for the time dependent searches

7.5.1. IceCube 22-string unbinned untriggered flare search event sample

The IC22 untriggered flare search developed in this work, covers the entire sky (declination range from -50° to 85°). Since at the time of the analysis there was no unified event sample for unbinned searches, it was decided for simplicity and readiness to use previously obtained neutrino data samples for IC22. For this purpose two different event samples with different selection criteria were used, one for the Northern sky

[A$^+$09b] and another for the Southern sky [A$^+$09a]. For both samples event tracks are obtained with a multi-photoelectron (MPE, see Sec. 5.2.3) reconstruction, thus improving the angular resolution for high energies with respect to the single-photoelectron (SPE, see Sec. 5.2.3) reconstruction.

ICECUBE 22-string Northern sky

The Northern sky event sample was optimized, in the context of the unbinned method, for the optimal sensitivity to both hard and soft spectrum sources. Given that the likelihood method separates more efficiently signal from background, there is no need for tight cuts. However, in order to speed up the calculation it is still useful to reject a large fraction of mis-reconstructed down-going events.

The cut parameters are similar to those from the binned method, however no cuts based on MPE reconstructions were used for the unbinned event sample and no declination dependence was introduced. An *or* condition between NDirC and RLogL is used in order to keep bad NDirC events, if their RLogL is good. The aim of these cuts is to preserve mainly the high energy events toward the horizon, that otherwise would have been cut out. Details about the selection can be found in [A$^+$09b].

ICECUBE 22-string Southern sky

The Southern sky event sample was optimized for a binned method at ultra high energies. Therefore it should be noted that the unbinned method results could still be better in the Southern sky.

A 2-dimensional cut on the number of hits per channel is parametrized as a function of zenith (MPE-reconstruction) and estimated energy (mue) and applied to the Southern sky in order to reduce the overwhelming number of background events, rejecting the lower energy tracks. The final optimization of this sample was done in a similar manner as that described in the beginning of this section. The cuts are also zenith-wise and include similar variables (e.g. BayeRatio, NHits/NCh, NCh, RLogL, ParabSigma, NDirE). Details about the selection can be found in [A$^+$09a].

7.5.2. ICECUBE 40-string unbinned untriggered flare search event sample

Similar cut variables as for IC22 data were used to select a point source event sample for IC40. The initial selection at Level2 was introduced in Sec. 7.2. Different strengths of the same cuts were tested in order to obtain a higher detection probability. The idea behind applying looser cuts for time variable analyses was that the background is already reduced by looking at smaller time scales, therefore the signal to background ratio can be still favorable if more background events are allowed to pass the cuts than signal events. However, the different tries resulted in a relatively bigger gain in background than signal. The gain in signal was not enough to compensate the bigger background and therefore the detection probability was lower. Thus it was decided to use the time-integrated point source event sample obtained in [D$^+$09], which was deemed already suitable for time variable searches. This event sample has a unified selection criteria for the whole sky in the context of an unbinned likelihood method.

There are two main sets of cuts. The first combination of cuts improves the angular resolution, rejects badly reconstructed events and reaches an atmospheric neutrino

level in the Northern sky. The second set of cuts reduces the background of atmospheric muons in the Southern sky as a function of energy (mue estimator) and zenith (from the MPE reconstruction), in a similar way as it was done for IC22. These cuts are summarized in App. B.2.

7.6. Final event sample description

The main characteristics of the four final samples used for the two different analyses are presented in this section by showing their key parameters distributions, angular resolution, energy containment, signal efficiency, data/simulation comparison and effective area. Emphasis is given to the time-integrated IC22 binned sample and to the IC40 sample.

7.6.1. Time integrated search event sample

The IC22 Northern sky binned sample consists of 2956 events (2568 strictly below the horizon), from May 31st 2007 to April 5th 2008, comprising 275.9 days of uptime. It covers a declination range from -10° to 90°. The signal main energy region, for an E^{-2} spectrum, goes from 4.7 TeV to 3.7 PeV. The atmospheric neutrino content of the sample is greater than 90%, where the contamination comes from misreconstructed down-going muons, mostly time-coincident multiple events. From simulation, a sky-averaged median angular resolution of 1.3° is estimated for signal neutrinos with E^{-2} energy spectrum.

In Fig. 7.6 the zenith ($-\cos(\theta)$, where $-\cos(\theta) = 1$ points to the North), azimuth and energy distributions are shown. The distribution is rather uniform with a peak above the horizon (around 80° in zenith) suggesting the start of a large atmospheric muon contamination. The azimuth distribution reveals two pronounced bumps corresponding to the mayor axis of the IC22 geometry (see Sec. 7.6.2 for more details). The energy distribution is shown using *mue* (see Sec. 5.2.5) as energy estimator.

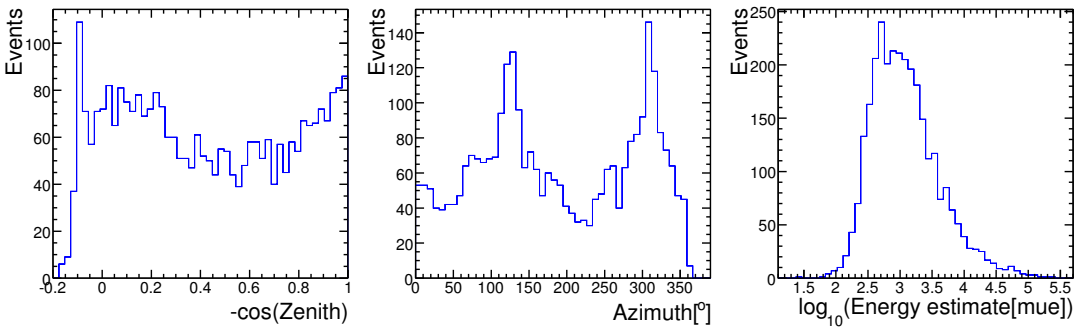

Figure 7.6.: Zenith, azimuth and energy distributions of the IC22 sample.

Angular resolution

The point spread function (PSF) is defined as the cumulative function of the space angle difference between the reconstructed track (i.e. MPE reconstruction) and the simulated

one. It is shown in Fig. 7.7a for two possible neutrino signal energy spectra. It is slightly worse for E^{-3} because the lower energy events have a less accurate direction reconstruction, given that they have shorter tracks (lower lever arm) and less hits (less information to constrain the fit). The median angular resolution corresponds to 50% of the PSF. For IC22 the obtained mean angular resolution is 1.3° for $E^{X}-2$ and 1.4° for E^{-3}. The spread of the individual reconstructed coordinates (zenith, azimuth) is presented in Fig. 7.7b. The azimuth dispersion is broader than the zenith error, because of the difference in vertical (17 m) and horizontal (125 m) spacing in IceCube.

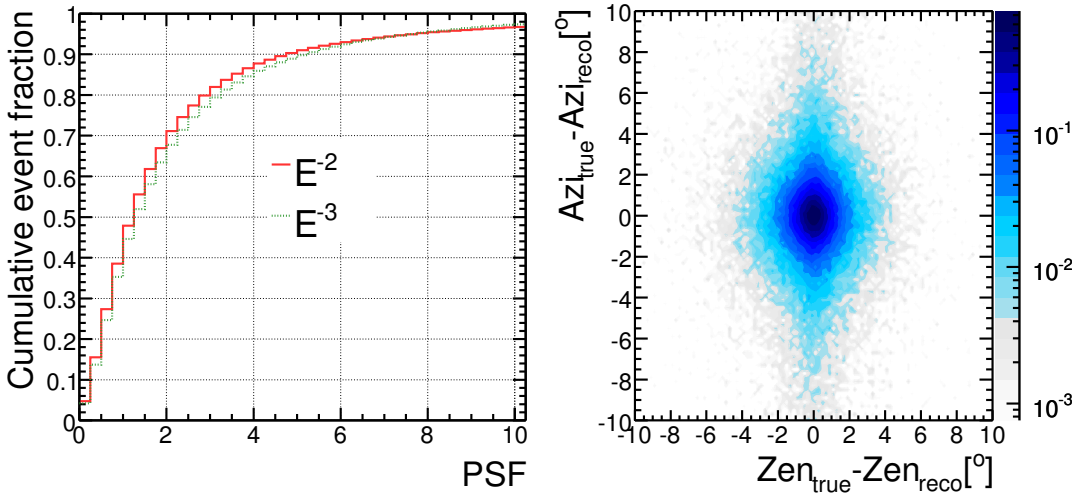

(a) Cumulative distribution of angular error

(b) Point Spread Function

Figure 7.7.: Point Spread Function for IC22.

Since the analyses presented here are focused on point sources, the mean angular resolution ($\Delta\Psi$) plays a key role. Therefore it is further investigated in Fig. 7.8 as a function of different parameters: declination, azimuth, energy and center of gravity (COG) in the Z coordinate (detector depth, $Z = 0$ is located at the center of the detector). Two different track reconstructions are shown (SPE and MPE) in order to emphasize the improvement of MPE, which is the reconstruction used in this work for the final direction of the events. The MPE reconstruction improves, on average, the median angular resolution by almost 20% at final level compared to SPE, with a higher impact at higher energies. In terms of sensitivity this results in an enhancement of ∼15%, since the search bin can then be shorten, decreasing the background while keeping the same amount of signal.

The improvement of MPE over SPE as a function of energy starts to manifest itself at 10 TeV, below this energy both reconstructions give similar results. The MPE reconstruction slightly improves with increasing energy, while for SPE it increasingly worsens. The improvement of MPE with respect to SPE for energies greater than 10 PeV can be as much as 50%. Nevertheless, the improvement at atmospheric muon level (Level2) is not significant because there are still more low energy events. The better performance of MPE at higher energies comes from the fact that it includes information on the total charge, which is not done in the SPE reconstruction.

The angular resolution as a function of declination is rather constant (see Fig. 7.8).

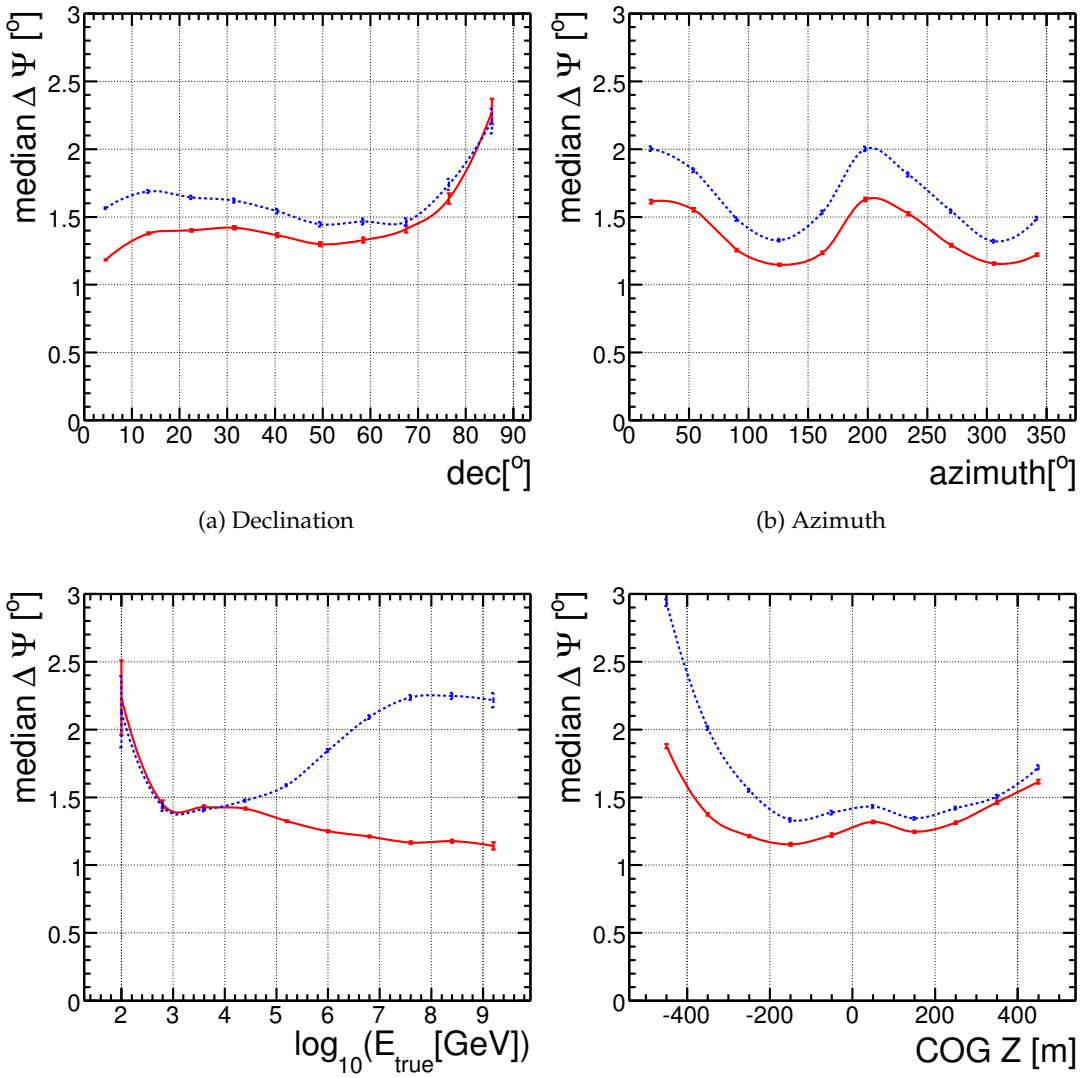

(a) Declination

(b) Azimuth

(c) Energy

(d) COGZ

Figure 7.8.: Angular resolution as a function of zenith, azimuth, energy and COGZ (depth center of gravity) for IC22 (solid red: MPE reconstruction, dashed blue: SPE reconstruction). A E^{-2} signal energy spectrum is used.

However, for almost vertical events it worsens, due to the uncertainty in azimuth (axis of symmetry). In this region both reconstructions converge because mostly low energy events are involved. The angular resolution distribution in azimuth shows the inverse pattern as the simple azimuth distribution (Fig. 7.6) evidencing the correlation between good angular resolution and more reconstructed events in the mayor axis of the IC22 geometry. Finally the COGZ distribution reveals a worsening of the reconstruction for deep events where the clear ice is located, because the parametrization of the photon arrival time distribution does not include the dust layer description of the ice. More photons can be registered in the clear ice, thus the MPE reconstruction performs better than the SPE reconstruction in this region.

Energy range

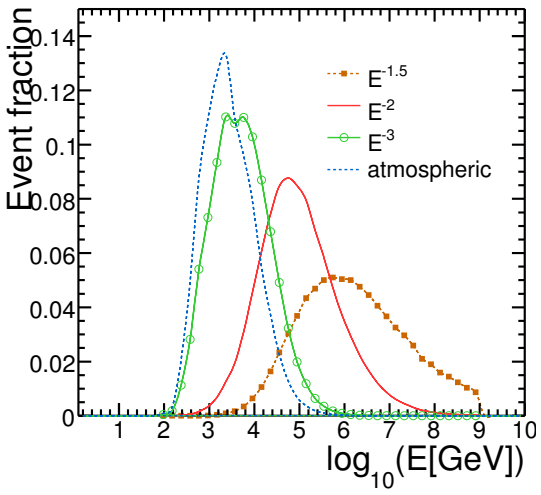

Figure 7.9.: IC22 final sample energy distribution ($\theta > 90°$) of neutrino signal simulation for different energy spectra and atmospheric neutrino simulation.

As a result of the detector spacing, neutrino absorption and interaction in Earth and the applied cuts, there are certain favored neutrino energy ranges. The energy distribution calculated at final level from signal neutrino simulation ($\theta > 90°$) for different spectral weights is presented in Fig. 7.9 and the 90% energy containment is given here:

- $E^{-1.5}$: 28 TeV - 204 PeV,
- E^{-2}: 4.7 TeV - 3.7 PeV,
- E^{-3}: 0.5 TeV - 68 TeV,
- Atmospheric: 0.37 TeV - 30 TeV.

Note that the E^{-3} signal practically overlaps with the atmospheric neutrino spectrum ($E^{-3.7}$), which is the persistent background after cuts, thus reducing the power of distinguishing the signal from background by using the energy.

Signal Efficiency

In order to quantify the impact of the cuts in the neutrino signal, the efficiency (given as the fraction of events left after applying cuts with respect to Level2) is calculated as a function of true zenith and energy (from simulation) and presented in Fig. 7.10. The efficiency as a function of zenith is rather constant, with an average of 33.3% for $\theta > 90^\circ$ and a E^{-2} signal. However, for a E^{-3} signal the efficiency is reduced to 11.4%. This behavior is evident once the efficiency with respect to energy is regarded. This distribution shows a strong suppression of events with less than 10 TeV. For events with energies above 100 TeV the efficiency is comparatively constant.

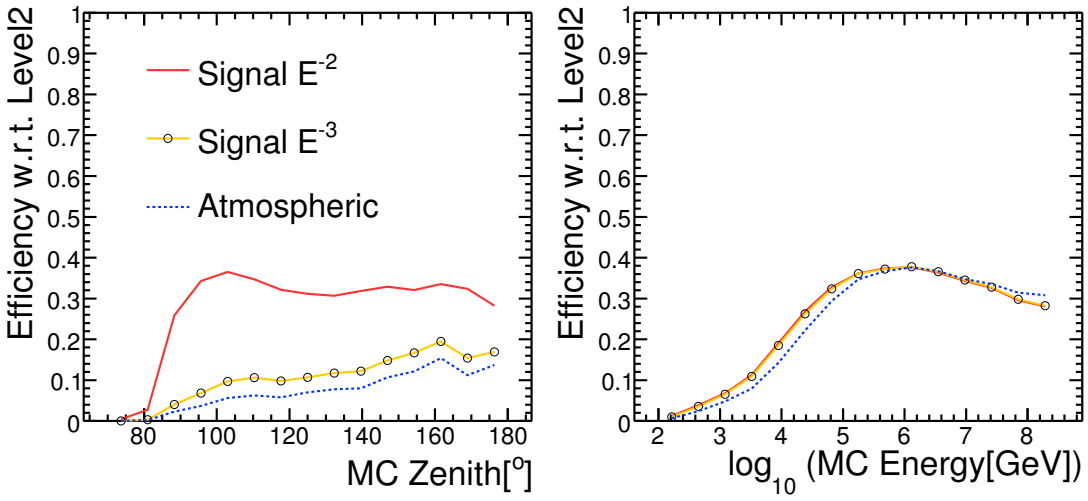

(a) Zenith dependence

(b) Energy dependence

Figure 7.10.: Signal efficiency versus zenith and energy for IC22.

Data/Simulation comparison

Even though the background is directly measured from data themselves, it is necessary for systematic error checks to compare the data with the expected background from simulation. In such manner a good understanding of the detector is achieved.

The data/simulation agreement from Level4 to final level is examined in Fig. 7.11a by increasing cuts. At Level4 the sample is still dominated by atmospheric muons, which are separated in the simulation into single muons and coincident muons (doublets), therefore they should be added up to match the data. The number of surviving events matches quite well as the zenith-dependent cuts from final level are progressively applied. The horizontal axis, *cut strength*, represents the fraction of values of the final applied cuts (cut strength=1 corresponds to the final cuts). At 90% of the cuts the lack of background simulation becomes evident. The transition from an atmospheric muon dominated sample to an atmospheric neutrino sample is achieved at the full strength of the cuts, where the data approaches the atmospheric neutrino simulation.

It is interesting to compare the final sample with the atmospheric simulation for several parameters. The atmospheric neutrino content of the sample is estimated to be

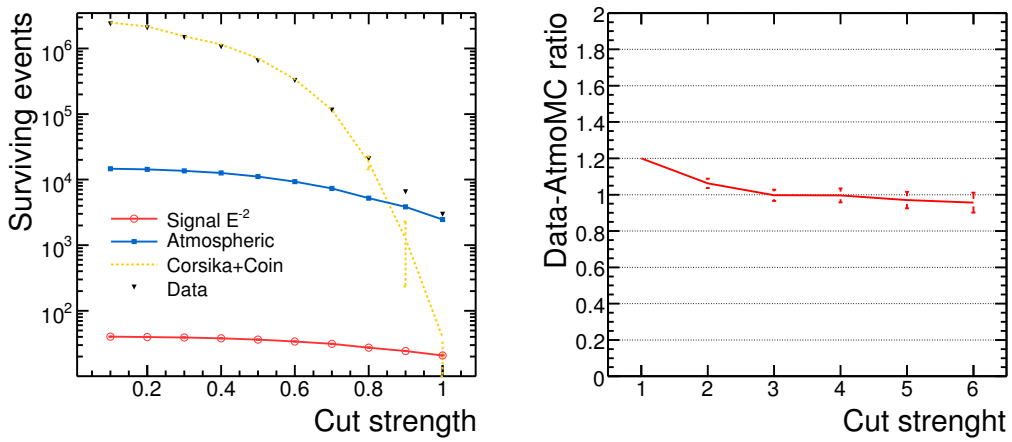

(a) Total events agreement

(b) Data-MonteCarlo normalization

Figure 7.11.: Left: Number of surviving events after increasing the strength of the combined cuts from level4 to final level for background and signal in IC22. The horizontal axis corresponds to fraction of the total combined cuts applied. Right: Data-MonteCarlo normalization. Point 1 corresponds to the cut strength chosen for this analysis.

90%, obtained from the ratio of atmospheric neutrino events, calculated from simulation, to the total number of data events. The remaining 10% is expected to be composed of mis-reconstructed down-going atmospheric-muon events. Therefore a full agreement in the parameter distribution between data and atmospheric neutrino simulation is not expected. In addition, there are uncertainties in the theoretical predictions at the level of 7-25% depending on the energy. Various reconstruction parameters are compared for data and atmospheric neutrino simulation in Fig. 7.12. It is observed that up to $\theta = 110^\circ$ there are more data events than predicted atmospheric neutrinos. This difference is assumed to be generated mostly by coincident muon events and to a lesser extend by misreconstructed down-going muons. Another clear disagreement is noticed for the COGZ distribution for deep events in the clear ice.

In order to select a virtually pure atmospheric neutrino sample, a stronger zenith cut is applied at $\theta > 115^\circ$. The results, presented in Fig. 7.13, show a better agreement between data and simulation. Nevertheless, the COGZ discrepancy does not vanish completely, which is a hint that the ice properties are not well understood. The other parameters show a reasonable agreement within the statistical errors of data and the average 15% theoretical uncertainty in the atmospheric muon flux.

An alternative way to estimate the agreement between data and atmospheric neutrino simulation is by further tightening the cuts, under the assumption that they can deliver a neutrino pure sample. Atmospheric muons are expected to have been absorbed while penetrating Earth, because the Earth's diameter is much larger than the attenuation length of a high energy muon. Then, if the cuts were 100% efficient, a pure atmospheric neutrino sample could be obtained. Nevertheless, the cuts might saturate and a residual contamination could still be present. If the zenith distributions agree after tighter cuts (see Fig. 7.13), it is an indication that a real atmospheric neutrino sample has been reached, since it is unlikely that mis-reconstructed events would mimic

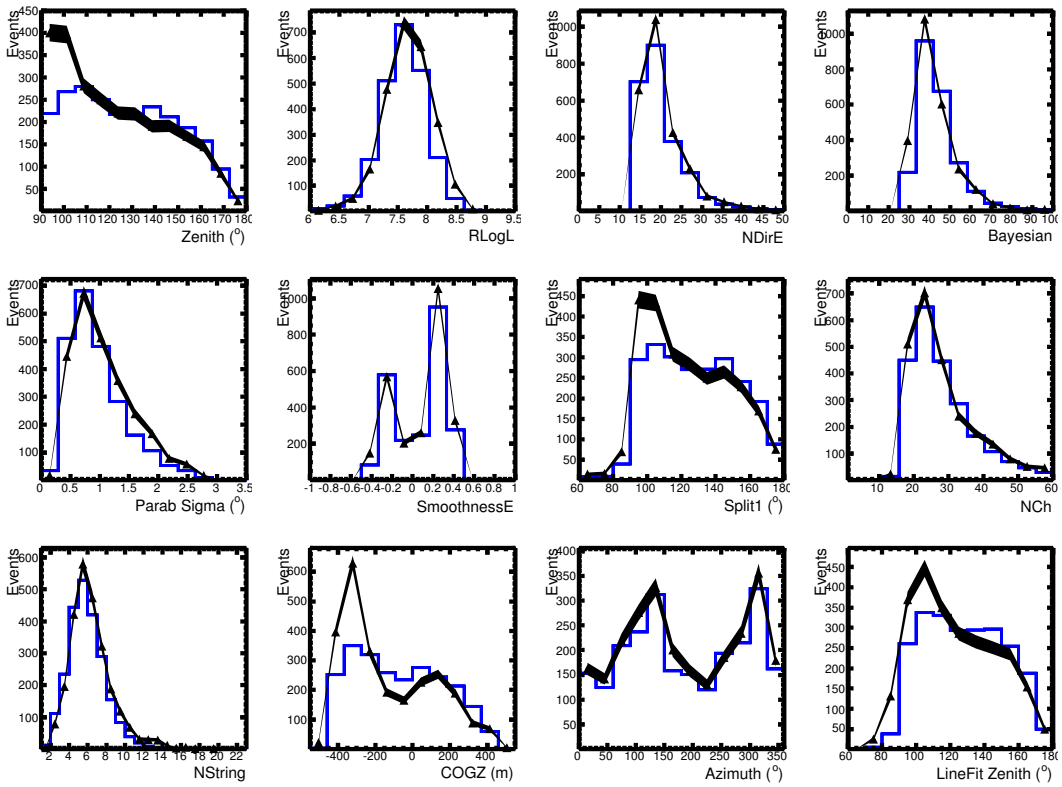

Figure 7.12.: IC22 data sample and atmospheric neutrino comparison with $\theta > 90°$. The black triangles show the data, the shadowed area represents the statistical error. The blue histogram corresponds to the atmospheric simulation. The parameters shown are: MPE zenith angle (Zenith), reduced log likelihood (RLogL), number of direct hits (NDirE), Bayesian ratio (Bayesian), angular error estimate (Parab sigma), SmoothnessE, zenith angle from time split reconstruction (Split1), number of channels (NCh), number of strings (NString), center of gravity in depth (COGZ), MPE azimuth angle (Azimuth), Line-Fit zenith angle (LineFit Zenith).

the atmospheric neutrino zenith distribution.

When tighter cuts are applied (see Fig. 7.11b), the number of data events matches, within the errors, the estimate from atmospheric simulation (i.e. ratio equal to 1). The strength of the cut's values (for NDirE and Bayesian ratio) is increased by 10% in each step starting with the cuts of this analysis. The fact that the ratio tends to converge to 1 for tighter cuts suggests that the disagreement between data and atmospheric MC, seen in Fig. 7.12, is due to a residual component of misreconstructed coincident events or atmospheric muons.

Effective Area

The neutrino effective area, $A_{\text{eff}}^{\nu+\bar{\nu}}$, can be defined in a slightly different way than in Eq. 3.1 in order to include not only the detector efficiency but also the neutrino interactions, absorption in Earth and event selection. Then a new definition is given by:

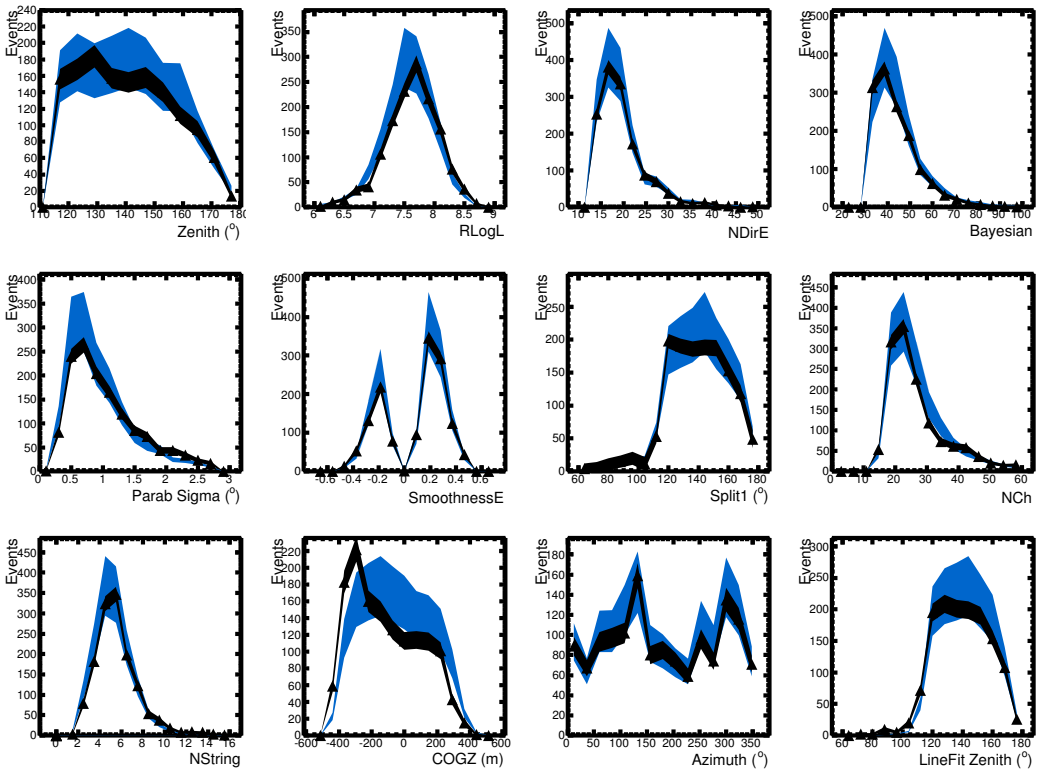

Figure 7.13.: IC22 data and atmospheric neutrino simulation comparison for $\theta > 115°$. The statistical uncertainties on data and the theoretical uncertainties on the atmospheric flux predictions are shown by the shadowed areas (black area and triangles: data, blue area: atmospheric simulation).

$$dR_{\nu+\bar{\nu}}(\delta) = A_{\text{eff}}^{\nu+\bar{\nu}}(E,\delta)\frac{d\Phi_{\nu+\bar{\nu}}}{dE}dE \ , \tag{7.6}$$

where $R_{\nu_+\bar{\nu}}$ is the number of detected neutrino-induced events and $\Phi_{\nu_+\bar{\nu}}$ is the original neutrino flux. The effective area depends on the neutrino energy and the declination because of the energy dependence of the neutrino-nucleon cross section, muon range and the declination-dependent matter distribution around the detector and related cuts. The effective area can be used to calculate the event rate for different flux predictions and to compare different experiments.

The effective area for a $\nu_\mu + \bar{\nu}_\mu$ flux, after final cuts, is presented in Fig. 7.14 including the bin efficiency. The bin efficiency accounts for the signal events which have true angular error greater than the bin size. The effective area is plotted for different declination ranges and for the whole Northern sky at Level2. The effect of the absorption in Earth, due to the increased cross section with energy, can be seen for events at large declination, where mainly lower energy events are detected. The low energy threshold at a few 10^2 GeV is caused by the broader spacing of the DOMs and the selection cuts, which is evident when the curve corresponding to Level2 and final level are compared.

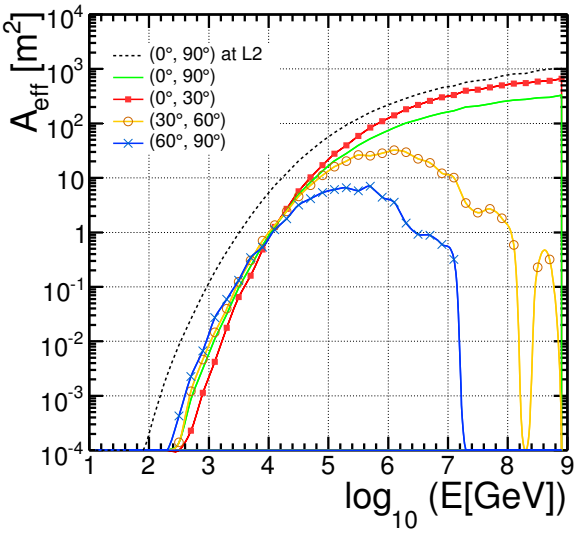

Figure 7.14.: IC22 effective area with bin efficiency for different declination ranges.

7.6.2. Time dependent search event samples

IceCube 22-string unbinned time-dependent search event sample

The data used for the IC22 unbinned time-dependent search consists of two different event samples (Northern [A$^+$09b] and Southern [A$^+$09a] skies) with particular selection criteria described in Sec. 7.5.1. Both event samples include IC22 data from May 31st 2007 to April 5th 2008, comprising 275.9 days of uptime.

The Northern sky unbinned sample consists of 5114 events, covering a declination range from $-5°$ to $85°$. The signal main energy region, for an E^{-2} spectrum, goes from 3 TeV to 3 PeV, similarly as for the binned event sample. The atmospheric neutrino content is also larger than 90%. A sky-averaged median angular resolution of $1.4°$ is obtained for an E^{-2} signal.

The Southern sky binned sample is a subset (declination $< 0°$) of the dedicated ultra high energy sample which covers a declination range from $-50°$ to $85°$ and has a total of 1877 events. Its sky-averaged median angular resolution is $1.3°$ for an E^{-2} signal. The energy containment ranges from $10^{4.7}$ to $10^{8.1}$ GeV for the same spectrum (for an $E^{-1.5}$ signal: from $10^{5.8}$ to $10^{9.1}$ GeV). The data distributions used as background have been shown in Fig. 6.3 (zenith-azimuth) and Fig. 6.4 (zenith-energy).

IceCube 40-string unbinned time-dependent search event sample

The IC40 all-sky unbinned event sample [D$^+$09] collects data from April 5th 2008 to May 20th 2009. It spans 410 days with an overall effective detector uptime of $\sim$ 92% (i.e. 375.5 days). The whole sky (declination range from -85° to 85°) is scanned. A unified zenith-dependent selection criteria was applied (see Sec. 7.5.2).

It was found that even though this was optimized for a time-integrated analysis, it is also suitable a for time-dependent analysis. In the Northern sky a 90% pure sample of neutrino-induced muons is obtained, while in the Southern sky the event sample consists mainly of high energy atmospheric muons.

After selection cuts 37290 events remain (14139 up-going, 23151 down-going), with a median angular resolution of 0.6° in the Southern sky and 0.8° in the Northern sky. The energy containment in the two regions of the sky is different, for an E^{-2} signal spectrum it ranges from $10^{4.1}$ to $10^{7.7}$ GeV and from $10^{3.4}$ to $10^{6.4}$ GeV, in the Southern and Northern skies, respectively. Event tracks are obtained with the MPE reconstruction.

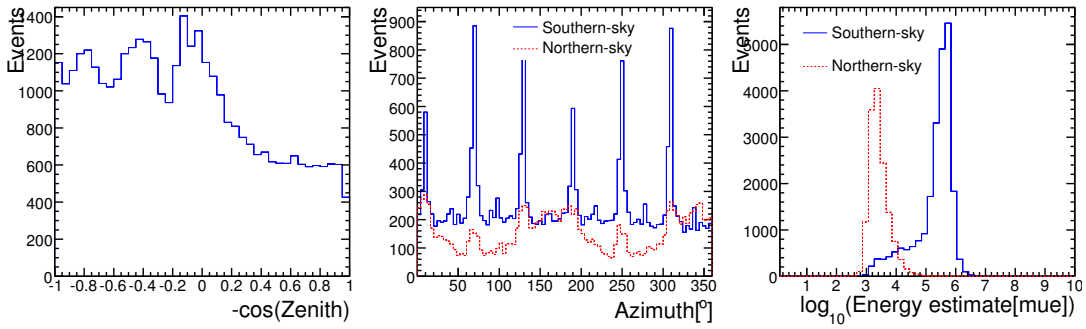

Figure 7.15.: Zenith, azimuth and energy distribution of the IC40 sample.

Fig. 7.15 shows the IC40 zenith, azimuth and energy distributions. The structure observed in the Southern sky for the zenith distribution is caused by the step-wise cuts applied at Level2. The energy distribution is clearly separated into two regions as an effect of the selection cuts, which correspond to the Northern (lower energies) and Southern skies (higher energies). There is a small overlap region around the horizon.

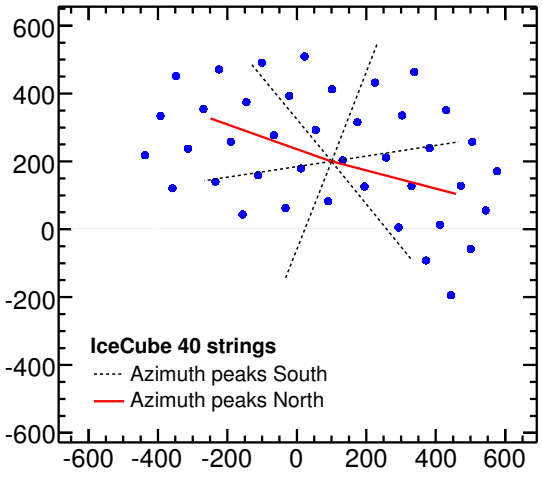

Figure 7.16.: IC40 geometry and axes corresponding to the center of the peaks in azimuth distribution.

The azimuth distribution shows two pronounced bumps for the Northern sky for events aligned along the mayor axis of the IC40 geometry, because they present a longer lever arm and are thus more likely to trigger the detector and be well-reconstructed. For the Southern sky (higher energies) there are 6 distinct peaks, coinciding with the three positions where the strings are aligned. This characteristic is due to the

fact that there is an initial cut on the integrated charge from all DOMs in the filtering for the Southern sky, giving a preference to events which pass near to a line of strings. All these directions are depicted in Fig. 7.16, where the axes corresponding to the peaks are drawn on top of the IC40 geometry.

Angular resolution

The angular resolution of IC40 represents an improvement of $\sim$ 40% over IC22. In Fig. 7.17 the mean angular resolution is shown as a function of zenith, azimuth, energy and COGZ. Since zenith and energy are correlated because of the selection cuts, the angular resolution of both variables is also correlated. Events with higher energies are better reconstructed, thus smaller declinations have better angular resolution, since the highest energy events are contained in the Southern sky. The enhancement of the angular resolution with increasing energy is more pronounced than in IC22, with difference of more than 3 times between the lowest and highest energy events. The angular resolution valleys in azimuth are once more aligned with the mayor axis, in this case of IC40, evidencing the correlation between good angular resolution and more reconstructed events (c.f. Fig. 7.15). The angular resolution with respect to COGZ has flattened compared to IC22.

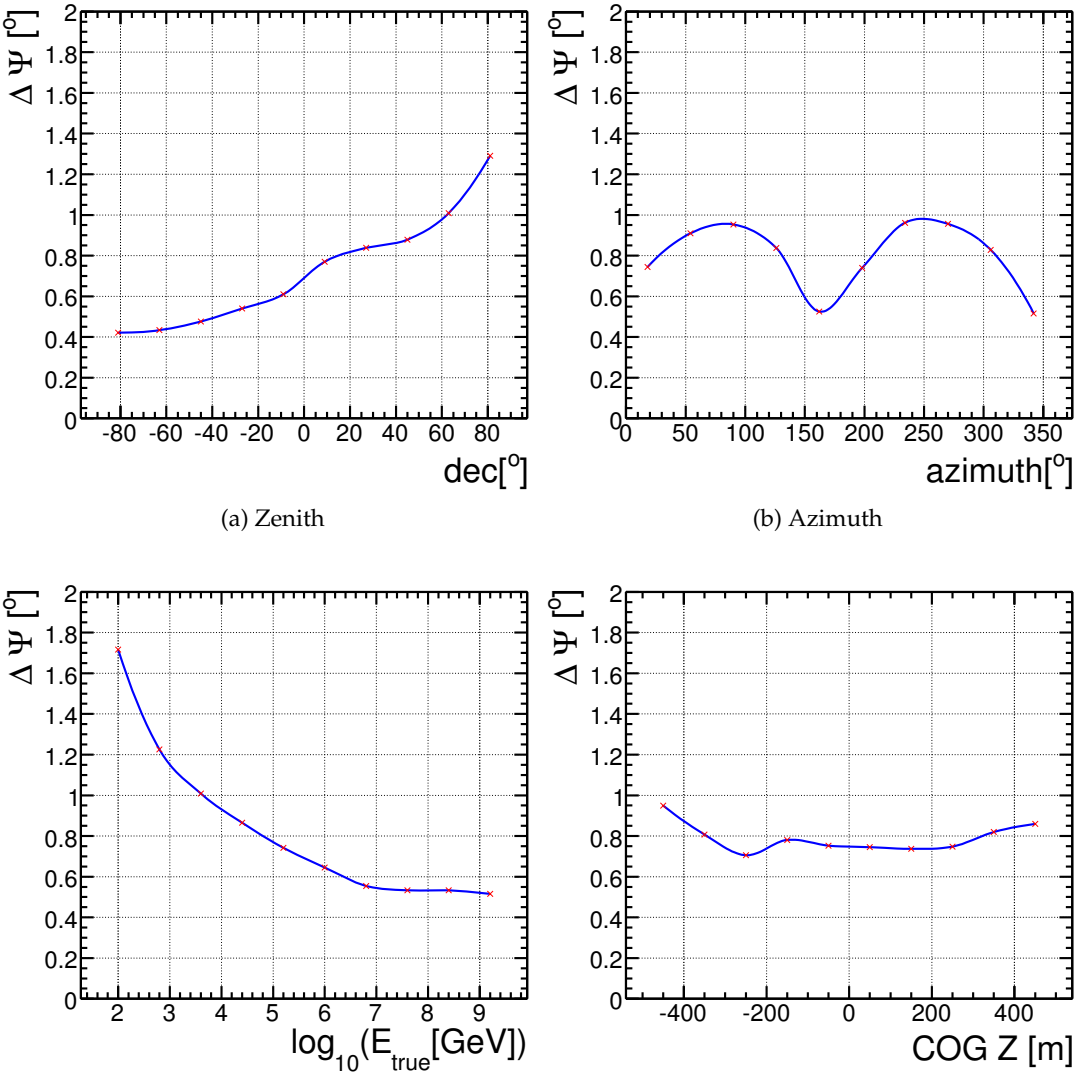

(a) Zenith

(b) Azimuth

(c) Energy

(d) COG Z

Figure 7.17.: Angular resolution as a function of zenith, azimuth, energy and COGZ for IC40, using the MPE reconstruction. A E^{-2} signal energy spectrum is used.

8. Source candidate selection

> Man konnte die Probleme nicht nur durch Nachdenken lösen, jemand musste durch ein Okular starren, bis ihm die Augen weh taten, und ein anderer musste die Messergebnisse in ermüdend langen Tabellen festhalten.
>
> Daniel Kehlmann 1975
> *Die Vermessung der Welt*

Searching for astrophysical neutrinos in all sky directions decreases the significance of a positive fluctuation, because of the increased number of trials. It is desirable to select only a few promising sources, thus reducing the number of trials. In this chapter the source selection criteria for the 3 analyses is presented with emphasis on the variable sources.

8.1. Time integrated search source list

The source selection is motivated by different models and assumptions, however, the final choice has also a subjective component, since no point source of neutrinos has been observed yet. Different lists have been used since the times of AMANDA and they have been continuously updated with recent observations and data from new experiments. The candidate list presented in this section corresponds to the time-integrated search at the time of the ICECUBE 22-string configuration.

The sources should be capable in the first place of accelerating protons to the highest necessary energies for hadronic production. This is a two-fold requirement between the magnetic field and the size of the accelerating region according to the Hillas criterion [Hil84]:

$$B_{\mu G} L_{pc} > 2 E_{15} Z \beta \ , \tag{8.1}$$

where $B_{\mu G}$ is the component of the magnetic field normal to the particle's velocity in microgauss, L_{pc} is the size of the accelerating region containing the field in units of parsec, E_{15} is the particle's energy in units of 10^{15}eV, Z is the charge of the particle and βc is its characteristic velocity. Active Galactic Nuclei are good candidates following this criterion.

The most natural way to select point sources a-priori without depending on neutrino observations, is to use photon observations, since photons will also not be deviated by magnetic fields in their way towards Earth. This argument is based on the $\gamma - \nu$ connection [Der06] (see also Eq. 2.3). Photohadronic models of astrophysical sources produce γ-rays and neutrinos alike. Therefore identifying bright TeV-γ-ray sources would mean that they should also produce neutrinos. Nevertheless, this logic is not completely correct. First of all, the γ-rays could have been caused by leptonic processes. Secondly, the γ-rays could have been attenuated (absorbed in the source's

opaque medium or extragalactic background light) making the sources less photon bright but still having produced neutrinos.

Since astrophysical neutrino observations are not background free, due to the persistent background of atmospheric neutrinos, a lower threshold on the neutrino flux that can be observed in ICECUBE can be set. This neutrino flux threshold can be translated into a photon flux, which would then be used to restrict the number of sources. Supposing a neutrino fluence $F_\nu \sim 10^{-4}$ erg cm^{-2} in the energy range from 10 TeV to 1 PeV, then the photon fluence should be $F_\gamma \gg 10^{-4}$ erg cm^{-2} [Der06]. If EGRET[1] (Energetic Gamma Ray Experiment Telescope) observations are used, the necessary photon flux can be calculated to be $\Phi_\gamma(> 100 \text{ MeV}) \gg 30 \times 10^{-8}$ phcm^{-2}s^{-1} [Der06]. However, this is no guarantee of a neutrino flux. Nevertheless, the sensitivity energy range of EGRET and Fermi[2] ($E_\gamma \approx 100$ MeV - 10 GeV), coincides with the energy region where photon attenuation by the extragalactic background light is negligible. Therefore, the most powerful objects observed by these experiments are very interesting.

In addition, observations by TeV γ-ray experiments (e.g. MAGIC, HESS, Milagro, VERITAS), but also from X-ray, radio and optical telescopes are taken into account (e.g. spectral shape, normalization and cut-off energy). Ultra high energy cosmic rays (e.g. protons) could be used to loosely point back to their sources, because at energies above tens of EeV, they are less deflected by magnetic fields (in the order of a few degrees). This approach is applied in [Lau10] with a high energy neutrino sample.

Since ICECUBE has a higher sensitivity in the TeV-PeV region in the Northern sky (dec$> 0^o$), only sources in this hemisphere were selected for the present candidate source list. However, also objects in the Southern sky can be included, but with a sensitivity at higher energies. These sources were included for the time variable searches, since at the time these analyses were developed an event sample selection for the Southern sky was available [A$^+$09a].

Finally a candidate source list of 28 astrophysical objects [M$^+$08] has been selected following the guidelines described above. The list covers 12 galactic and 16 extragalactic sources, including 3 supernova remnants, 6 X-ray binaries, 10 blazars, 3 quasars and 2 radio galaxies. The names, coordinates and types of the sources are summarized in Table 8.1.

Table 8.1.: Time-integrated candidate source list for IC22.

Name	**Dec (^{o})**	**RA(^{o})**	**Type**
Galactic sources			
MGRO J2019+37	36.83	304.83	
MGRO J1908+06	6.28	287.27	SNR
TeV J2032+4130	41.51	308.08	
SS 433	4.98	287.96	HMXB mqso
Cyg X-1	35.20	299.59	HMXB

[1] EGRET was a γ-ray space telescope, installed on NASA's Compton Gamma Ray Observatory satellite. Its energy range covered from 30 MeV to 30 GeV and was taking data from 1991 to 2000.

[2] Fermi is a γ-ray space telescope in a low Earth orbit. It was formerly known as GLAST (Gamma-ray Large Area Space Telescope). It was launched on 11 June 2008. The instrument inside Fermi, from which data for this analysis are used, is called Large Area Telescope (LAT). The LAT performs an all-sky survey studying diverse astrophysical phenomena in the energy range from 20 MeV to more than 300 GeV.

Table 8.1 – continued from previous page

Name	Dec (^{o})	RA(^{o})	Type
LS I +61 303	61.23	40.13	HMXB mqso
GRS 1915+105	10.95	288.80	LMXB
XTE J1118+480	48.04	169.54	LMXB
GRO J0422+32	32.91	65.43	LMXB
Geminga	17.77	98.48	Pulsar
Crab Nebula	22.01	83.63	SNR/PWN
Cas A	58.81	350.85	SNR
Extragalactic sources			
Mrk 421	38.21	166.11	HBL
Mrk 501	39.76	253.47	HBL
1ES 1959+650	65.15	300.00	HBL
1ES 2344+514	51.70	356.77	HBL
H 1426+428	42.67	217.14	HBL
1ES 0229+200	20.29	38.20	HBL
BL Lac	42.28	330.68	LBL
S5 0716+71	71.34	10.47	LBL
3C66A	43.03	35.66	LBL
3C 454.3	16.15	343.49	FSRQ
4C 38.41	38.13	248.81	QSO
PKS 0528+134	13.53	82.73	QSO
3C 273	2.05	187.28	QSO
M87	12.39	187.71	Misaligned BL Lac
NGC 1275	41.51	49.95	Seyfert Galaxy
Cyg A	40.73	299.87	RLG

Note.- Name (name of the source), Dec (declination in degrees), RA (right ascension in degrees). Types: SNR (supernova remnant), mqso (microquasar), HMXB/LMXB (high/low-mass X-ray binary), PWN (Pulsar wind nebula), HBL/LBL (high/low frequency peaked Blazars), QSO (quasi-stellar object) and RLG (radio-loud galaxy).

8.2. Time dependent search source lists

In a time dependent analysis an additional property of the sources is taken into account, namely, the time variability. An analysis of a source with a steady neutrino flux would not profit from a time dependent search, thus only time variable sources should be selected. Using the neutrino-photon expected correlation from hadronic models, γ-ray data can be used to select sources that show high photon flaring states, which would imply neutrino flares. The most promising type of source with prominent photon flares are blazars (see Sec. 2.2.2), which could also produce neutrinos. The photon variability of blazars is further discussed in this section, since it motivates their selection.

Among AGNs, blazars show the most extreme photon flux variability at all wavelengths. They are only surpassed by GRBs, which present extremely rapid explosions.

The variability time-scale of blazars ranges from fast flares of few minutes, to hours and high states of several days. This variability implies a very compact emission region. However, not only blazars have been observed to be variable, other sources include radio galaxies and X-ray binaries. In addition, the intensities during these flares are frequently many times larger than the usual photon flux in the normal state. The vast majority of these flares are not predictable, with a few exceptions of periodic sources. In hadronic models of AGNs [Aha00, BMB09], these flares arise from photo-hadronic and proton-proton interactions (see Sec. 2.4), which also lead to the coincident production of neutrinos.

Blazars, as many other possible astrophysical neutrino sources, present two broad spectral photon components, one at low energies (IR to soft X-rays) and another at very high energies (GeV to TeV γ-rays) [U$^+$97]. In the lower energy component two regions with different behaviors can be differentiated. Below the peak energy the variability amplitude is small, while above the peak the variability is much more pronounced increasing with energy. The high-energy component also varies more, showing a harder spectrum with increasing energy above its peak [U$^+$97].

Simultaneous observations of a broad range of wavelengths suggest that the variability amplitude of both components (e.g. γ-rays and X-rays) is correlated. Time lags of hours to days have been registered between optical and X-ray flares, also between optical and TeV flares. HBLs and LBLs show the same variability with respect to their own peak energies in their spectral distributions (e.g. they vary more above their respective peaks: optical and GeV for LBLs and X-rays and TeV for HBLs). Some possible explanation of the flux variability in blazars can be given by mechanisms that involve shock waves moving along the jet or the rotation of the beaming cone across the line of sight.

Even though a neutrino flare search not triggered by γ-ray flare observations is applied to the selected sources, it is still desirable to collect γ-ray information in order to choose them, given the strong motivation given above.

8.2.1. IceCube 22-string candidate list

Variable bright astrophysical sources covering the whole sky are selected. The sources were taken from the confirmed Active Galactic Nuclei (AGN) in the third EGRET catalog (3EG) [H$^+$99]. According to the AGN type classification from [N$^+$07] they are Blazars, including Flat Spectrum Radio Quasars (FSRQs) and Low-frequency peaked BL Lacs (LBLs). The criteria for selecting variable and bright source is based on the following parameters thresholds:

- EGRET variability index > 1, taken from [N$^+$03],
- maximum 3EG flux (10^{-8}ph cm^{-2}s^{-1}, E> 100 MeV) > 40,
- average 3EG flux (10^{-8}ph cm^{-2}s^{-1}, E> 100 MeV)> 15,
- present in both 3EG and Fermi [A$^+$09e] catalogs,
- inside visibility region of the IC22 sample ($\delta > -50$).

The first condition requires that the p-value for rejecting the non-variable source hypothesis is lower than 10^{-1}. The conditions related to the photon flux [Lau10] select

bright sources, which should also have a high neutrino flux, if hadronic models are valid for these sources.

The selected source list consists of 10 directions (see Table 8.2) that are tested for flares with the untriggered unbinned method. Its distribution in the sky is shown in Fig. 8.1. Models like the one described in [AD04] favor fluxes of higher energy neutrinos from FSRQ sources. Given the absorption of neutrinos at different energies in the Earth and the event cut strategy, Southern sky FSRQs are more favored by these models because of their higher energy range of sensitivity.

It is possible that by chance some GRBs directions coincide with those of the sources selected here. Since the untriggered flare search is in principle also sensitive to GRBs, the directions were confronted to the GRBs (41 North and 40 South [Rot09]) bursting during the IC22 good data taking period. No coincidence within 2 degrees of the 10 blazars directions with the GRBs locations was found.

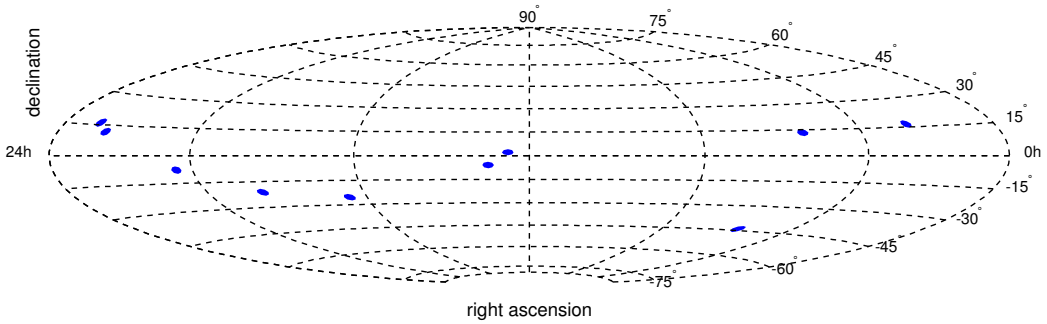

Figure 8.1.: Locations in the sky of the selected 10 sources for IC22.

8.2.2. IceCube 40-string candidate list

For IC40 variable bright astrophysical sources are also selected from the whole sky. In this case sources are only taken from the Fermi LAT Bright Source List [A$^+$09e], because the results supersede those from EGRET and the data taking period of IC40 and Fermi overlap. The sources, most of them blazars, include Flat Spectrum Radio Quasars (FSRQs) and BL Lacs, as well as, one high-mass X-ray binary and one radio galaxy. The selection criteria for choosing the sources was simplified from that of IC22 and was based on the following parameters:

- Classified as variable (variability flag=T),
- Flux [100 MeV - 1 GeV] > 1.1 [10^{-7} ph cm^{-2}s^{-1}].

The first requisite implies that the source has a 1% chance of being a steady source. The second one sets a minimum photon flux, motivated by the correlation between neutrinos and photons emitted from the source predicted by hadronic models [Aha00, BMB09]. The photon flux distribution of all Fermi variable sources is presented in Fig. 8.2, having an average flux of 2.3 $\times 10^{-7}$ ph cm^{-2}s^{-1}. The source with the largest flux is LS I+61 303. The flux threshold chosen keeps most of the well-known sources and prevents a future list, when Fermi updates its results, from arbitrarily expanding. Using all 66 variable sources from the Fermi list, would have still represented a not too

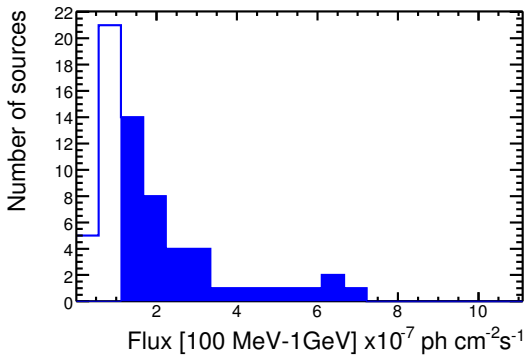

Figure 8.2.: Fermi variable sources photon flux distribution. The selected IC40 sources (above $> 1.1 \times 10^{-7}$ ph cm^{-2}s^{-1}) correspond to the shadowed area.

large trial factor, however the list was reduced to fewer more promising sources. If the expected neutrino flux for a E^{-2} source had been used to select the declination region, it would have meant to reject almost the entire Southern sky. This selection criterion was not used because it would have reduced the scope of the analysis.

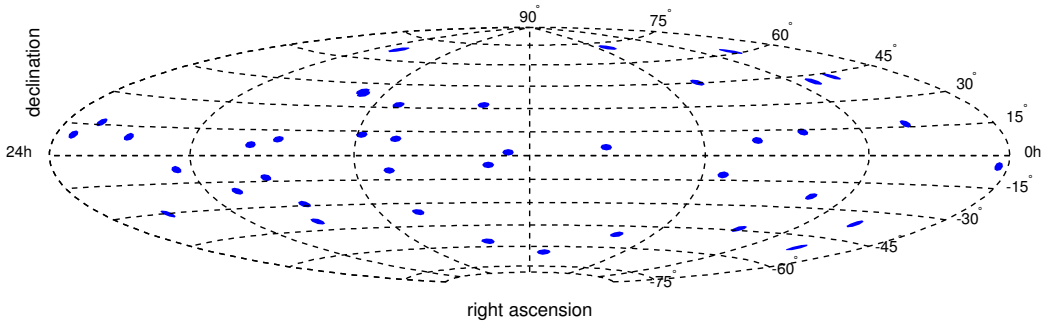

Figure 8.3.: Locations in the sky of the selected 40 sources for IC40.

The selected source list consists of 40 directions (see Table 9.3), 18 in the Southern sky and 22 in the Northern sky. The 40 selected sources distribution in the sky is shown in Fig. 8.3. From the 10 selected sources for IC22, 7 remain in the IC40 selection. The grounds for discarding the other 3 sources were that they were not seen variable by Fermi during the restricted period considered (i.e. first three months of survey data [A$^+$09e]), otherwise they would have satisfied the photon flux threshold. When newly available one-year Fermi data are taken into account, 2 out of the 3 rejected sources satisfy the variability criteria.

As for IC22, a correlation between GRB locations and the selected sources is searched for. From the 117 selected GRBs [M$^+$09a] during the IC40 period, only one falls within a 1 degree angular bin from the selected variable sources. The pair of directions correspond to GRB090301B (dec 9.5^o, ra 352.8^o) and the blazar PKS2325+093 (dec 9.794^o, ra 351.83^o).

Table 8.2.: IC22 pre-defined variable astrophysical source candidates.

Source	**3EG Name**	**Type**	**dec [°]**	**ra [°]**	**z**	**Var$_{EG}$**	**Var$_F$**	**Flux$_{max}$**	**Flux$_{min}$**	**Flux$_{avg}$**
GEV J0540-4359	3EG J0540-4402	LBL	-44.1	84.7	0.894	6.18	y	91.1	16.5	25.3
GEV J1626-2502	3EG J1626-2519	FSRQ	-25.5	246.4	0.79	2.03	n	82.5	10.1	21.3
GEV J1832-2128	3EG J1832-2110	FSRQ	-21.1	278.4	1	1.05	n	99.3	17.8	26.6
GEV J2024-0812	3EG J2025-0744	FSRQ	-7.6	306.4	1.39	3.14	y	74.5	18.8	21.2
3C 279	3EG J1255-0549	FSRQ	-5.8	194.1	0.54	>16	y	267.3	7.6	74.2
3C 273	3EG J1229+0210	FSRQ	2.0	187.3	0.16	1.56	y	48.3	8.5	15.4
CTA 102	3EG J2232+1147	FSRQ	11.7	338.1	1.04	1.22	n	51.6	12.1	19.2
GEV J0530+1340	3EG J0530+1323	FSRQ	13.5	82.7	2.06	>16	y	351.4	32.4	93.5
3C 454.3	3EG J2254+1601	FSRQ	16.1	343.5	0.86	3.93	y	116.1	24.6	53.7
GEV J0237+1648	3EG J0237+1635	LBL	16.6	39.7	0.94	5.07	y	65.1	11.6	25.9

Note.- Source types are: LBL (low-frequency peaked blazars) and FSRQ (Flat-Spectrum Radio Quasar), z is the redshift, Var$_{EG}$ is the EGRET variability index ([N^{+}03]), Var$_F$ is the variability flag from Fermi (y means variable, n steady), Flux$_{max}$, Flux$_{min}$ and Flux$_{avg}$ are the 3EG maximum, minimum and average photon fluxes with E> 100 MeV in units of 10^{-8}ph cm^{-2}s^{-1}.

9. Results

... daß der Heeresbericht sich nur auf den Satz beschränkte,
im Westen sei nichts Neues zu melden.
Erich Maria Remarque 1898-1970
Im Westen nichts Neues

In this chapter the results of the time-integrated neutrino search and the two untriggered neutrino flare searches are presented. Since no signal has been detected, limits are calculated for each source. The statistical and systematic uncertainties are discussed in the end.

9.1. Search for point sources in the Northern sky with ICECUBE 22-string

A time-integrated neutrino point source search using a binned method (see Sec. 6.2.1) was applied to IC22 data (see Sec. 7.6.1) in the Northern sky. The declination averaged sensitivity of this analysis was 2×10^{-11} TeV^{-1}cm^{-2}s^{-1}, which is 40% better than the total statistics collected with the AMANDA-II detector [A^{+}09c]. A candidate source list (see Sec. 8.1) was tested and the entire Northern sky was scanned. In neither case a source signal can be claimed since the upward fluctuations were considered compatible with background. The highest p-value came from the all-sky search. In combining both post-trial results, an additional trial factor of $\sim$2 is taken into account.

Another analysis was developed elsewhere [A^{+}09b] for the same ICECUBE configuration using an unbinned method, which proved to be 35% more sensitive. However, no signal was observed either using this method. Since the overlap between the event samples of both analyses was 72%, due to a different selection criteria, there was certain independence in the results. The most significant direction in the sky of each analysis had different sky coordinates, which can be explained given that the unbinned analysis included an energy term, which was not present in the binned analysis.

9.1.1. Candidate source list

Table 9.1 shows the individual source results including the number of observed events inside the bins, the estimated background, the p-values and the flux upper limits for two possible neutrino spectra. The limits include the statistical and systematic uncertainties (for a discussion of these errors see Sec. 9.3). The significance calculation has been done using binomial statistics (see Eq. 6.6). The column description is given next:

Name	Name of the source
Dec	Declination in degrees
RA	Right ascension in degrees
Bin_S	Radius of the search bin in degrees
N_{obs}	Number of observed events in the bin
N_{bg}	Mean number of background events in the bin
μ_{90}	Event upper limit at 90% CL from Feldman&Cousins
NsE^{-2}	Number of expected signal events for E^{-2} and $\Phi_0 = 10^{-11}$ $\text{TeV}^{-1}\text{cm}^{-2}\text{s}^{-1}$
ULE^{-2}	Flux upper limit including errors, in units of $10^{-11}\text{TeV}^{-1}\text{cm}^{-2}\text{s}^{-1}$ for E^{-2}
NsE^{-}3	Number of expected signal events for E^{-3} and $\Phi_0 = 10^{-4}$ $\text{TeV}^{-1}\text{cm}^{-2}\text{s}^{-1}$
ULE^{-3}	Flux upper limit including errors, in units of $10^{-11}\text{TeV}^{-1}\text{cm}^{-2}\text{s}^{-1}$ for E^{-3}
pvalue	Probability of obtaining a significance greater than the one observed assuming the background-only hypothesis
sigma	Significance in number of standard deviations

The maximum significance, pre-trial, found was 1.27σ (p-value=10.2%) for the Crab nebula. Using randomized simulations, the probability that the excess parameter, ξ ($\xi = -\log_{10}$[p-value]), would be greater than the largest excess parameter from all the sources in the catalogue (i.e. 28 sources) is found to be 89.9% (post-trial). If the normalized distribution of ξ for background simulations is compared to the obtained results for the list, it is seen that they are compatible within statistical errors (see Fig. 9.1a). In Fig. 9.1b the upper limits for a standard E^{-2} signal neutrino flux are shown. There are under and upward fluctuations around the sensitivity, as expected.

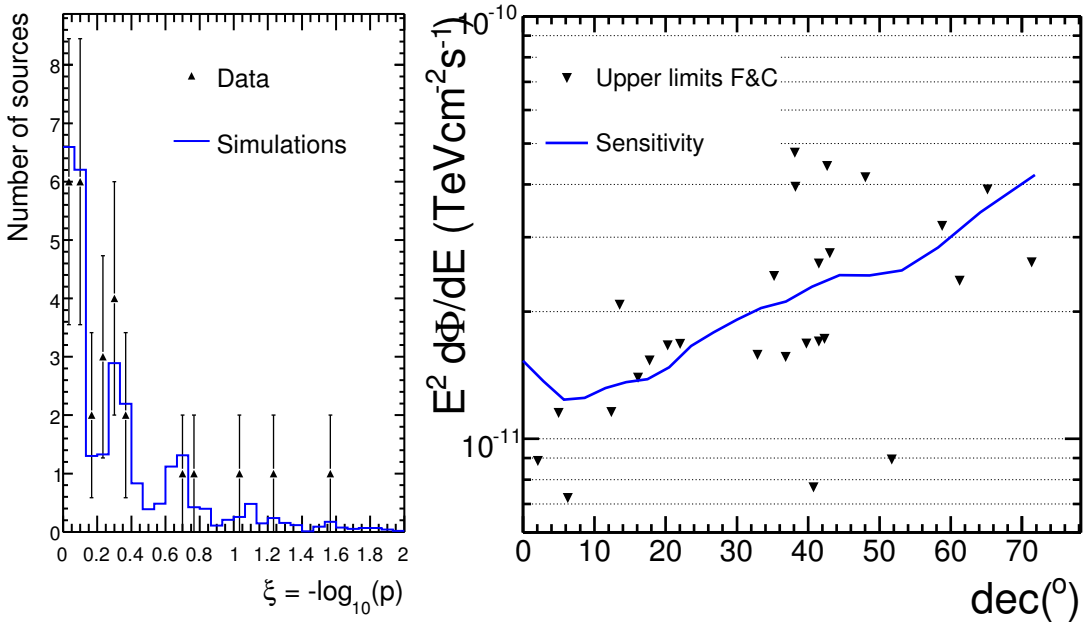

(a) Excess parameter

(b) Upper limits

Figure 9.1.: Excess parameter and upper limits distribution of the 28 IC22 sources assuming an E^{-2} energy spectrum.

Table 9.1.: Results for the *a priori* source list for IC22 (see text for label explanations).

Name	Dec (^{o})	RA(^{o})	Bins	N_{obs}	N_{bg}	μ_{90}	NsE^{-2}	ULE^{-2}	NsE^{-3}	ULE^{-3}	pvalue	sigma
MGRO J2019+37	36.83	304.8	2.21	2	1.69	4.18	1.83	2.28	1.08	38.70	0.51	0.03
MGRO J1908+06	6.28	287.3	2.17	1	2.25	2.34	3.35	0.70	0.59	39.66	0.90	1.28
TeV J2032+4130	41.51	308.1	2.18	1	1.66	2.70	1.54	1.75	1.17	23.08	0.81	0.88
SS 433	4.98	287.9	2.16	2	2.25	3.62	3.28	1.10	0.52	69.62	0.66	0.41
Cyg X-1	35.20	299.6	2.22	0	1.50	1.30	1.79	0.73	0.99	13.13	1.00	0.00
LS I +61 303	61.23	40.1	2.02	1	1.58	2.78	1.24	2.24	1.62	17.16	0.80	0.84
GRS 1915+105	10.95	288.8	2.21	4	2.32	6.82	3.12	2.19	0.74	92.16	0.20	0.84
XTE J1118+480	48.04	169.5	2.13	0	1.44	1.34	1.51	0.89	1.16	11.55	1.00	0.00
GRO J0422+32	32.91	65.4	2.23	3	1.32	6.42	1.82	3.53	0.96	66.88	0.15	1.04
Geminga	17.77	98.5	2.24	2	1.70	4.18	2.71	1.54	0.95	44.00	0.51	0.03
Crab Nebula	22.01	83.6	2.25	4	1.77	7.38	2.47	2.99	0.97	76.08	0.10	1.28
Cas A	58.81	350.9	2.04	2	1.82	4.02	1.37	2.93	1.58	25.44	0.54	0.10
Mrk 421	38.21	166.1	2.20	1	1.73	2.70	1.76	1.53	1.10	24.54	0.82	0.92
Mrk 501	39.76	253.5	2.19	2	1.61	4.34	1.64	2.65	1.11	39.09	0.48	0.05
1ES 1959+650	65.15	300.0	1.98	2	1.91	4.06	1.05	3.87	1.41	28.79	0.57	0.18
1ES 2344+514	51.70	356.8	2.10	3	1.48	6.22	1.52	4.09	1.31	47.48	0.19	0.88
H 1426+428	42.67	217.1	2.17	0	1.53	1.30	1.49	0.87	1.16	11.21	1.00	0.00
1ES 0229+200	20.29	38.2	2.25	1	1.64	2.74	2.56	1.07	0.97	28.25	0.81	0.88
BL Lac	42.28	330.7	2.17	1	1.61	2.78	1.51	1.84	1.14	24.39	0.80	0.84
S5 0716+71	71.34	10.5	1.94	2	2.09	3.78	0.95	3.98	1.54	24.55	0.62	0.31
3C66A	43.03	35.7	2.17	1	1.45	2.90	1.54	1.88	1.21	23.97	0.77	0.74
3C 454.3	16.15	343.5	2.24	4	1.95	7.26	2.81	2.58	0.95	76.42	0.13	1.13
4C 38.41	38.13	248.8	2.20	2	1.71	4.18	1.75	2.39	1.08	38.70	0.51	0.03
PKS 0528+134	13.53	82.7	2.23	0	2.33	1.26	3.00	0.42	0.87	14.48	1.00	0.00
3C 273	2.05	187.3	2.13	1	2.12	2.38	2.81	0.85	0.40	59.5	0.88	1.17
M87	12.39	187.7	2.22	2	2.33	3.50	3.09	1.13	0.83	42.17	0.68	0.47
NGC 1275	41.51	49.9	2.18	2	1.65	4.26	1.54	2.77	1.17	36.41	0.49	0.03
Cyg A	40.73	299.9	2.18	3	1.50	6.26	1.60	3.91	1.14	54.91	0.19	0.88

The significance can also be given in terms of standard deviations. In order to convert probabilities (p-values) into units of σ the following formula has been used:

$$\sigma = \text{erf}^{-1}(1 - 2 \times \text{p-value}) \times \sqrt{2} \ , \tag{9.1}$$

where erf^{-1} is the inverse of the error function. This value of sigma comes from a one-sided Gaussian distribution because the calculated significances are defined to be the probabilities to have a result greater or equal to a certain value.

9.1.2. Sky-map

Given that no evidence for a signal was found in the candidate source list, the whole Northern sky was scanned looking for point sources using a grid of overlapping bins. The sky-map with the significances of the bins in terms of the excess parameter (ξ) is shown in Fig. 9.3 together with the single events represented by point markers. The ξ distribution of all bins is presented in Fig. 9.2a, alongside with the same distribution that is obtained when only background events (randomized skymaps) are used. It can be seen that the data resemble the background-only distribution.

The hottest spot in the all-sky search was located at $dec = 47^o$, $ra = 12.23$ h, with a pre-trial p-value of 7.5×10^{-5} ($3.79\ \sigma$). In order to calculate the post-trial probability, randomized all-sky maps are created, giving as a results the normalized excess parameter distribution shown in Fig. 9.2a. A distribution with the maximum ξ for each randomization is created (Fig. 9.2b) with the goal to estimate the post-trial value of the highest deviation in data.

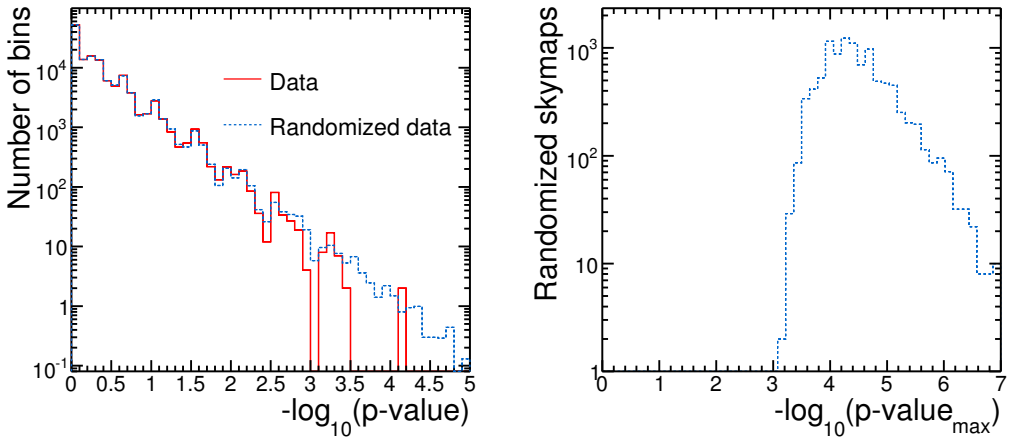

(a) Data excess parameter

(b) Randomized max. excess parameter

Figure 9.2.: Left: Excess parameter distribution in the real skymap (data) and from randomized skymaps using the IC22 Northern sky sample. Right: Distribution of the maximum excess parameter in a skymap, for randomized data using the same IC22 sample.

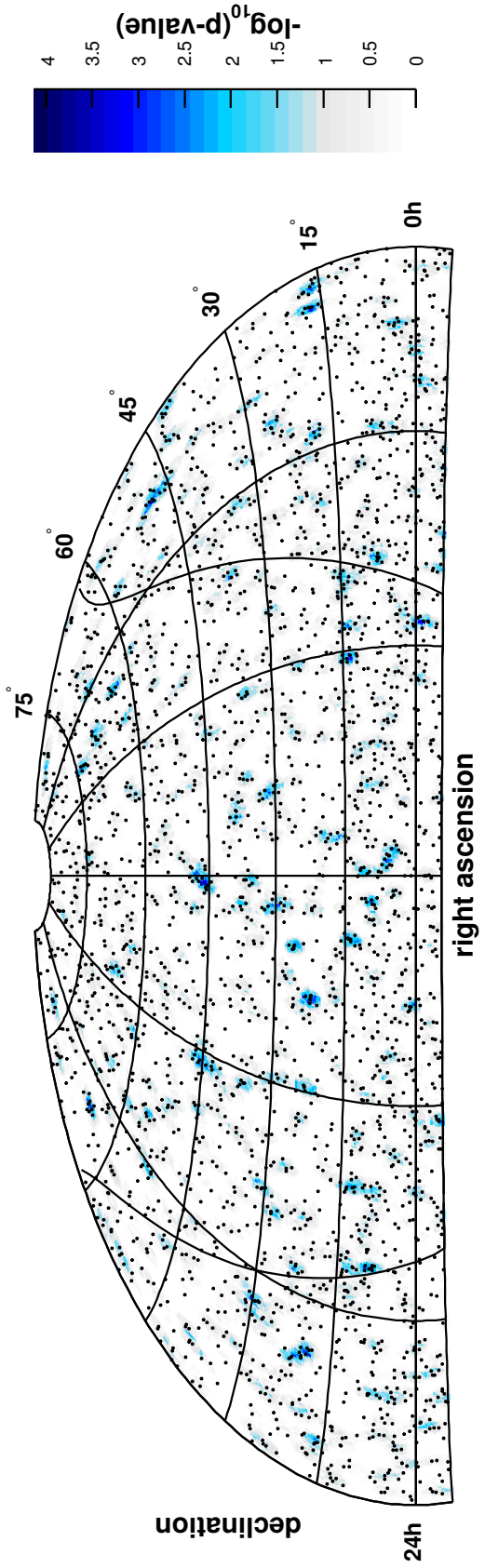

Figure 9.3.: Skymap of the bin significances and events for the Northern sky with the IceCube 22-string configuration in equatorial coordinates. The pre-trial significance (color coded) is obtained with the binned method. There are a total of 2568 events below the horizon.

The probability that in randomized skymaps the maximum significance is greater than 3.79 sigma (pre-trial) is 67.6%, which is the post-trial p-value of the all-sky search. This gives a better significance than the pre-defined source search. Given the fact that both searches were performed, the best obtained significance must be corrected for the trial of carrying out two searches. Therefore, the final combined trial-corrected p-value is 89.5%.

9.2. Search for variable point sources in the whole sky

The untriggered unbinned neutrino flare search (see Sec. 6.3.2) was applied separately to two sets of ICECUBE data from different configurations: IC22 (Sec. 7.6.2) and IC40 (Sec. 7.6.2), using two lists of candidates sources (see Sec. 8.2.1 and Sec. 8.2.2) in the whole sky. In both cases the results were compatible with background fluctuations, thus upper limits on the neutrino fluence were calculated for readiness using the Neyman approach. This limits are ∼10% lower compared to the ones given by the F&C approach.

9.2.1. ICECUBE 22-string results

Table 9.2 shows the results for each of the 10 sources in the selected catalog for IC22. The significances as a function of the p-value are shown in a skymap in Fig. 9.4. The maximum significance found was p-value=4.7% (1.67 σ) for 3C 454.3. After applying the correction for the trials of using 10 sources, the final p-value is 9.2%. The corresponding time window of the best cluster was 0.5 days. Since no significant deviation from the background only hypothesis was found, fluence upper limits were calculated.

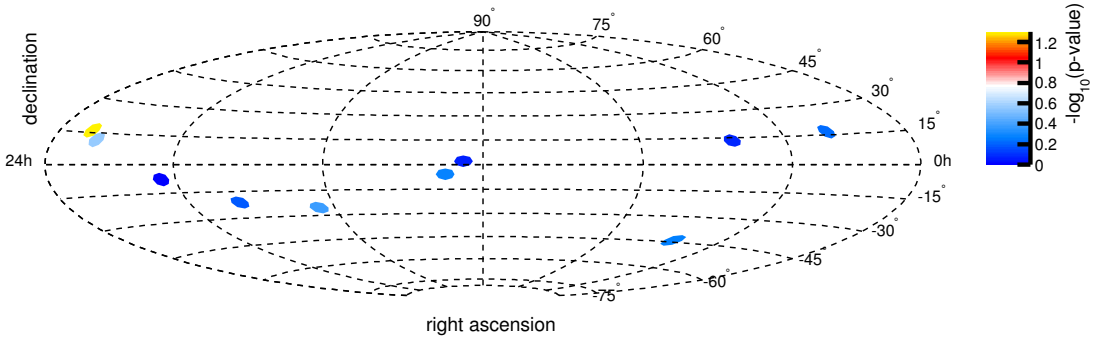

Figure 9.4.: P-values in the sky of the selected 10 sources for IC22.

Table 9.2.: IC22 results for pre-defined variable astrophysical source candidates using the time dependent search.

Source	**Other Name**	**dec** [°]	**ra** [°]	**p-value**	**Δt** (days)	**n_s**	**$\Phi_{90} \times 10^{-10}$** TeVcm^{-2}s^{-1}	**Fluence limits** GeVcm^{-2}
GEV J0540-4359	3EG J0540-4402	-44.1	84.7	0.54	7.08	0.84	89.3	29.8
GEV J1626-2502	3EG J1626-2519	-25.5	246.4	0.41	22.8	0.49	17.4	22.8
GEV J1832-2128	3EG J1832-2110	-21.1	278.4	0.64	4.49	0.26	46.8	12.0
GEV J2024-0812	3EG J2025-0744	-7.6	306.4	-	3.55	<0.01	15.1	3.7
3C 279	3EG J1255-0549	-5.8	194.1	0.52	0.19	2	266.9	3.3
3C 273	3EG J1229+0210	2.0	187.3	0.84	1.97	1.43	3.2	0.37
CTA 102	3EG J2232+1147	11.7	338.1	0.27	3.7	2.82	6.3	1.42
GEV J0530+1340	3EG J0530+1323	13.5	82.7	0.82	3.48	1.65	2.3	0.47
3C 454.3	3EG J2254+1601	16.1	343.5	0.047	0.5	2	73.8	2.22
GEV J0237+1648	3EG J0237+1635	16.6	39.7	0.59	1.99	1.79	9.1	1.08

Notes.- The p-value was calculated from simulated background skymaps, Δt is the flare duration of the best cluster, n_s is the number of signal events estimated with the likelihood method, Φ_{90} is the upper limit (E^{-2}) for the time window (Δt) calculated using the Neyman approach (when there is a downward fluctuation, the median sensitivity is quoted as a conservative value) and the fluence upper limit was calculated by integrating $d\Phi/dE \times E$ over the 90% energy range and Δt.

9.2.2. IceCube 40-string results

The untriggered neutrino flare search was applied to the 40 selected source candidates using IC40 data. No significant excess above the atmospheric background is found, therefore upper limits on the neutrino fluence are calculated. The results for each source are presented in Table 9.3 and the fluences are summarized in Fig. 9.5. The highest fluctuation observed corresponds to 0FGL J0643.2+0858 (dec=8.9^o, ra=100.8^o) with a p-value=8% (1.4 σ) (not including the trial factors generated by looking at 40 sources). Including the correction for the 40 sources, based on a dedicated simulation constructing the background pdf from the best significance from all 40 sources for each simulation, the final post-trial p-value is 94.9% (a simple correction of a trial factor of 40 gives a conservative value of 96.4%). The corresponding best time cluster was 14.3 days.

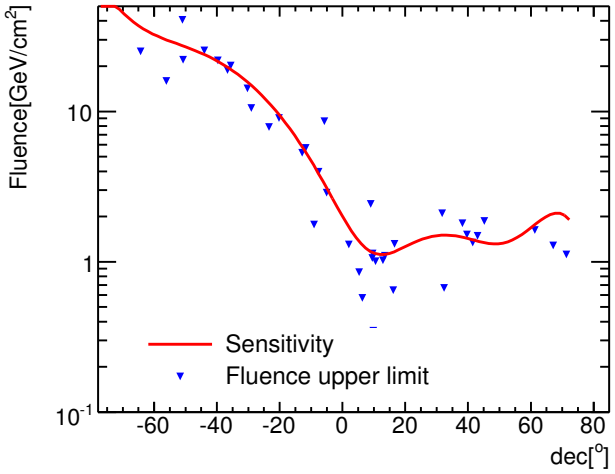

Figure 9.5.: Fluence upper limits, using the Neyman approach, of the 40 selected sources as function of declination and the median sensitivity.

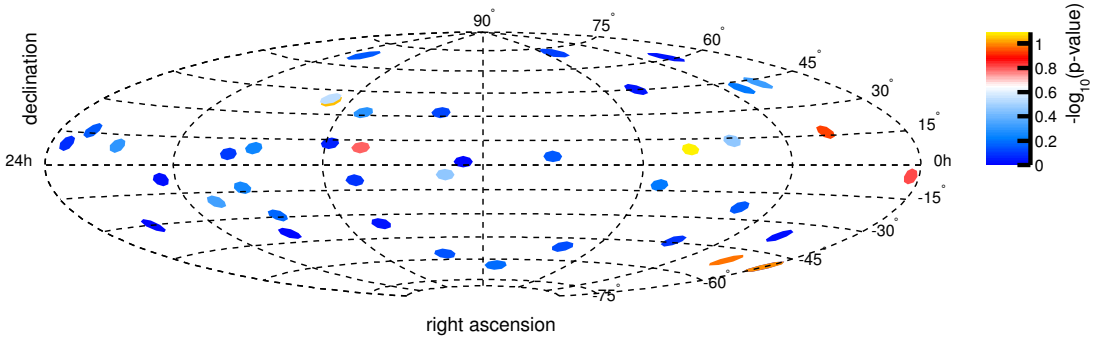

Figure 9.6.: P-values in the sky of the selected 40 sources for IC40.

Table 9.3.: IC40 results for pre-defined variable astrophysical candidates using the time dependent search.

Source (0FGL)	**Other Name**	**dec** [°]	**ra** [°]	**p-value**	Δt (days)	n_s	**Uptime**	Φ_{90} $\times 10^{-10}$ TeVcm^{-2}s^{-1}	**Fluence limits** GeVcm^{-2}
J1123.0-6416		-64.27	170.8	0.64	14.2	3.57	0.907	41.8	25.1
J1328.8-5604		-56.08	202.2	0.72	22.6	3.94	0.946	17.7	15.9
J0210.8-5100	PKS 0208-512	-51.01	32.71	0.1	18.4	5.87	0.936	52.9	40.7
J0910.2-5044		-50.74	137.6	0.73	4.02	2.97	0.725	131	22.1
J0538.8-4403	PKS 0537-441	-44.06	84.72	0.82	3.63	2.01	0.678	167	25.5
J1802.6-3939		-39.66	270.7	0.96	11	2.91	0.993	44.1	21.9
J0229.5-3640	PKS 0227-369	-36.68	37.38	0.93	8.3	2.64	0.953	50.2	18.8
J1457.6-3538	PKS 1454-354	-35.64	224.4	0.92	24.9	2.96	0.928	17.7	20.2
J2158.8-3014	PKS 2155-304	-30.24	329.7	0.97	19.8	2	0.971	15.9	14.3
J1746.0-2900		-29	266.5	0.65	11.4	3.99	0.902	20.2	10.5
J0457.1-2325	PKS 0454-234	-23.43	74.29	0.7	17.2	3.98	0.91	9.85	7.89
J1911.2-2011	PKS 1908-201	-20.19	287.8	0.47	3.81	3.16	0.987	50.7	9.02
J1813.5-1248		-12.8	273.4	0.56	0.971	2	0.983	103	5.32
J0730.4-1142	PKS 0727-11	-11.71	112.6	0.6	27.4	6.33	0.927	3.77	5.72
J1512.7-0905	BZQ J1512-0905	-9.093	228.2	0.8	0.979	2	0.995	30.6	1.77
J2025.6-0736	PKS 2022-07	-7.611	306.4	0.95	2.08	2	0.766	30.3	3.98
J1256.1-0547	3C 279	-5.8	194	0.34	21.8	6.7	0.41	5.81	8.6
J0017.4-0503		-5.054	4.358	0.15	3.25	3.79	0.995	12.7	2.89
J1229.1+0202	3C 273	2.045	187.3	0.97	28.5	4.77	0.957	0.646	1.3
J1015.9+0515	PMN J1016+0512	5.254	154	0.69	4.46	2.93	0.86	2.89	0.855
J1830.3+0617		6.287	277.6	0.79	2.37	2	0.94	3.8	0.574
J0643.2+0858		8.983	100.8	0.08	14.3	4.97	0.749	2.84	2.43
J2147.1+0931	PKS 2144+092	9.519	326.8	0.5	27.8	5.28	0.946	0.648	1.06
J1751.5+0935	OT 081	9.591	267.9	0.57	24.6	5.01	0.832	0.78	1.13
J2327.3+0947	PKS 2325+093	9.794	351.8	0.82	2.84	2	0.979	2.09	0.348
J1504.4+1030	PKS 1502+106	10.51	226.1	0.16	0.151	2	1	114	1.01

Table 9.3 – continued from previous page

Source (0FGL)	**Other Name**	**dec** [°]	**ra** [°]	**p-value**	**Δt** (days)	**n_s**	**Uptime**	**Φ_{90} $\times 10^{-10}$** TeVcm^{-2}s^{-1}	**Fluence limits** GeVcm^{-2}
J1553.4+1255	PKS 1551+130	12.92	238.4	0.87	4.92	2	0.989	3.67	1.03
J0531.0+1331	PKS 0528+134	13.53	82.76	0.34	0.581	2	0.971	33.3	1.1
J2254.0+1609	3C 454.3	16.15	343.5	0.7	7.94	3.94	0.989	1.49	0.647
J0238.6+1636	AO 0235+164	16.61	39.66	0.12	0.216	2	1	112	1.32
J1522.2+3143	TXS 1520+319	31.73	230.6	0.51	3.95	3	0.542	10.5	2.11
J1310.6+3220	B2 1308+32	32.34	197.7	0.75	13.9	2.98	0.977	0.971	0.669
J1635.2+3809	4C +38.41	38.16	248.8	0.089	0.268	2	0.998	136	1.8
J1641.4+3939		39.67	250.4	0.29	0.268	2	0.998	115	1.52
J0320.0+4131	NGC 1275	41.52	50	0.61	28.3	4.71	0.957	0.959	1.34
J0222.6+4302	3C 66A	43.04	35.65	0.48	19.6	3.98	0.98	1.56	1.49
J0654.3+4513	B3 0650+453	45.22	103.6	0.92	5.85	2	0.841	6.57	1.86
J0240.3+6113	LS I+61 303	61.23	40.09	0.91	6.19	2	0.988	5.78	1.63
J1849.4+6706	S4 1849+67	67.1	282.4	0.69	10.6	2.99	0.991	2.73	1.28
J0722.0+7120	S5 0716+71	71.35	110.5	0.76	7.11	2	0.905	3.91	1.12

Notes.- The source name corresponds to the OFGL, the preliminary Fermi gamma-ray LAT list [A$^+$09e]. The p-value was calculated from simulated background skymaps, Δt is the flare duration of the best cluster, n_s is the signal event estimate from the likelihood, *uptime* is the fraction during Δt when the detector had good data, Φ_{90} is the upper limit (E^{-2}) for Δt calculated using the Neyman approach; this limit includes a correction for the detector uptime during the time of the flare (when there is a downward fluctuation, the median sensitivity is quoted as a conservative value) and the fluence upper limit was calculated by integrating $d\Phi/dE \times E$ over the 90% energy range and Δt.

9.3. Uncertainties

To the extent that measurements are not absolutely precise and that the analysis is not free of uncertainties, a robust result on the flux and fluence limits should include the necessary error estimates. The error on the background is mostly statistical, because it is estimated directly from data. Nevertheless, a modelling of the background time structure is used (see Sec. 6.3.1) and also parametrizations of its properties are included in the unbinned likelihood method, which account for a minor systematical error. On the contrary, the error on the expected signal has a larger systematical contribution and a minor statistical error (i.e. from the limited amount of simulation used).

9.3.1. Statistical errors

In Fig. 9.7a the statistical errors for the time-integrated analysis using IC22 data and simulation are shown. To account for the statistical errors, the number of events in a given declination band containing the search bin is counted. The error itself is given by $\frac{\sqrt{N}}{N}$ (%), for data, where N is the number of events in the band. For the weighted E^{-2} signal neutrino simulation, it is defined as: $\frac{\sqrt{\sum(w^2)}}{\sum(w)}$ (%), where w is the weight of each simulated event. The statistical error for background (from data) ranges from 6.5% to 11.3%, while for a E^{-2} neutrino signal (simulation) it varies from 0.6% to 3.3%.

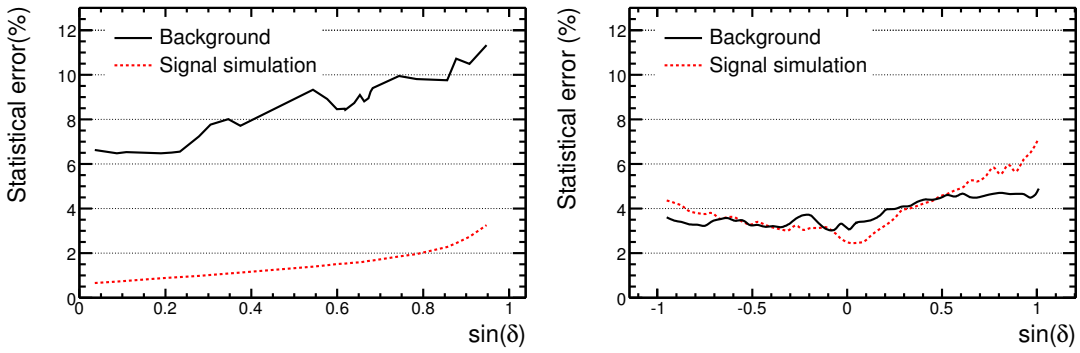

(a) IC22 (b) IC40

Figure 9.7.: Statistical errors from background and neutrino signal simulation.

For the IC40 event sample the statistical errors were calculated likewise using a fixed declination band of 6^o, as implemented in the unbinned method. The results are shown in Fig. 9.7b. The statistical error from data varies from 3.1% to 4.9%, while the range for a E^{-2} neutrino signal is 2.5% to 7.1%. The improvement in the statistical error from data is evident since the event sample has increased around 5,5 times from IC22 to IC40, due to not only the growth of the detector, but to the looser event selection of an unbinned method.

9.3.2. Systematic errors

There are several sources of systematic errors, the most important being the modeling of light propagation in the ice, including ice properties, which accounts for a 16%

error. The uncertainties on the DOM efficiency contribute with $\sim$ 6%. Theoretical uncertainties related to the muon energy loss and neutrino cross section are at the level of $\sim$ 3%. These general sources of errors and other systematic uncertainties specific to each analysis are discussed in this section.

Light propagation and ice properties

The modeling of the deep South Pole ice, the detector medium, and the propagation of light through the ice are the largest sources of uncertainty. This ice, though extremely clear, contains several layers of dust which produce depth dependent variations in the scattering and absorption coefficients.

In order to estimate the uncertainty related to the properties of the ice and the propagation of light in this medium, the following approach is taken. A modification of the ice model is simulated, by varying the DOM efficiency as a function of depth according to the observed differences between data and simulation [K$^+$09]. This mimics a different average photon travel length (distance of closest approach between the track and the center of gravity of the hit DOMs). Indirectly modifying the ice properties yields a 16% worsening of the detected flux.

DOM efficiency

The errors related to the DOM performance are associated with the PMT quantum efficiency, as well as with their glass spheres and gel transmission. In the simulation, an average value coming from laboratory based measurements is used. However, their properties are expected to have a variation of $\pm$10 %. The glass effect on the short wavelength cutoff and the gel properties variations are at the level of 1%. From PMT calibrations a 8% variation is observed. A modification of $\pm$10% in the global efficiency for photon detection in a muon neutrino simulation (10 - 10^{10} GeV) gives as a result for E^{-2} a $^{-4.4}_{+6.3}$ % deviation on the expected number of neutrinos [L$^+$09].

Theoretical uncertainties

The theoretical uncertainties are summarized here:

- Neutrino cross section: $\pm$2%
- Muon propagation: $\pm$3%
- Bedrock density uncertainty: $\pm$3%

The error on the neutrino cross section can modify the normalization of the expected signal flux. For the energies of the present analyses a deep inelastic scattering is considered, thus parton distribution functions are used. The CTEQ5 structure functions, used in the neutrino simulation, start to deviate from the newest CTEQ6 for energies greater than EeV, which is beyond the scope of the analyses. The uncertainty on the parton distribution functions from CTEQ6 is about 2%, while the error from quark masses and mixing is <1% [P$^+$02]. The errors increase with the energy of the neutrino.

The muon propagation code used in the ICECUBE simulation is compared to other codes [CR04]. An uncertainty of about 3% is obtained. The errors come from the uncertainty in the parametrization of the muon energy loss processes (ionization, bremsstrahlung, pair-production, etc.). In addition, the density of the bedrock (interaction

and conversion region) below the detector is not known precisely. A standard value for the rock density is used ($\rho = 2.65$ gcm^{-3}). Changes in this assumed value affect the muon interaction probability [MS03]. Varying the density by a 10% tolerance gives an uncertainty of 3% in the event rate.

The difference between the direction of the incoming neutrino and that of the resulting muon, scattering angle, is almost neglegible in the energy range (>TeV) of the analyses, where the relativistic boosting due to high velocities makes them almost collinear. Therefore the error of assuming the direction of the muon as the direction of the neutrino is not important [Ack06] (less than 1%).

Errors in simulation and data processing

Errors (*bugs*) have been found in the neutrino simulation and data processing used for the analyses after these have been carried out. With the purpose of testing the effects of these errors on the signal neutrino flux estimation and data event selection, old and new simulations and processing versions are compared. The differences are taken as systematic errors.

For the IC22 time-integrated analysis the corrected simulation version increases uniformly the light amount in the ice layers. The associated systematic errors (difference between number of selected signal events) due to this correction are small: +0.3% (E^{-2} signal), +2.2% (E^{-3} signal) and +2.3% (atmospheric neutrinos).

For IC40 the new data processing corrects anomalies in the waveform reconstruction, that led to the loss of charge (i.e. underestimation of the total charge). This error can affect the MPE reconstruction since it takes into account the total charge. The final event sample used in the analysis has been reprocessed. The effects on the directional and energy reconstruction are small compared to their respective resolutions [D$^+$10]. The signal efficiency for a E^{-2} energy spectrum is reduced by <4%.

Bias in reconstruction and cutting parameters

Although the same reconstruction algorithm is applied to data and simulation, if simulated events do not include a correct description of reality (e.g. wrong DOM's noise rates), this can affect the reconstruction results. Such bias in reconstruction would lead to a disagreement between the cutting parameters from data and simulation, thus introducing systematic errors.

This difference can be quantified by comparing the distributions of derived cutting parameters from atmospheric neutrino simulation to the final data sample. This is done by means of the pull, defined by:

$$Pull = \frac{x_{Data} - x_{MC}}{\sqrt{\sigma^2_{Data} + \sigma^2_{MC}}} \ , \tag{9.2}$$

where x_{Data} and x_{MC} are the number of data and simulated events in a bin, respectively, and σ_{Data} and σ_{MC} are the standard deviations from data and simulation. The distributions are compatible when the pull approaches zero. In addition, a Kolmogorov-Smirnov test is performed in order to obtain the probability that the simulation resembles the data sample.

However, the final data sample from this analysis cannot be directly compared to the atmospheric neutrino simulation because there is still contamination from misreconstructed muons. This fact has already been discussed in Sec. 7.6.1, concluding that by tightening the cuts a neutrino pure sample can be obtained. Therefore, stronger cuts are applied to approach a pure atmospheric neutrino sample. Another possibility is to use a zenith cut ($\theta > 115^o$), taking only the region where the agreement between data and atmospheric simulation is good. The largest systematic error from both alternatives is chosen in order to give a conservative estimate.

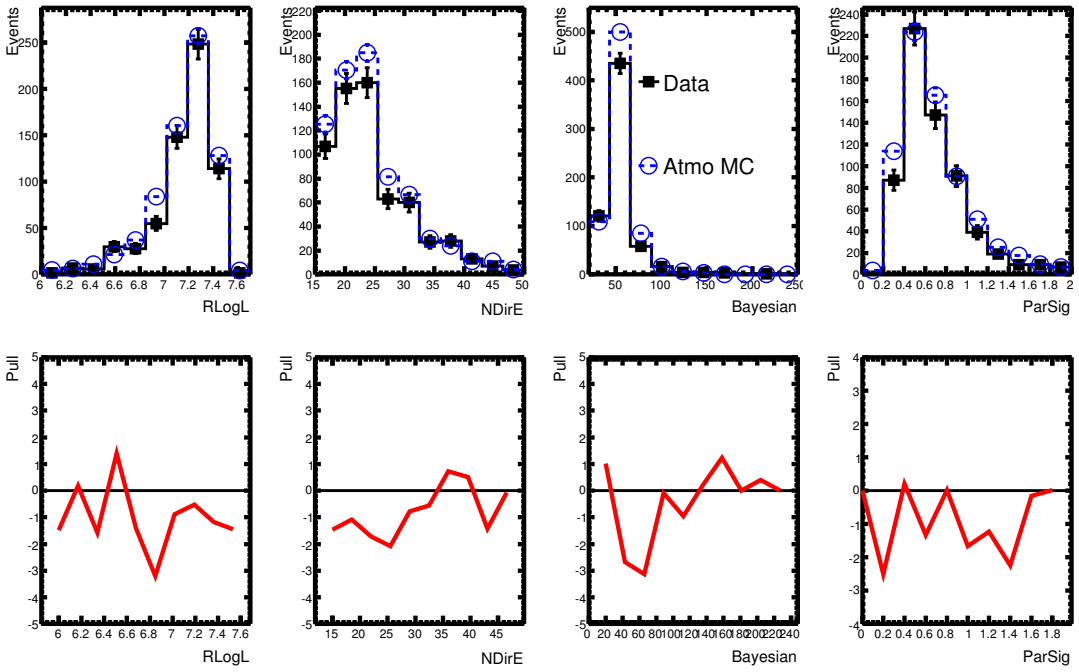

Figure 9.8.: Distributions of track-reconstruction dependent parameters after applying stronger cuts in IC22.

The main reconstruction parameters used in the event selection are investigated. A comparison of the distribution of these parameters after applying stronger cuts is shown in Fig. 9.8, with the corresponding value of the pull. The agreement between data and atmospheric neutrino simulation parameters improves after stronger cuts. The remaining disagreement can be overcome by a simple modification (i.e. scaling or shifting factor) of the simulation parameters. The scaling or shifting factor that yields the highest KS probability is found for each parameter. The difference in the number of expected signal events passing the final chosen cuts with and without scaling/shifting gives the systematic error from reconstruction bias. The maximum error for each parameter from both sets of cuts (stronger and zenith cuts) is chosen as a conservative estimate of the systematic error. Table 9.4 presents the systematic errors for individual reconstruction parameters for different energy spectra and the total error is given as the quadrature sum of all parameter errors.

Error	E^{-2}	E^{-3}	Atmospheric
RLogL	1.53%	1.50%	1.53%
NDirE	<0.01%	<0.01%	<0.01%
ParSigma	0.71%	1.43%	1.58%
BayeRatio	0.03%	0.10%	0.09%
Quadrature sum	1.69%	2.07%	2.2%

Table 9.4.: Systematic errors on the flux from parameter reconstruction bias for different energy spectra.

Angular error estimate

The unbinned method includes the reconstruction angular error estimate (paraboloid sigma, see Sec. 7.3.2) in the signal description. If paraboloid sigma would have a different value (e.g. systematically shifted) in simulation with respect to data, then this will affect the discovery potential. In Fig. 9.9a the distributions from the final event sample and atmospheric neutrino simulation are compared. A good agreement is found.

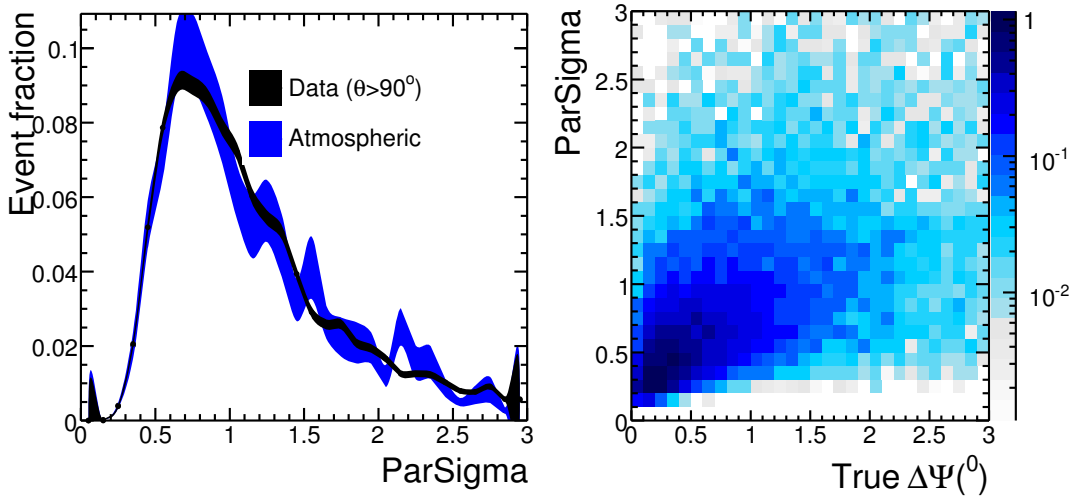

(a) Data/simulation comparison

(b) Estimated versus true angular error

Figure 9.9.: Left: Comparison of data and atmospheric neutrino simulation distributions of the angular error estimate. The shadowed regions correspond to the statistical error on data and the theoretical error on the atmospheric flux prediction. Right: Correlation of the estimated angular error to the true one for a E^{-2} signal simulation.

In addition, the discovery potential would be affected if paraboloid sigma would yield an incorrect estimate of the angular error. The correlation between the true (i.e. from simulation) and estimated angular error is shown in Fig. 9.9b. The estimated angular error has been corrected, as described in App. A, to match the true error. However, it is an average correction and the spread in the correlation plot indicates that estimates of the angular error used in the unbinned method likelihood are still inaccurate.

In order to evaluate the impact of an incorrect angular error estimate for the reconstructed muon track in the discovery potential, the paraboloid sigma value is changed by 10%. This results in a modification of the discovery potential by 2.2%.

Energy estimate

The unbinned method also uses the estimated energy (*mue*, see Sec. 5.2.5) in the signal and background descriptions of the likelihood. The systematic error introduced by the energy estimate is evaluated using the same procedure as for the angular error estimate. In Fig. 9.10a the distributions from the final event sample and atmospheric neutrino simulation are compared. A slight disagreement for higher energies is observed. It can be due to the presence of misreconstructed coincident muons that mimic an up-going event, but producing more light or a bias in the energy reconstruction between data and simulation at the level of <10%.

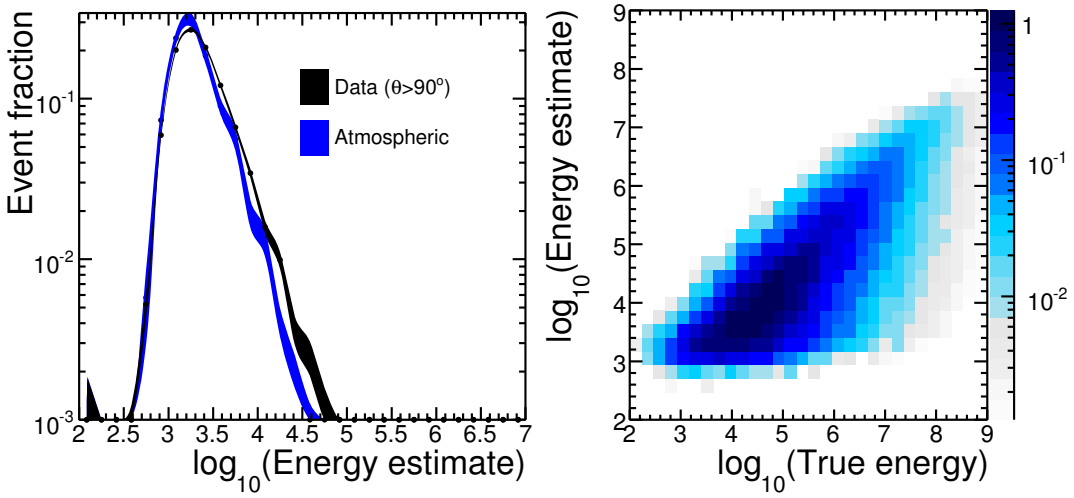

(a) Data/simulation comparison

(b) Estimated versus true energy

Figure 9.10.: Left: Comparison of data and atmospheric neutrino simulation distributions of the energy estimate (*mue*). A zenith cut $\theta > 115^0$ is included to provide a pure atmospheric neutrino sample. Right: Correlation of the energy estimate to the true energy for a E^{-2} signal simulation.

In the correlation plot (Fig. 9.10b) between reconstructed and true energy, an underestimation of the true energy is noticed. The effect of an underestimation of the reconstructed energy in the discovery potential is calculated by modifying the estimated energy by +10%. This changes the discovery potential by -7.5%.

Fits to rates

The background time term in the likelihood used in the untriggered time dependent unbinned method contains a fit to the event rates (see Sec. 6.3.1) that describes the seasonal variations of the atmospheric muon events in the Southern sky. Since the time dependence of the background is not entirely described by a sinusoidal fit, given the daily changes in temperature, these differences should be accounted for as systematic

errors. Therefore different fits (e.g. constant fit, linear fit) are tested and the highest deviation is chosen as a conservative estimate of the systematic error coming from using a fit to the background time dependence. The associated error, 0.2%, is negligible.

9.3.3. Errors summary

Most of the uncertainties described above are common to all analyses, however since some are particular to the unbinned method and others only apply to the IC22 or IC40 sample, they are summarized in Table 9.5 for each analysis . The total systematic error is at the 20% level, though it is 2% smaller when the binned method is applied, since in the implementation used in this work no energy term has been included. If other larger systematic uncertainties were reduced (e.g. ice properties and light propagation) the error on the energy estimate would play a more important role.

Source of uncertainty	**IC22 time integrated** (binned)	**IC22 time variable** (unbinned)	**IC40 time variable** (unbinned)
Statistical	11.3%	11.3%	4.9%
Systematic			
Light propag./ice prop.	16%	16%	16%
DOM efficiency	6.3%	6.3%	6.3%
Neutrino cross section	2%	2%	2%
Muon propagation	3%	3%	3%
Bedrock density	3%	3%	3%
Sim./data processing	0.3%	0.3%	4%
Reconstruction bias	1.7%	1.7%	$\sim$1.7%
Angular error estimate	-	$\sim$2.2%	2.2%
Energy estimate	-	$\sim$7.5%	7.5%
Time modeling of background	-	$\sim$0.2%	0.2%
Total systematic error	17.9%	19.5%	19.9%

Table 9.5.: Statistical and Systematic errors summary for all analyses. There are no errors associated with the angular error and energy estimates for the binned analysis, since these parameters are not used in the method. In addition, the time integrated analysis has no time modeling of the background.

9.3.4. Limits including uncertainties

The Feldman-Cousins approach gives flux upper limits without taking into account any statistical or systematic errors, either on the background or the expected signal. In order to include these errors, the method described in [C$^+$03] is used, in particular the POLE [Con02] program. This method constructs the confidence belts including the uncertainties by averaging the probabilities over the error range. A Gaussian parametrization is assumed for both systematic and statistical errors. Incorporating the statistical and systematic errors in the flux upper limit calculation gives an absolute change of 3.5% (1.2% average change).

It should be pointed out that tau neutrinos would also contribute to a muon flux, because they can give rise to taus which decay to muons (with a 17.4% branching ratio).

Since an equal astrophysical flux of tau neutrinos and muon neutrinos is expected from neutrino oscillations (see Sec. 2.5), the fluxes presented here are conservative. If the tau neutrino component would be included, it would lead to a tighter upper limit on the muon neutrino flux.

10. Summary and Outlook

> Wir sind in unserer Wissenschaft an die Grenzen des Erkennbaren gestoßen. Wir wissen einige genau erfaßbare Gesetze, einige Grundbeziehungen zwischen unbegreiflichen Erscheinungen, das ist alles, der gewaltige Rest bleibt Geheimnis, dem Verstande unzugänglich.
> Friedrich Dürrenmatt 1921-1990
> *Die Physiker*

If hadrons can be accelerated to ultra-high energies in astrophysical sources, for example AGNs, a flux of high energy neutrinos and γ-rays is also expected from these objects. ICECUBE, a km-scale neutrino telescope, is being constructed at the South Pole with the main purpose to detect such neutrinos in the TeV-PeV energy range. Data from two partial configurations of ICECUBE, 2007 to 2009 (651 days of lifetime), have been analyzed in this thesis. The various searches for neutrino point sources presented in this work were compatible with fluctuations of the background.

An event selection for the Northern sky, aimed at obtaining the best sensitivity, was developed for the ICECUBE 22-string configuration (IC22). A binned method was used for a time-integrated search. An a-priori selected list of promising astrophysical neutrino sources and the whole Northern hemisphere were searched for point sources of neutrinos. In both cases no signal was found. Flux upper limits were calculated for the selected sources. These limits were 40% better than those from the total statistics collected with the AMANDA-II detector [A$^+$09c].

A comparison with a time integrated unbinned method implemented in [A$^+$09b], proved that an unbinned method can give tighter flux limits. The reason for this is that signal events outside a fixed angular bin could still contribute to the signal, if their estimated directional error was large. In addition, the unbinned method included an energy term that further helped to distinguish background from signal events. Nevertheless, the binned analysis developed in this work represented a cross-check to the unbinned analysis, which was not yet well stablished.

An untriggered time dependent search that looks for neutrino flares was then developed in this thesis in order to enhance the detection chances. Neutrino flares are expected to take place in astrophysical sources given the observations of flaring blazars and other sources in γ-rays and other wavelengths. This hypothesis is supported by the neutrino-photon correlation, predicted by hadronic models, at production in the sources. An independent (untriggered) analysis of neutrino data, not directly triggered by γ-ray observations, is in order since photon data is not available for all sources during complete periods. In addition, there could be a time lag between observed photon flares and neutrinos or γ-rays could have been absorbed, while neutrinos can escape dense media. This analysis covers a wide range of possible flare durations.

Motivated by the results of the previously mentioned comparison (binned versus unbinned method), the search for neutrino events clustering in time was expanded in this work from a binned approach [S$^+$07] to an unbinned method. The likelihood in

this unbinned method included, in addition to a spatial term, energy and time terms that characterized signal and background. The new method improves the binned results by 5% to 25% increasing with the duration of the flare. For flares of duration less than $\sim$ 30 days, this time dependent search has proven to perform better than a time integrated search method. For a discovery of an hour-scale flare, this search requires less than half of the events needed in a time-integrated analysis.

For the first time the Southern sky was also analyzed with a time-dependent method. This required an accurate description of the seasonal variations, because the background for the Southern sky is composed of atmospheric muons. Furthermore, a detailed background modeling was implemented for the whole sky.

New source selection criteria were developed in this work. Two pre-defined lists of variable astrophysical sources, distributed in the entire sky, were defined first for IC22 and updated for IC40. The results of the untriggered unbinned time dependent method are compatible with the background-only hypothesis for all sources tested, using IC22 and IC40 data. Therefore upper limits on the neutrino fluence from these sources have been calculated.

Given that there is no lower threshold for the duration of a flare in the search method, GRBs could also be detected. However, the coincidences of GRB locations with the selected variable blazars and other astrophysical sources are low. Only one coincidence within 1^o was found. However, the limits coming from a specialized GRB search are, as expected, orders of magnitudes better.

This untriggered time-dependent search was later carried on in IceCube with a similar analysis developed elsewhere [B$^+$10a], where a scanning of the sky was done. The methods are essentially the same and when the discovery probability of a single source was compared, it was found out be similar. No neutrino flare using IC40 data was found in this search either.

The systematic uncertainties associated with the different analyses developed in this thesis have been fully calculated. These errors are at the level of 20%, the largest contribution (16%) coming from the partial understanding of the ice properties and light propagation.

ICECUBE is setting each year, with new data and a larger configuration, tighter limits on the astrophysical neutrino flux. The limits from the 22-string configuration improved by a factor of two the results from the total statistics collected with the AMANDA-II detector [A$^+$09c]. The next configuration, 40-strings, superseded the IC22 results by a factor of $\sim$ 2, which is mostly related to the larger detection volume and also to the $\sim$40% improvement in the angular resolution of muons. Data collected in one year by the completed ICECUBE detector is expected to improve the IC40 sensitivity to a point source flux of neutrinos by yet another factor of 2 or more. By combining several years of observations and with a further improvement in the reconstruction and analysis methods, the sensitivity to steady neutrino point sources will be enhanced up to an order of magnitud.

The chances of discovering a neutrino point source will also increase in the near future with the contribution from other already running or planned detectors. The sensitivity to point sources in the Southern sky, which is currently only accessible at ultra high energies, will be extended to low energy ($\sim$ 10 GeV) sources with DEEPCORE, a newly deployed denser subarray of the ICECUBE Observatory. In addition, the Southern sky would also gain in sensitivity in the high energy range (TeV-PeV) with the construction of a neutrino telescope in the Northern hemisphere. The KM3NeT Con-

sortium plans to deploy such a detector in the Mediterranean Sea with a volume at least as large as that of ICECUBE. A full-sky coverage at a wide range of energies of possible astrophysical neutrino sources might be a reality soon.

Non neutrino-related experiments can also contribute to increase the discovery potential of astrophysical neutrino sources in the framework of multi-messenger analyses. New γ-ray and cosmic-ray data can be used to look for space and time correlations with neutrino events. The lightcurves from the Fermi satellite will be used to choose the most promising flare windows in triggered flare searches of neutrinos. Fermi data will also help to characterize the time variability of many astrophysical sources, improving the source selection for untriggered time-dependent neutrino searches. Follow-up observations from Imaging Atmospheric Cherenkov Telescopes (e.g. MAGIC) triggered by neutrino telescopes will enhance the probability of discovering a neutrino flare, by using the photon-neutrino production correlation expected at the sources. New cosmic-ray data on the highest energy particles detected by the Pierre Auger Observatory and by the Telescope Array will be used together with IceCube neutrino data looking for correlations.

With the construction completion of ICECUBE in 2011, the mentioned upcoming experiments and multi-messenger analyses, the astrophysics neutrino community might soon find an evidence for astrophysical neutrinos. If these neutrinos would be associated with known objects, hadronic models would be confirmed.

A. Parametrization of the angular error from reconstruction

The angular error estimate of the track reconstruction is obtained via the paraboloid error ellipse (see Sec. 7.3.2). Nevertheless, it is a fact that the current implementation of the MPE reconstruction paraboloid sigma is not properly describing the angular error. Therefore, an energy dependent correcting factor is obtained and applied individually for each event sample. In order to obtain the correcting factor, the pull, defined below, is calculated for each event.

$$\text{Pull} = \frac{\Delta\Psi(\text{true} - \text{reco})}{\text{Parab}_{\text{sigma}}} \ , \tag{A.1}$$

where $\Delta\Psi$ is the space angular difference between the true and reconstructed track and $\text{Parab}_{\text{sigma}}$ is the paraboloid angular error estimate. The average pull value for different energy ranges is obtained (energy given by *mue*) (see Fig. A.1). If the paraboloid estimated would be correct, then the pull should be 1. However, this is not the case. The disagreement increases for higher energies. As a next step, the average pull points are fitted with a polynomial function, which will represent the correction factor for paraboloid sigma. Fig. A.1 shows the results of applying this correction. After applying the correcting factor the average pull goes from ~ 2.6 to ~ 1.2, thus the agreement is improved.

The correction for the southern sky in IC22 is given by:

$$\text{MPE}_{\text{parab}} = \text{MPE}^{\text{old}}_{\text{parab}} \times (2.77 - 1.93x + 0.559x^2 - 0.034x^3) \ , \tag{A.2}$$

where $\text{MPE}^{\text{old}}_{\text{parab}}$ is the uncorrected value of MPE paraboloid and $x = \log_{10}(muE)$, where muE is the energy estimate. For the northern sky the correction is:

$$\text{MPE}_{\text{parab}} = \text{MPE}^{\text{old}}_{\text{parab}} \times (-13.17 + 23.15x - 12.31x^2 + 2.97x^3 - 0.33x^4 + 0.014x^5) \ . \tag{A.3}$$

The correction used for IC40 is [D$^+$09]:

$$\text{MPE}_{\text{parab}} = \text{MPE}^{\text{old}}_{\text{parab}} \times 1.19 \times (4.97 - 1.97x + 0.27x^2) \ . \tag{A.4}$$

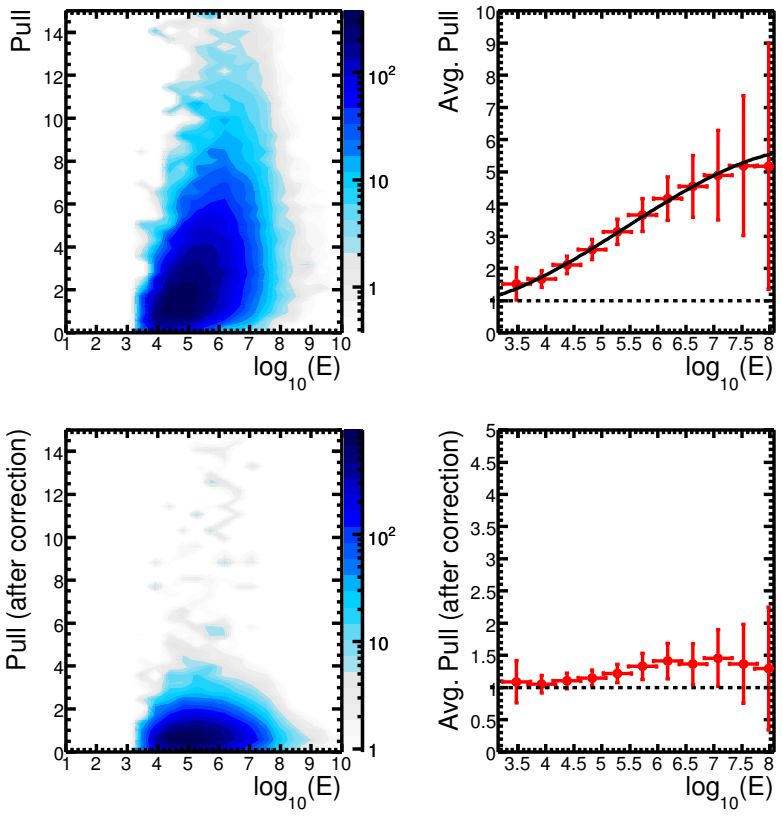

Figure A.1.: Pull distribution and fit for the UHE sample before (upper plots) and after (lower plots) the correction factor given by the black curve fit.

B. Event selection cuts expanded

The numerical values of the applied cuts described throughout Chapter 7 are presented in this appendix. For the description and motivation of the used reconstructions refer to Sec. 5.2 and for the variables see Sec. 7.3.

B.1. ICECUBE 22-string Northern sky binned event sample cuts

ICECUBE data is recorded, if the Simple Majority Trigger (SMT, 8 DOMs triggered within 5 μs) is satisfied. The next step is to apply simple reconstructions at the South Pole and select events that can be used in physics analyses (physics filters).

Level2: physics filters

The muon and extreme high energy (EHE) filters are used for the all-sky (South and North) point-source search. The muon filter is split into Northern and Southern skies in order to tackle the different backgrounds. The corresponding cuts are given in the following table.

Filter	Region	Cuts
Muon	North	Line.Z $\geq 70^o$ and NCh ≥ 10
	South	(Line.Z $\geq 60^o$ and NCh ≥ 40) or (Line.Z $\geq 50^o$ and NCh ≥ 50)
EHE	All sky	NCh >80

Table B.1.: Physics filters cuts for the 2007/08 season (IC22).

The cut parameters are Line.Z (Line-Fit reconstructed zenith) and NCh (number of channels). The combined data rate of these filters is $\sim$23 Hz. However, for the time integrated analysis, corresponding to the event sample described in this section, only the Northern sky branch of the muon filter was used.

Level3: further processing

For IC22 data further processing was required because not all higher level reconstructions were included at Level2, due to CPU time constraints. After Level2 the following cuts were applied to reach Level3 for the Northern sky:

- MuonFilter-North and Llh1.Z $\geq 80^o$ and Llh1.RLogL$<$ 13 and Llh32.Z $\geq 80^o$,

where Llh1.RLogL is the reduced log-likelihood of the SPE (see Sec. 5.2.3) reconstruction and Llh32.Z is the reconstructed zenith from a 32-fold iteration SPE likelihood reconstruction, which is first calculated during the Level3 processing. These cuts bring

the rate down to ∼3.6 Hz. Other reconstructions added at Level3 are the paraboloid error, the bayesian fit, the MPE reconstruction seeded with the 32-iterations SPE and the energy estimator *mue*.

Level4: data reduction

Before the final CPU intensive cut tuning, the data amount is further reduced to Level4 ($\sim$ 0.1 Hz) using the newly added reconstructions.

- LlhMPE.Z $> 80^o$ (further upgoing selection),
- ParabSig32<6 & ParabSigMPE<6 (improves angular resolution),
- Split1.Llh.Z$> 50^o$ & Split2.Llh.Z$> 50^o$ (coincident event rejection),
- Abs(LlhMPE.SDirE) < 0.5 (coincident event rejection),

where LlhMPE.Z is the zenith of the MPE log-likelihood reconstruction, ParabSig32 and ParabSigMPE are the paraboloid reconstruction error estimates of the 32-iterations SPE and MPE reconstructions respectively, Split1.Llh.Z and Split2.Llh.Z correspond to the first and second tracks coming from the double-muon reconstruction applied to a splitting of the events in time and LlhMPE.SDirE is the smoothness value of the MPE reconstruction.

Level5: declination-wise cuts

The final cut optimization based on the best sensitivity gives the following cuts depending on declination (δ):

Parameter	Region 1 ($\sin(\delta) < 0.3$)	Region 2 ($\sin(\delta) > 0.3$)
Llh32.RLogL	$< 8.9 - 0.75\sin(\delta)$	<8.7
LlhMPE.NDirE	$> 17.76 - 12.5\sin(\delta)$	>14
BayeRatio32	$> 27.25 + 12.5\sin(\delta)$	>31
ParabSigMPE	$< 1.8 + 3.1\sin(\delta)$	<2.75

Table B.2.: Final declination dependent cuts for the IC22 Northern sky binned sample.

The cuts variables correspond to: Llh32.RLogL, the reduced LogLikelihood from the 32-iterations SPE track; LlhMPE.NDirE, the number of direct hits in the residual time interval E (between -15 ns to +250 ns) from the MPE track; BayeRatio32, the Bayesian ratio from the 32-iterations SPE track and ParabSigMPE, the paraboloid sigma angular error estimate from the MPE track.

B.2. ICECUBE 40-string all-sky unbinned event sample cuts

For the ICECUBE 40-string configuration the physics filters cuts were tuned as to keep the rates at the same level as for IC22, since the satellite bandwidth was not increased. The muon and extreme high energy physics filters, presented in the Table below, were the starting events to the all-sky sample selection.

Filter	Region	Cuts
Muon	North	[((Llh1.Z $\geq 70^o$ and Llh2.Z $\geq 70^o$) and NCh $\geq$16) OR ((Llh1.Z $\geq 80^o$ and Llh2.Z $\geq 80^o$) and NCh $\geq$10)]
	South	NHit/NCh $\geq$5 and [((Llh1.Z $\geq 50^o$ or Llh2.Z $\geq 50^o$) and NCh $\geq$20) or ((Llh1.Z$\geq 70^o$ or Llh2.Z $\geq 70^o$) and NCh $\geq$10)]
EHE	All sky	NPE >631

Table B.3.: Physics filters cuts for the 2008/09 season (IC40).

The cut parameters are NCh (number of channels), Llh1.Z (reconstructed zenith from a single-seeded with Line-Fit Log-likelihood SPE), Llh2.Z (reconstructed zenith from a dual-seeded (Line-Fit and its reciprocal) Log-likelihood SPE, Sec. 5.2.3), NHit/NCh (number of hits per channel) and NPE (number of photo electrons), which represents the total charge of an event.

All necessary reconstructions were already included at Level2 after the physics filters. The following cuts [D^+09] deliver the final all-sky sample. They can be divided into two main sets.

The first set improves the angular resolution, rejects badly reconstructed events and reaches an atmospheric neutrino level in the Northern sky. These cuts are:

(MuonFilter-North or (MuonFilter-South & NPulses/NCh>4) || EHEFilter) &

((LLhMPE.RLogL<7.5 & ParabSigMPE<1.5) or

(ParabSigMPE<3.0 & SplitG.Llh.Z>80 & SplitT.Llh.Z>80 & BayeRatio32>30 &

LlhMPE.RLogL<8.3 & (LlhMPE.RLogL<8.0 or LlhMPE.LogL/(NCh-2.5)<7.1) &

LlhMPE.NDirC$\geq$5 & LlhMPE.LDirC>200)) &

(LlhMPE.Z<90 or BayeRatio32>30)

where MuonFilter-North, MuonFilter-South and EHEFilter correspond to the Level2 cuts, ParabSigMPE has been rescaled as a function of *mue* (see App. A), SplitG.Llh.Z and SplitT.Llh.Z are the zenith direction of the double muon reconstruction when the events are split with the geometry and in time, respectively. The other variables are the same as mentioned for IC22.

The second set of cuts reduces the background of atmospheric muons in the Southern sky as a function of energy and zenith, in a similar way as it was done for IC22. These cuts are defined by:

- cos(LlhMPE.Z)$\leq$0.05 or $\log_{10}$(LlhMPE.mue.En)>MueCut(LlhMPE.Z).

where LlhMPE.mue.En is the energy estimation of the event and MueCut is a 6^{th} order polynomial function which depends on the zenith.

Bibliography

[A+00] Athar, H.; et al.: Effects of neutrino mixing on high-energy cosmic neutrino flux. In: *Phys. Rev. D*, volume 62:p. 103007, Oct 2000. ArXiv:hep-ph/0005104v2.

[A+01a] Ahrens, J.; et al. (IceCube Collaboration): IceCube Preliminary Design Document, Oct 2001. ., URL `http://www.icecube.wisc.edu/science/publications/pdd/`.

[A+01b] Andrés, E.; et al. (AMANDA Collaboration): Observation of High-Energy Neutrinos Using Cerenkov Detectors Embedded Deep in Antarctic Ice. In: *Nature*, volume 410:pp. 441–443, Mar 2001.

[A+03] Anchordoqui, L. A.; et al.: Neutrinos from Accreting Neutron Stars. In: *Astrophys. J.*, volume 589:pp. 481–486, May 2003. ArXiv:hep-ph/0211231v2.

[A+04] Ahrens, J.; et al. (AMANDA Collaboration): Muon Track Reconstruction and Data Selection Techniques in AMANDA. In: *Nucl. Instrum. Meth. A*, volume 524:pp. 169–194, May 2004. ArXiv:astro-ph/0407044.

[A+06a] Achterberg, A.; et al. (IceCube Collaboration): First year performance of the IceCube neutrino telescope. In: *Astropart. Phys.*, volume 26:pp. 155–173, Oct 2006. ArXiv:astro-ph/0604450.

[A+06b] Ackermann, M.; et al. (AMANDA Collaboration): Optical properties of deep glacial ice at the South Pole. In: *J. Geophys. Res.*, volume 111:p. D13203, Jul 2006.

[A+07a] Achterberg, A.; et al. (AMANDA Collaboration): Five Years of Searches for Point Sources of Astrophysical Neutrinos with the AMANDA-II Neutrino Telescope. In: *Phys. Rev. D*, volume 75:p. 102001, May 2007. ArXiv:astro-ph/0611063.

[A+07b] Ackermann, M.; et al. (IceCube Collaboration): Neutrino Triggered Target of Opportunity (NToO) test run with AMANDA-II and MAGIC. In: *Proceedings of the 30th International Cosmic Ray Conference*. Mérida, Yucatán, México, Jul 2007. ArXiv:0709.2640v1.

[A+08] Amsler, C.; et al. (Particle Data Group): Review of Particle Physics. In: *Phys. Lett. B*, volume 667:pp. 1–6, Sept 2008. URL `http://pdg.lbl.gov/`.

[A+09a] Abbasi, R.; et al. (IceCube Collaboration): Extending the Search for Neutrino Point Sources with IceCube above the Horizon. In: *Phys. Rev. Lett.*, volume 103:p. 221102, Nov 2009. ArXiv:0911.2338.

[A+09b] Abbasi, R.; et al. (IceCube Collaboration): First Neutrino Point-Source Results From the 22 String IceCube Detector. In: *Astrophys. J. Lett.*, volume 701:pp. 47–51, Aug 2009. ArXiv:0905.2253.

[A+09c] Abbasi, R.; et al. (IceCube Collaboration): Search for Point Sources of High Energy Neutrinos with Final Data from AMANDA-II. In: *Phys. Rev. D*, volume 79:p. 062001, Mar 2009. ArXiv:0809.1646.

[A+09d] Abbasi, R.; et al. (IceCube Collaboration): The IceCube Data Acquisition System: Signal Capture, Digitization, and Timestamping. In: *Nucl. Instrum. Meth. A*, volume 601:pp. 294–316, Apr 2009. ArXiv:0810.4930.

[A+09e] Abdo, A. A.; et al. (Fermi Collaboration): Fermi Large Area Telescope Bright Gamma-ray Source List. In: *Astrophys. J. Suppl.*, volume 183:pp. 46–66, July 2009. ArXiv:0902.1340.

[A+09f] Aharonian, F.; et al. (HESS Collaboration): Discovery of very high energy gamma-ray emission from Centaurus A with H.E.S.S. In: *Astrophys. J. Lett.*, volume 695:pp. 40–44, Apr 2009. ArXiv:0903.1582.

[A+10a] Abbasi, R.; et al. (IceCube Collaboration): Search for Muon Neutrinos from Gamma-Ray Bursts with the IceCube Neutrino Telescope. In: *Astrophys. J.*, volume 710:pp. 346–359, Feb 2010. ArXiv:0907.2227.

[A+10b] Abraham, J.; et al. (Pierre Auger Collaboration): Measurement of the energy spectrum of cosmic rays above 10^{18} eV using the Pierre Auger Observatory. In: *Phys. Lett. B*, volume 685:pp. 239–246, Mar 2010. ArXiv:1002.1975v1.

[AB05] Ackermann, M.; Bernardini, E. (IceCube Collaboration): An investigation of seasonal variations in the atmospheric neutrino rate with the AMANDA-II neutrino telescope. In: *Proceedings of the 29th International Cosmic Ray Conference*. Pune, India, Aug 2005. ArXiv:astro-ph/0509330.

[Ack06] Ackermann, M.: *Searches for signals from cosmic point-like sources of high energy neutrinos in 5 years of AMANDA-II data*. Ph.D. thesis, Humboldt-Universität zu Berlin, 2006.

[AD04] Atoyan, A.; Dermer, C. D.: Neutrinos and gamma-rays of hadronic origin from AGN jets. In: *New Astron. Rev.*, volume 48:pp. 381–386, April 2004. ArXiv:astro-ph/0402646v1.

[Aha00] Aharonian, F.: TeV gamma rays from BL Lac objects due to synchrotron radiation of extremely high energy protons. In: *New Astron.*, volume 5:pp. 377–395, Nov 2000. ArXiv:astro-ph/0003159.

[AM09] Anchordoqui, L. A.; Montaruli, T.: In search of extraterrestrial high energy neutrinos. In: *Annu. Rev. Nucl. Part. Sci.*, volume 60, Nov 2009. ArXiv:0912.1035v1.

[AMH02] Alvarez-Muñiz, J.; Halzen, F.: Possible High-energy neutrinos from the cosmic accelerator RXJ1713.7-3946. In: *Astrophys. J.*, volume 576:pp. L33–L36, 2002. ArXiv:astro-ph/0205408v3.

[B+87] Bionta, R. M.; et al. (IMB Collaboration): Observation of a Neutrino Burst in Coincidence with Supernova 1987A in the Large Magellanic Cloud. In: *Phys. Rev. Lett.*, volume 58:pp. 1494–1496, Apr 1987.

[B+97] Belolaptikov, I.; et al. (Baikal Collaboration): The Baikal underwater neutrino telescope: Design, performance, and first results. In: *Astropart. Phys.*, volume 7:pp. 263–282, Aug 1997.

[B+03] Beacom, J. F.; et al.: Measuring Flavor Ratios of High-Energy Astrophysical Neutrinos. In: *Phys. Rev. D*, volume 68:p. 093005, Nov 2003. ArXiv:hep-ph/0307025v3.

[B+07] Blaufuss, E.; et al. (IceCube Collaboration): 2007 Online Filter, Jul 2007. Internal site, URL `http://wiki.icecube.wisc.edu/index.php/2007_Online_Filter`.

[B+08] Braun, J.; et al.: Methods for point source analysis in high energy neutrino telescopes. In: *Astropart. Phys.*, volume 29:pp. 299–305, May 2008. ArXiv:0801.1604.

[B+09a] Baker, M.; et al. (IceCube Collaboration): IceCube Time-Dependent Point Source Analysis Using Multiwavelength Information. In: *Proceedings of the 31st International Cosmic Ray Conference*. Lodz, Poland, Jul 2009.

[B+09b] Boersma, D.; et al. (IceCube Collaboration): Documentation for the double-muon project, 2009. Internal code repository, URL `http://code.icecube.wisc.edu/svn/projects/double-muon/releases/V01-04-01/resources/docs/index.dox`.

[B+10a] Baker, M.; et al. (IceCube Collaboration): IC-40 Time Dependent Analysis/Untriggered, 2010. Internal site, URL `http://wiki.icecube.wisc.edu/index.php/IC-40_Time_Dependent_Analysis/Untriggered`.

[B+10b] Braun, J.; et al.: Time-Dependent Point Source Search Methods in High Energy Neutrino Astronomy. In: *Astropart. Phys.*, 2010. ArXiv:0912.1572.

[BA08a] Bazo-Alba, J. L. (IceCube Collaboration): Search for neutrino point sources with IceCube 22-strings. In: *Proceedings of the Neutrino Oscillation Workshop*, volume 188. Conca Specchiulla, Otranto, Italy, Sep 2008. ArXiv:0811.4110v1.

[BA+08b] Bazo-Alba, J. L.; et al. (IceCube Collaboration): Request for a Level2 Online Muon Filter, 2008. Internal document, URL `https://docushare.icecube.wisc.edu/dsweb/Get/Document-45309/`.

[BA+09] Bazo-Alba, J. L.; et al. (IceCube Collaboration): Search for neutrino flares from point sources with IceCube. In: *Proceedings of the 31st International Cosmic Ray Conference*. Lodz, Poland, Jul 2009. ArXiv:0908.4209.

[Ber06] Berezinsky, V.: On transiton from galactic to extragalactic cosmic rays. In: *Journal of Physics: Conference Series*, volume 47:pp. 142–153, 2006.

[BMB09] Becker, J.; Meli, A.; Biermann, P.: Neutrinos from photo-hadronic interactions in Pks2155-304. In: *Proceedings of the 31st International Cosmic Ray Conference*. Lodz, Poland, Jul 2009. ArXiv:0907.4284v1.

[BZ03] Bian, W. H.; Zhao, Y. H.: Accretion rates and accretion efficiency in AGNs. In: *Publ. Astron. Soc. Japan*, volume 55:pp. 599–603, 2003. ArXiv:astro-ph/0305095v1.

[C+03] Conrad, J.; et al.: Including systematic uncertainties in confidence interval construction for Poisson statistics. In: *Phys. Rev. D*, volume 67:p. 012002, Jan 2003. ArXiv:hep-ex/0202013v2.

[Car08] Carr, J. (ANTARES Collaboration): Data from the ANTARES Neutrino Telescope. In: *Proceedings of XIII Conference on Neutrino Physics and Astrophysics (Neutrino 2008)*, volume 136. Christchurch, New Zealand, May 2008.

[CH08] Cuoco, A.; Hannestad, S.: Ultra-high energy Neutrinos from Centaurus A and the Auger hot spot. In: *Phys. Rev. D*, volume 78:p. 023007, July 2008. ArXiv:0712.1830v2.

[Che37] Cherenkov, P. A.: Visible Radiation Produced by Electrons Moving in a Medium with Velocities Exceeding that of Light. In: *Phys. Rev.*, volume 52:pp. 378–379, Aug 1937.

[Chi07] Chirkin, D. (IceCube Collaboration): Feature Extraction of IceCube Waveforms, 2007. IceCube Internat Report.

[Chi08] Chirkin, D. (IceCube Collaboration): Neutrino search with IceCube, 2008. Internat Report: icecube/200807006.

[CO96] Carroll, B. W.; Ostlie, D. A.: *An introduction to modern astrophysics*, chapter 26, pp. 1155–1202. Addison-Wesley, 1996.

[Con02] Conrad, J.: Calculation of Confidence intervals with systematic uncertainties, 2002. POLE program, URL `http://www3.tsl.uu.se/~conrad/pole.html`.

[CR04] Chirkin, D.; Rhode, W.: Muon Monte Carlo: A high-precision tool for muon propagation through matter, 2004. ArXiv:hep-ph/0407075.

[D+09] Dumm, J.; et al. (IceCube Collaboration): All-Sky Point-Source Search with 40 Strings of IceCube. In: *Proceedings of the 31st International Cosmic Ray Conference*. Lodz, Poland, Jul 2009.

[D+10] Dumm, J.; et al. (IceCube Collaboration): IC-40 PS DOMcal SaturationThresholdBug, Apr 2010. Internal site, URL `http://wiki.icecube.wisc.edu/index.php/IC-40_PS_DOMcal_SaturationThresholdBug`.

[DA81] Dziewonski, A. M.; Anderson, D. L.: Preliminary reference Earth model. In: *Physics of The Earth and Planetary Interiors*, volume 25:pp. 297–356, Jun 1981.

[D'A95] D'Agostini, G.: A multidimensional unfolding method based on Bayes' theorem. In: *Nucl. Instrum. Meth. A*, volume 362:pp. 487–498, Aug 1995.

[Der06] Dermer, C.: Best-Bet Astrophysical Neutrino Sources. In: *Proceedings of the TeV Particle Astrophysics II Workshop*, volume 60. Madison, WI, USA, Aug 2006. ArXiv:astro-ph/0611191v1.

[F+07] Filimonov, K.; et al. (IceCube Collaboration): IceCube Monitoring Web Page, 2007. Internal site, URL `http://icecube.berkeley.edu/i3-monitoring/2007/monitor.shtml`.

[FB09] Franke, R.; Bernardini, E. (IceCube Collaboration): Neutrino triggered high-energy gamma-ray follow-up with IceCube. In: *Proceedings of the 31st International Cosmic Ray Conference*. Lodz, Poland, Jul 2009.

[FC98] Feldman, G.; Cousins, R.: Unified approach to the classical statistical analysis of small signals. In: *Phys. Rev. D*, volume 57:p. 3873?3889, April 1998. ArXiv:physics/9711021.

[Fer49] Fermi, E.: On the Origin of the Cosmic Radiation. In: *Phys. Rev.*, volume 75:pp. 1169–1174, Jan 1949.

[FNV01] Fiorentini, G.; Naumov, V. A.; Villante, F. L.: Atmospheric neutrino flux supported by recent muon experiments. In: *Phys. Lett. B*, volume 510:pp. 173–188, Jun 2001. ArXiv:hep-ph/0103322v2.

[G+98] Gandhi, R.; et al.: Neutrino Interactions at Ultrahigh Energies. In: *Phys. Rev. D*, volume 58:p. 093009, Sep 1998. ArXiv:hep-ph/9807264v1.

[G+08] Ghisellini, G.; et al.: TeV variability in blazars: how fast can it be? In: *MNRAS Letters*, volume 393:pp. L16–L20, Oct 2008. ArXiv:0810.5555v1.

[Gai07] Gaisser, T. K. (IceCube Collaboration): Performance of the IceTop Array. In: *Proceedings of the 30th International Cosmic Ray Conference*. Mérida, Yucatán, México, Jul 2007. ArXiv:0711.0353v1.

[GHS95] Gaisser, T. K.; Halzen, F.; Stanev, T. S.: Particle astrophysics with high energy neutrinos. In: *Physics Reports*, volume 258-3:pp. 173–236, Jul 1995.

[GK05] Gazizov, A.; Kowalski, M.: ANIS: High Energy Neutrino Generator for Neutrino Telescopes. In: *Comput. Phys. Commun.*, volume 172:pp. 203–213, Nov 2005. ArXiv:astro-ph/0406439v1.

[Gre66] Greisen, K.: End to the Cosmic-Ray Spectrum? In: *Phys. Rev. Lett.*, volume 16:pp. 748–750, Apr 1966.

[Gri03] Grimm, H. J.: *X-ray binaries in the Milky Way and other galaxies*. Ph.D. thesis, Ludwig-Maximilian-Universität München, 2003.

[GS06] Gaensler, B. A.; Slane, P. O.: The Evolution and Structure of Pulsar Wind Nebulae. In: *Annu. Rev. Astron. Astro.*, volume 44:pp. 17–47, Apr 2006. ArXiv:astro-ph/0601081v1.

[H+87] Hirata, K.; et al. (KAMIOKANDE-II Collaboration): Observation of a Neutrino Burst from the Supernova SN 1987a. In: *Phys. Rev. Lett.*, volume 58:pp. 1490–1493, Apr 1987.

[H+98] Heck, D.; et al.: CORSIKA: A Monte Carlo Code to Simulate Extensive Air Showers. Technical Report 6019, Forschungszentrum Karlsruhe FZKA, 1998.

[H+99] Hartman, R. C.; et al.: The Third EGRET Catalog of High-Energy Gamma-Ray Sources. In: *Astrophys. J. Suppl.*, volume 123:pp. 79–202, July 1999.

[HÖ3] Hörandel, J.: On the knee in the energy spectrum of cosmic rays. In: *Astropart. Phys.*, volume 19:pp. 193–220, May 2003. ArXiv:astro-ph/0210453v1.

[H+05] Hill, G.; et al.: Examining the balance between optimising an analysis for best limit setting and best discovery potential. In: *Proceedings of PHYSTAT05*, pp. 108–111. Oxford, UK, Sep 2005.

[HÖ6a] Hörandel, J.: Cosmic rays from the knee to the second knee: 10^{14} to 10^{18} eV. In: *International School of Cosmic Ray Astrophysics - 15th Course: "Astrophysics at Ultra-High Energies"*, pp. 63–82. Erice, Sicily, Italy, Jun 2006.

[H+06b] Hultqvist, K.; et al. (IceCube Collaboration): Simulation Documentation Wiki, Jun 2006. Internal site, URL `http://wiki.icecube.wisc.edu/index.php/Simulation_Documentation_Wiki`.

[H+07] Honda, M.; et al.: Calculation of atmospheric neutrino flux using the interaction model calibrated with atmospheric muon data. In: *Phys. Rev. D*, volume 75:p. 043006, Feb 2007. ArXiv:astro-ph/0611418.

[Har06] Hartmann, B.: *Reconstruction of Neutrino-Induced Hadronic and Electromagnetic Showers with the ANTARES Experiment*. Ph.D. thesis, Friedrich-Alexander-Universität Erlangen-Nürnberg, 2006.

[Hau04] Hauschildt, T.: *Search for Cosmic Point Sources of High Energy Neutrinos with the AMANDA-II Detector*. Ph.D. thesis, Humboldt-Universität zu Berlin, 2004.

[Hil84] Hillas, A. M.: The Origin of Ultra-High-Energy Cosmic Rays. In: *Annu. Rev. Astron. Astro.*, volume 22:pp. 425–444, Sept 1984.

[Hil01] Hill, G.: Bayesian event reconstruction and background rejection in neutrino detectors, 2001. ArXiv:astro-ph/0106081v1.

[HO08] Halzen, F.; O'Murchadha, A.: Neutrinos from Auger Sources. In: *Proceedings of the 4th International Workshop on Neutrino Oscillations in Venice*. Veince, Italy, Apr 2008. ArXiv:0802.0887.

[I+07] Ishihara, A.; et al. (IceCube Collaboration): Neutrino Generator, Mar 2007. Internal site, URL `http://wiki.icecube.wisc.edu/index.php/Neutrino_Generator`.

[JR05] Japaridze, G.; Ribordy, M.: Realistic arrival time distribution from an isotropic light source, 2005. ArXiv:astro-ph/0506136v1.

[K+09] Kappes, A.; et al. (IceCube Collaboration): Systematic Errors, Jan 2009. Internal site, URL `http://www.icecube.wisc.edu/~kappes/icecube_restricted/GRB080319B/systematicerrors.html`.

[Kar07] Karle, A. (IceCube Collaboration): IceCube - construction status and performance results of the 22 string detector. In: *Proceedings of the 30th International Cosmic Ray Conference*. Mérida, Yucatán, México, Jul 2007. ArXiv:0711.0353v1.

[Kar08] Karle, A. (IceCube Collaboration): IceCube: Construction Status and First Results. In: *Proceedings of the 3rd International Workshop on the Acoustic and Radio EeV Neutrino detection Activities (ARENA)*, volume 604 1-2S. Roma, Italy, Jun 2008. ArXiv:0812.3981.

[Kir99] Kirk, J. T. O.: Multiple scattering of a photon flux: Implications for the integral average cosine of the underwater light yield. In: *Applied Optics*, volume 38:pp. 3134–3140, May 1999.

[KM3] KM3NeT Consortium: KM3NeT Conceptual Design Report. Deep-Sea Research Infrastructure, URL `http://www.km3net.org/CDR/CDR-KM3NeT.pdf`.

[L+00] Lai, H.; et al.: Global QCD analysis of parton structure of the nucleon: CTEQ-5 parton distributions. In: *Eur. Phys. Journal C*, volume 12:pp. 375–392, Feb 2000. ArXiv:hep-ph/9903282.

[L+07] Lundberg, J.; et al.: Light tracking through ice and water – Scattering and absorption in heterogeneous media with Photonics. In: *Nucl. Instrum. Meth. A*, volume 581:pp. 619–631, Nov 2007. ArXiv:astro-ph/0702108.

[L+09] Lauer, R.; et al. (IceCube Collaboration): UHE Point Source Search Systematics, Sep 2009. Internal site, URL `http://wiki.icecube.wisc.edu/index.php/UHE_Point_Source_Search_Systematics`.

[Lau10] Lauer, R.: *Extending the search for cosmic point sources of neutrinos with IceCube beyond PeV energies and above the horizon*. Ph.D. thesis, Humboldt-Universität zu Berlin, 2010.

[LM00] Learned, J. G.; Mannheim, K.: High-Energy Neutrino Astrophysics. In: *Annu. Rev. Nucl. Part. Sci.*, volume 50:pp. 679–749, Dec 2000.

[LS91] Lipari, P.; Stanev, T.: Propagation of multi-TEV muons. In: *Phys. Rev. D*, volume 44:p. 3543, Dec 1991.

[LW01] Levinson, A.; Waxman, E.: Probing Microquasars with TeV Neutrinos. In: *Phys. Rev. Lett.*, volume 87:p. 171101, Oct 2001. ArXiv:hep-ph/0106102v2.

[M+08] Montaruli, T.; et al. (IceCube Collaboration): Candidate Sources for IC22 analysis, May 2008. Internal site, URL `http://wiki.icecube.wisc.edu/index.php/IC22_Point-Source_List_Page`.

[M+09a] Meagher, K.; et al. (IceCube Collaboration): Burst Selection, 2009. Internal site, URL `http://umdgrb.umd.edu/~kjmeagher/IC40_GRB_Analysis/BurstSelection/index.html`.

[M+09b] Middell, E.; et al. (IceCube Collaboration): Improved Reconstruction of Cascade-like Events in IceCube. In: *Proceedings of the 31st International Cosmic Ray Conference*. Łódź, Poland, Jul 2009.

[Mal10] Malkus, E. (IceCube Collaboration): IceCube Array 2010, 2010. Internal Docushare, URL `https://docushare.icecube.wisc.edu/dsweb/View/Collection-8787/`.

[Mig06] Migneco, E. (NEMO Collaboration): Status of the NEMO Project. In: *Proceedings of the III International Workshop on: Neutrino Oscillations in Venice*. Venice, Italy, Feb 2006.

[MS81] Moore, R. L.; Stockman, H. S.: The class of highly polarized quasars - Observations and description. In: *Astrophys. J.*, volume 243:pp. 60–75, Jan 1981.

[MS03] Montaruli, T.; Sokalski, T.: Influence of neutrino interaction and muon propagation media on neutrino-induced muon rates in deep underwater detectors, 2003. Internal Docushare, URL `https://docushare.icecube.wisc.edu/dsweb//Get/Document-48841/Montaruli_and_Sokalski_Media_Study.pdf`.

[N+03] Nolan, P. L.; et al.: Variability of EGRET Gamma-Ray Sources. In: *Astrophys. J.*, volume 597:p. 615?627, Nov 2003. ArXiv:astro-ph/0307188v1.

[N+07] Nandikotkur, G.; et al.: Does the Blazar Gamma-Ray Spectrum Harden with Increasing Flux? Analysis of 9 Years of EGRET Data. In: *ApJ*, volume 657:p. 706, March 2007. ArXiv:0704.0939v1.

[Neu03] Neunhöffer, T.: *Die Entwicklung eines neuen Verfahrens zur Suche nach kosmischen Neutrino-Punktquellen mit dem AMANDA-Neutrinoteleskop*. Ph.D. thesis, Johannes Gutenberg Universität Mainz, 2003.

[Neu06] Neunhöffer, T.: Estimating the Angular Resolution of Tracks in Neutrino Telescopes Based on a Likelihood Analysis. In: *Astropart. Phys.*, volume 25:pp. 220–225, Apr 2006. ArXiv:astro-ph/0403367.

[Ney37] Neyman, J.: Outline of a Theory of Statistical Estimation Based on the Classical Theory of Probability. In: *Philosophical Transactions of the Royal Society of London. Series A*, volume 236:pp. 333–380, Aug 1937.

[P+02] Pumplin, J.; et al.: New Generation of Parton Distributions with Uncertainties from Global QCD Analysis. In: *JHEP*, volume 07:p. 012, Aug 2002. ArXiv:hep-ph/0201195v3.

[P+09] Paneque, D.; et al. (Fermi Collaboration): FERMI view of the TeV blazar Markarian 421. In: *Proceedings of the 31st International Cosmic Ray Conference*. Lodz, Poland, Jul 2009.

[Pan96] Pandel, D.: *Bestimmung von Wasser- und Detektorparametern und Rekonstruktion von Myonen bis 100 TeV mit dem Baikal-Neutrinoteleskop NT-72*. Master's thesis, Humboldt-Universität zu Berlin, 1996.

[RA08] Rieger, F. M.; Aharonian, F.: Particle acceleration close to the supermassive black hole horizon: the case of M87. In: *Int. J. Mod. Phys. D*, volume 17:pp. 1569–1575, Sep 2008. ArXiv:0805.4075v1.

[RBRD07] Rieger, F. M.; Bosch-Ramon, V.; Duffy, P.: Photohadronic neutrinos from transients in astrophysical sources. In: *Astrophys. Space Sci.*, volume 309:pp. 119–125, Jun 2007. ArXiv:astro-ph/0610141v1.

[Rei60] Reines, F.: Neutrino interactions. In: *Annu. Rev. Nucl. Sci.*, volume 10:pp. 1–26, 1960.

[Res06] Resvanis, L. K. (NESTOR Collaboration): Recent results from NESTOR. In: *Proceedings of the III International Workshop on: Neutrino Oscillations in Venice*. Venice, Italy, Feb 2006.

[Rob92] Roberts, A.: The birth of high-energy neutrino astronomy: A personal history of the DUMAND project. In: *Rev. Mod. Phys.*, volume 64:pp. 259–312, Jan 1992.

[Roo03] Roodman, A.: Blind Analysis in Particle Physics. Technical Report SLAC-PUB-10281, SLAC California, PHYSTAT2003, 2003.

[Rot09] Roth, A. P.: *A search for muon neutrinos from Gamma-Ray Bursts with the IceCube 22-string detector*. Ph.D. thesis, University of Maryland, 2009.

[S+98] Stokstad, R. G.; et al.: RAP - A method for absolute time-calibration of a large array based on a Digital Optical Module System. In: *LBNL-43200*, Oct 1998.

[S+07] Satalecka, K.; et al. (IceCube Collaboration): Cluster Search for neutrino flares from pre-defined directions. In: *Proceedings of the 30th International Cosmic Ray Conference*, pp. 115–118. Mérida, Yucatán, México, Jul 2007. ArXiv:0711.0353v1.

[Sch08] Schulz, O. (IceCube Collaboration): The IceCube DeepCore. In: *High Energy Gamma-Ray Astronomy: Proceedings of the 4th International Meeting on High Energy Gamma-Ray Astronomy*, volume 1085. Heidelberg, Germany, Jul 2008.

[Seo09] Seo, S. H. (IceCube Collaboration): Selection of High Energy Tau Neutrinos in IceCube. In: *Proceedings of the 31st International Cosmic Ray Conference*. Łódź, Poland, Jul 2009.

[SS96] Stecker, F. W.; Salamon, M. H.: High Energy Neutrinos from Quasars. In: *Space Sci. Rev.*, volume 75:pp. 341–355, Jan 1996. ArXiv:astro-ph/9501064v1.

[T+09] Tilav, S.; et al. (IceCube Collaboration): Atmospheric Variations as observed by IceCube. In: *Proceedings of the 31st International Cosmic Ray Conference*. Lodz, Poland, Jul 2009. ArXiv:1001.0776v2.

[U+97] Ulrich, M. H.; et al.: Variability of Active Galactic Nuclei. In: *Annu. Rev. Astron. Astro.*, volume 35:pp. 445–502, Sept 1997.

[UP95] Urry, C. M.; Padovani, P.: Unified Schemes for Radio-Loud Active Galactic Nuclei. In: *Publ. Astron. Soc. Pac.*, volume 107:pp. 803–845, Sep 1995. ArXiv:astro-ph/9506063v2.

[vE+07] van Eijndhoven, N.; et al.: Implementation of a Gauss convoluted Pandel PDF for track reconstruction in Neutrino Telescopes. In: *Astropart. Phys.*, volume 28:pp. 456–462, Dec 2007. ArXiv:0704.1706v2.

[W+07] Woschnagg, K.; et al. (IceCube Collaboration): New ice model, May 2007. Internal site, URL `http://wiki.icecube.wisc.edu/index.php/New_ice_model`.

[WB01] Waxman, E.; Bahcall, J.: High energy astrophysical neutrinos: The upper bound is robust. In: *Phys. Rev. D*, volume 64:p. 023002, Jun 2001. ArXiv:hep-ph/9902383v2.

[Wie09] Wiebusch, C. (IceCube Collaboration): Physics Capabilities of the IceCube DeepCore Detector. In: *Proceedings of the 31st International Cosmic Ray Conference*. Łódź, Poland, Jul 2009. ArXiv:0907.2263.

[Wis08] Wischnewski, R. (Baikal Collaboration): The BAIKAL neutrino experiment - physics results and perspectives. In: *Proceedings of the Very Large Volume Neutrino Telescope Workshop (VLVNT08)*, volume 604 1-2S. Toulon, France, April 2008. ArXiv:0811.1109.

[Z+03] Zhang, B.; et al.: High-energy neutrinos from magnetars. In: *Astrophys. J.*, volume 595:pp. 346–351, Sep 2003. ArXiv:astro-ph/0210382v2.

[ZC07] Zornoza, J.; Chirkin, D. (IceCube Collaboration): Muon energy reconstruction and atmospheric neutrino spectrum unfolding with the IceCube detector. In: *Proceedings of the 30th International Cosmic Ray Conference*. Mérida, Yucatán, México, Jul 2007. ArXiv:0711.0353v1.

List of Figures

2.1. Cosmic-ray spectrum and power law spectral index as a function of energy. 4

3.1. Feynman diagram of charged current neutrino-nucleon interaction. . . . 15
3.2. Cross sections for ν-N and $\bar{\nu}$-N interactions. 16

4.1. Side 3D view of the complete ICECUBE Observatory 20
4.2. Top view of the complete ICECUBE Observatory 21
4.3. Diagram of the energy range of ICECUBE Observatory's sub-detectors . 21
4.4. Top view of the ICECUBE detector at intermediate deployment steps. . . 23
4.5. Schematics of a Digital Optical Module 26
4.6. Depth dependence of the effective absorption and scattering in ice . . . 27

6.1. Number of events per bin in IC22. 42
6.2. Binned Sensitivity and discovery potential for IC22 43
6.3. Azimuth and zenith distribution of data normalized for each zenith band. 45
6.4. Energy background pdf from data as a function of zenith angle. 45
6.5. Energy signal pdf as a function of energy and spectral index. 47
6.6. Energy signal pdf for different zenith bands. 48
6.7. Uptime corrected rates and fits for IC22 and IC40. 51
6.8. Pdfs of the test statistics for bkgd and bkgd+signal simulations in IC40. . 53
6.9. Detection Probabilities for 40 selected sources distributed in declination 55
6.10. Poisson average events for a 5σ discovery for different flare durations . 56
6.11. IC22 sensitivity and discovery potential for two time-integrated methods 57
6.12. IC40 discovery potential for time-variable binned and unbinned methods 57
6.13. Trial factor according to the p-value for the list of 28 source in IC22. . . . 61
6.14. Distributions of the excess parameter 61

7.1. Rates as a function of time for IC22 and IC40. 65
7.2. Background rejection power for different cut parameters in IC22. 71
7.3. Surviving events after increasing cuts in IC22 72
7.4. Cuts values as a function of declination 73
7.5. Bin radius as a function of declination 74
7.6. Zenith, azimuth and energy distributions of the IC22 sample. 76
7.7. Point Spread Function for IC22. 77
7.8. Angular resolution versus declination, azimuth, energy and COGZ for IC22. 78
7.9. IC22 final sample energy distribution of signal simulation. 79
7.10. Signal efficiency versus zenith and energy for IC22. 80
7.11. Surviving events after cuts and Data-MonteCarlo normalization in IC22 81
7.12. IC22 data and atmospheric neutrino comparison ($\theta > 90^\circ$) 82
7.13. IC22 data and atmospheric neutrino comparison ($\theta > 115^\circ$) 83

7.14. Effective area for different declination ranges for IC22. 84
7.15. Zenith, azimuth and energy distribution of the IC40 sample. 85
7.16. IC40 geometry and axes corresponding to the azimuth peaks. 85
7.17. Angular resolution versus zenith, azimuth, energy and COGZ for IC40. 87

8.1. Locations in the sky of the selected 10 sources for IC22. 93
8.2. Fermi variable sources photon flux distribution 94
8.3. Locations in the sky of the selected 40 sources for IC40. 94

9.1. Excess parameter and upper limits distribution of the 28 IC22 sources. . 98
9.2. Excess parameter for the real and randomized skymaps using IC22. . . . 100
9.3. IC22 significance and event skymap 101
9.4. P-values in the sky of the selected 10 sources for IC22. 102
9.5. Fluence upper limits of the 40 selected sources as function of declination. 104
9.6. P-values in the sky of the selected 40 sources for IC40. 104
9.7. Statistical errors from background and neutrino signal simulation. . . . 107
9.8. Distributions of reconstruction parameters after stronger cuts. 110
9.9. Data/simulation comparison of paraboloid sigma for IC40. 111
9.10. Data/simulation comparison of energy estimated for IC40. 112

A.1. Pull distribution and fit for the IC22 UHE sample. 120

List of Tables

4.1. Historical and future deployment by season of the ICECUBE Observatory 19

5.1. Passing rates for online Level2 filter in IC40 38

6.1. Rate fit parameters and errors for IC22 and IC40 50

7.1. Good runs, periods and uptime fraction for IC22 and IC40. 64

8.1. Time-integrated candidate source list for IC22. 90
8.2. IC22 pre-defined variable astrophysical source candidates. 95

9.1. Time-integrated search results for the IC22 candidate source list 99
9.2. Time dependent search results for IC22. 103
9.3. Time dependent search results for IC40. 105
9.4. Systematic errors from parameter reconstruction bias 111
9.5. Statistical and Systematic errors summary for all analyses. 113

B.1. Physics filters cuts for the 2007/08 season. 121
B.2. Final cuts for the IC22 Northern sky binned sample. 122
B.3. Physics filters cuts for the 2008/09 season. 123

Abbreviations

Abbreviation	Explanation
AGN	Active Galactic Nuclei
AHA	Additionally Heterogeneous Absorption
ANIS	All Neutrino Interaction Simulation
ANTARES	Astronomy with a Neutrino Telescope and Abyss environmental RESearch
AMANDA	Antarctic Muon and Neutrino Detector Array
AURA	Askaryan Under-ice Radio Array
ATWD	Analog Transient Waveform Digitizer
CC	Charged Current
CMB	Cosmic Microwave Background
COG	Center Of Gravity
CORSIKA	COsmic Ray SImulations for KAscade
DAQ	Data Acquisition
dof	degrees of freedom
DOM	Digital Optical Module
DUMAND	Deep Underwater Muon And Neutrino Detector
EGRET	Energetic Gamma Ray Experiment Telescope
EHE	Extremely High Energy
fADC	fast Analog to Digital Converter
FC	Feldman & Cousins
FE	Feature Extractor
FPGA	Field-Programmable Gate Array
FSRQ	Flat-Spectrum Radio Quasar
GCD	Geometry Calibration Detector status
GLAST	Gamma-ray Large Area Space Telescope
HBL	High-frequency peaked Blazars
HESS	High Energy Stereoscopic System
HLC	Hard Local Coincidence
HMXB	High-Mass X-ray Binary
HPQ	Highly Polarized Quasar
HV	High Voltage
IACT	Imaging Atmospheric Cherenkov Telescopes
IC22	IceCube 22-string configuration
IC40	IceCube 40-string configuration
KS	Kolmogorov-Smirnov
LAT	Large Area Telescope
LBL	Low-frequency peaked Blazars
LED	Light Emitting Diode
LLH	Log LikeliHood

Abbreviation	Explanation
LPQ	Low-Polarized Quasar
MC	MonteCarlo
MJD	Modified Julian Days
MMC	Muon Monte Carlo
MPE	Multiple Photo-Electron
MRF	Model Rejection Factor
MRP	Model Rejection Potential
MWL	MultiWaveLength
NC	Neutral Current
NEMO	NEutrino Mediterranean Observatory
NESTOR	Neutrino Extended Submarine Telescope with Oceanographic Research
NToO	Neutrino triggered Target of Oportunity
GPS	Global Positioning System
GRB	Gamma-Ray Burst
PDF	Probability Density Function
pe	photo-electron
PMT	PhotoMultiplier Tube
PREM	Preliminary Reference Earth Model
PSF	Point Spread Function
PWN	Pulsar Wind Nebula
QSO	Quasi-Stellar Object
RAP	Reciprocal Active Pulsing
RLG	Radio-Loud Galaxy
RQPM	Recombination Quark Parton Model
RTV	Room-Temperature Vulcanizing
SED	Spectral Energy Distribution
SMT	Simple Majority Trigger
SNO	Sudbury Neutrino Observatory
SNR	Supernova Remnant
SPE	Single Photo-Electron
SPATS	South Pole Acoustic Test Setup
SSRQ	Steep Spectrum Radio Quasars
TDRSS	Tracking and Data Relay Satellite System
TWR	Transient Waveform Recorder
UHECR	Ultra High Energy Cosmic Rays
ULEE	Ultra Low Energy Events
WIMP	Weakly Interacting Massive Particle

Acknowledgments

During these three years of PhD several people have supported and influenced this work. I would like to recognize them in the following lines.

First of all, I would like to thank my advisor Elisa for giving me the opportunity to be part of the young investigators group, guiding me in this research, introducing me to several new concepts and methods and being ready to help and give suggestions.

My thanks also go to Dr. Christian Spiering for enthusiastically leading the astroparticle group in Zeuthen creating a flexible work atmosphere and for allowing me to go to the South Pole, a once in a lifetime experience.

Thanks to all those who read, corrected and made suggestions to improve this thesis: Elisa, Christian, Gareth, RobertL, Gernot, MikeW, Tilo, RobertF, Rolf, StefanS, Pratik and Konstancja. I would also like to thank Prof. Dr. Thomas Gaisser and Prof. Dr. Hermann Kolanoski for kindly accepting being part of my thesis committee.

Many thanks to both Roberts and Pratik for useful discussions about the methods and to our colleagues from IceCube, specially to Chad, JonD and MikeB for their help on developing the unbinned method. Thanks to our programming and IceCube software experts for all the tips and tricks, from old times with Bernhard and MartinT, and now with RobertF and Fabian.

But life is not all about physics and I could not have handled all this work without many nights and weekends of fun, culture and relaxation in Berlin, a unique and wonderful city.

Thanks RobertL for inviting me to join the WG, introducing me to your friends, who are also now mine and for a smooth integration into German life. Thanks Pratik for initiating the good habit of the Dinner Club and to all of you who kept on coming. Thanks Delia for the funniest photo-shooting at the Pole. For the conversations about the world and life near the lake, in the S-Bahn and during breaks, that helped relaxing my mind, thanks not only but specially to: Sirin, MartinB, Maria, Pratik, Lotfi, Eike, Sebastian, Anna, Achim, Arne and Madalina.

Gracias a los hispanohablantes: Rosa, Elena, Manuel, Victoria y Nati que no permitieron que me olvidara de mi idioma, por todas las conversaciones relajantes. Danke auch an meine Tandempartnerinnen, Johanna, Franzi, Kathi und Jeannine mit denen ich auch Spanisch geübt habe, für alle Gespräche über alles und nichts. Thanks to Michele for the Italo-Deutsche-English conversations and Spaß outside Zeuthen, the dinners at *Il Ritrovo*, movie nights and multi-kulti Partys. I would also like to thank Juan Pablo, Matteo and Marçà who, in the time between the submission of the thesis until the defense, helped me to overcome those stressful days with joyful times.

Finalmente, pero sobre todo, gracias a mis papás, que desde la distancia, cada fin de semana, me supieron escuchar, comprender, aconsejar y enviar su cariño.

...Caminante, son tus huellas
el camino y nada más;
Caminante, no hay camino,
se hace camino al andar.
Al andar se hace el camino,
y al volver la vista atrás
se ve la senda que nunca
se ha de volver a pisar.
Caminante no hay camino
sino estelas en la mar...

Antonio Machado 1875-1939
Campos de Castilla.

Selbständigkeitserklärung

Hiermit erkläre ich, die vorliegende Arbeit selbständig und ohne fremde Hilfe verfasst zu haben und nur die angegebene Literatur und Hilfsmittel verwendet zu haben. Ich habe mich nicht anderweitig um einen Doktorgrad beworben und besitze keinen entsprechenden Doktorgrad.

Die Promotionsordnung der Mathematisch-Naturwissenschaftlichen Fakultät I der Humboldt-Universität ist mir bekannt.

Berlin, den 10.06.2010 José Luis Bazo Alba